Atomistic Simulations of Material Properties under Extreme Conditions

Thesis by

Qi An

In Partial Fulfillment of the Requirements for the

Degree of

Doctor of Philosophy

CALIFORNIA INSTITUTE OF TECHNOLOGY

Pasadena, California

2012

(Defended May 11, 2012)

ACKNOWLEDGEMENTS

It is my great pleasure to thank those who made this thesis possible. I appreciate their help and encouragement to finish this thesis.

I am heartily thankful to my advisor, Prof. William A. Goddard, whose encouragement, guidance and support from the initial to the final level enabled me to develop an understanding of the atomistic simulations. I gained a lot from his patient education and mentoring, as well as brilliant thoughts on scientific questions. His enthusiasm on scientific research and extremely hard work make him a perfect paragon for me to follow in my future career.

I would like to thank Dr. Andres Jaramillo-Botero, Dr. Sergey V. Zybin, and Dr. Julius T. Su, who are my project directors and good friends. They provided a lot of help on scientific and technical aspects of the projects. They also gave me many good suggestions on my life and career.

I also would like to thank Dr. Sheng-Nian Luo, who is a brilliant physicist working on dynamic shock waves at the Los Alamos National Lab. He provided numerous suggestions on scientific research and I had a lot of useful discussions with him on my Caltech projects.

It is my honor to have Prof. William L. Johnson, Prof. Brent Fultz, and Prof. Julia Greer both in my candidacy exam and thesis defense committees. Particularly, I owe my deepest gratitude to Prof. William L. Johnson, who guided me on the amorphous alloy projects which are also a part of my thesis.

I had a lot of fun interacting with the current and former members of MSC. I would like to thank everyone at MSC, in particular, Yao Sha, Hai Xiao, Mucheng Cheng, and Lianchi Liu.

Finally I would like to express my gratitude to my parents, my wife, and my son. I thank my parents for bringing me up, as well as providing education opportunities for me. My wife, Chenying Gu accompanies me and supplies me a great deal of support and the

encouragement to finish my Ph.D. My son, Daniel An, brings us a lot of happiness and pleasure every day.

ABSTRACT

Extreme conditions involve low or high temperatures (> 1500 K), high pressures (> 30 MPa), high strains or strain rates, high radiation fluxes (> 100 dpa), and high electromagnetic fields (> 15T). Material properties under extreme conditions can be extremely different from those under normal conditions. Understanding material properties and performance under extreme conditions, including their dynamic evolution over time, plays an essential role in improving material properties and developing novel materials with desired properties.

To understand material properties under extreme conditions, we use molecular dynamics (MD) simulations with recently developed reactive force fields (ReaxFF) and traditional embedded atom methods (EAM) potentials to examine various materials (e.g., energetic materials and binary liquids) and processes. The key results from the simulations are summarized below.

Anisotropic sensitivity of RDX crystals: Based on the compress-and-shear reactive dynamics (CS-RD) simulations of cyclotrimethylene trinitramine (RDX) crystals, we predict that for mechanical shocks between 3 and 7 GPa, RDX is the most sensitive to shocks perpendicular to the (100) and (210) planes, while it is insensitive to those perpendicular to the (120), (111), and (110) planes. The simulations demonstrate that the molecular origin of anisotropic shock sensitivity is the steric hindrance to shearing of adjacent slip planes.

Mechanisms of hotspot formation in polymer bonded explosives (PBXs): The simulations of a realistic model of PBXs reveal that hotspots may form at the nonplanar interfaces where shear relaxation leads to a dramatic temperature increase that persists long after the shock front has passed the interface. For energetic materials this temperature increase is coupled to chemical reactions that eventually lead to detonation. We show that decreasing the density of the binder eliminates the hotspots or reduces the sensitivity.

Cavitation in binary metallic liquids: We demonstrate the stochastic nature of the cavitation process in binary metallic liquids, and that classical nucleation theory can predict the cavitation rate if we incorporate the Tolman length derived from the MD simulations.

Synthesis the single metallic glass on amorphous substrate: We show that single component metallic glasses (SCMGs) can be synthesized by thermal spray coating of nanodroplets onto an amorphous substrate (ND-AS). The key requirements to form the SCMGs are the rapid cooling rates and the amorphous substrates.

Carbon and hydrogen phases under extreme conditions: we report on the use of electron force fields (eFF) in characterizing the Hugoniot relationships of carbon, which includes consecutive phase transitions also captured by experiments, as well as the Hugonoit states of hydrogen centered at various initial densities compared to experiments and the predictions of other theories.

TABLE OF CONTENTS

Chapter 1 Introduction

1.1 Extreme environments

Extreme environments exhibit extreme conditions involving low or high temperature (> 1500 K), high pressure (> 30 MPa), high strain or strain rates, high radiation fluxes (> 100 dpa) and high intensity electromagnetic fields (> 15T)[1]. The extreme environments are challenging for most life forms. Most of our universe is in extreme environments such as geographical poles, very dry deserts, volcanoes, deep ocean trenches, upper atmosphere, giant planets, and stars. Much fundamental physics/chemistry and many engineering applications also inevitably involve extreme environments. Materials under extremes are not only of interest in science, but also have a great impact on our living environments and life.

Material properties under extreme conditions can be extremely different from those under normal conditions. For example, the hydrogen might become metallic phase under very high pressure[2]. Understanding material properties and performance under extreme conditions, including their structure, morphology, and dynamic evolution over time, plays an essential role in improving material properties and developing novel materials with unique properties. For example, the use of ultra-supercritical steam may allow increasing the efficiency of today's state-of-the-art coal-fired power plants from 35% to almost 60%, but this will involve raising operating temperatures by over 40% of their current capability (from 540°C to 760°C) and more than doubling the operating pressures, from 16.5 MPa to 37.9 MPa[3].

Scientific research on extreme conditions covers a variety of interests and has a great impact on various fields. For example, the examination of the equation of states of warm dense hydrogen and helium is essential to understanding the internal structure of giant planets, to designing the deuterated capsules for inertial confinement fusion (ICF), and to the many-body interactions in theory[4].

Another example is the detonation sensitivity study on energetic materials, as well as hotspot formation mechanism in polymer-bonded explosives (PBX). Understanding the detonation sensitivity of explosives plays an important role in effective strategies for developing new energetic materials with high energy density and in their safe handling, and we have witnessed drastic improvements. The explosives are embedded in the polymer binder matrix for safety during storage and transportation. It is normally accepted that hotspot formation is the initiation of detonation in energetic materials. So understanding the hotspot formation mechanisms play an essential role in designing the next generation of explosives.

Extended solid refers to the polymorphs/phases of simple molecules that are currently formed under ultrahigh-pressure conditions, where strong intermolecular bonding and tight crystal packing can be induced, leading to dramatic changes in physical, mechanical, and functional properties. The research on extended solids provides scientific insights on bonding formation and breakage under high pressure, how atoms and molecules organize over short and long ranges, and how the kinetics and thermodynamics govern materials stability[5]. It also provides the opportunity to design novel extended solids at ambient

conditions, due to the high kinetic energy barrier of reversal in extended solids. For example, the CO_2-V polymeric phase can be stable at 0.5 GPa, although it is energetically more stable than other CO_2 solid structures over 40 GPa[5].

There are some other research areas related to extreme conditions, such as the cavity process in liquids[6], the various phase transitions of various materials under high pressures[7], material properties under hypervelocity impact[8], etc.

Overall, in extreme conditions, high temperature lowers the chemical reaction barrier for chemical bond breakage and formation, and speeds up the chemical reactions. The mechanical loading conditions change or destroy the material structure and alter the material mechanical properties. It is important to use the theoretical and experimental methods that can capture these characteristics.

1.2 Experimental study and computational modeling of extreme conditions

Great progress has been achieved in experiments and theories on extreme conditions over the last several decades. Experimentally the diamond anvil cell (DAC) high-pressure experiment can achieve over 300 GPa[9] by using diamond to compress the small (sub millimeter sized) samples. Dynamical shock experiments, which generate the high temperature and high pressure by shock-wave loading, have developed from gas-gun driven to laser driven, leading to the improvement of temperature to 10^4 K and pressure to TPa[10].

Theoretically, a variety of methods have been developed based on quantum-mechanics molecular-dynamics simulations and continuum models. For example, path-integral Monte Carlo (PIMC)[11] is a quantum Monte Carlo method in the path-integral formulation of quantum mechanics, and can be applied to calculate the internal energy or free energy under very high temperature (> 10^4 K) and pressure (> 100 GPa) accurately. The Car–Parrinello molecular dynamics (CPMD), which is a type of *ab initio* molecular dynamics, explicitly introduces the electron degree of freedom as a dynamic variable[12]. The CPMD is applicable in adiabatic conditions, so it is not suitable for the highly excited states. The recently developed electron force field (eFF)[13], which also treats the electrons explicitly, can simulate the highly excited states where Born-Oppenheimer approximation may break down over long times.

To better understand various simulation methods and the concept of multiscale simulations, we give a brief introduction of computational/simulational methods. Fig. 1.1 shows that the length and time scales of the physical processes that can be examined by various simulation methods.

(1) Quantum mechanics (QM) simulation

In QM simulation, the many-body Schrödinger equations are solved to obtain the system energy as a function of nuclei and electron positions. Hartree-Fock (HF) approximation is normally used to solve the many-body Schrödinger equation[14,15]. More accurate methods use configuration interaction or couple clusters to obtain the electron correlation energy in addition to the HF approximation[17]. These simulation methods are

ab initio methods. Another popular QM method is density functional theory (DFT)[16,17] which expresses the system energy using the function of electron densities. The physical system size and time scale that can be treated with QM calculations efficiently are limited to hundreds of atoms and picoseconds, respectively.

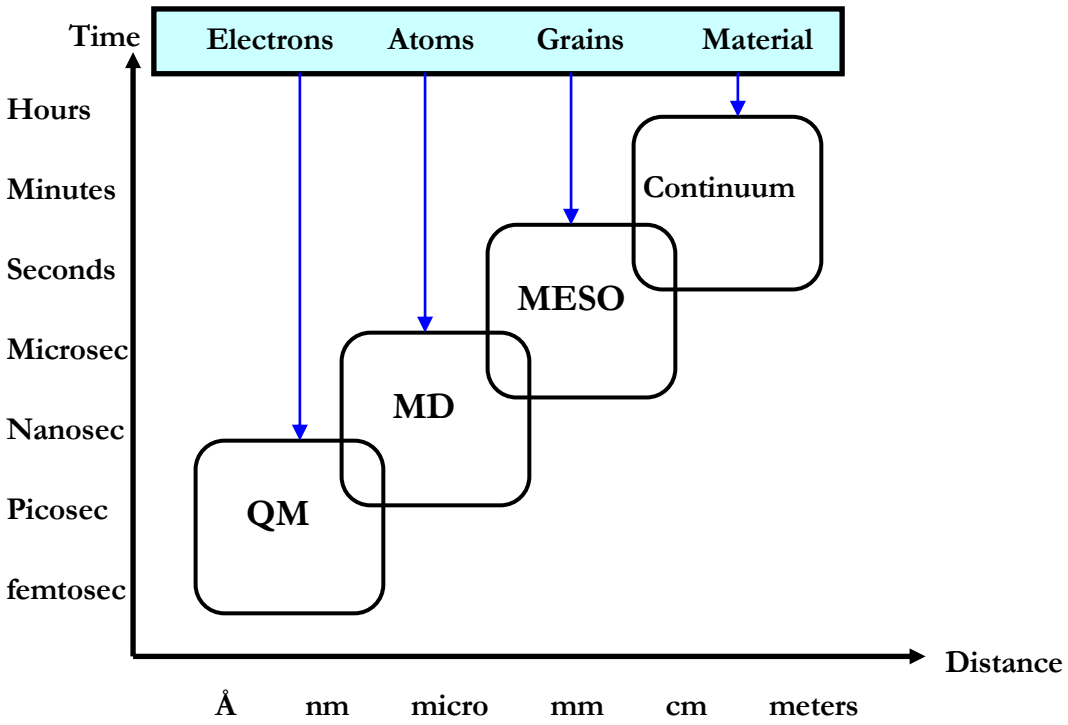

Figure 1.1 Methods for the hierarchically informed multiscale simulations

(2) Molecular dynamics (MD) simulation.

Molecular dynamics (MD) is a computer simulation of physical movements of atoms and molecules. In most situations, the trajectories of atoms and molecules are determined by the Newton's classical equation of motion. The system's physical properties can be obtained over a period when the atoms and molecules move in the phase space. The interactions of the systems are determined by the molecular mechanics force field. Chapter

2 provides detailed description on the force field. The physical system size and time scale can be treated with MD simulations and can reach millions of atoms and nanoseconds.

(3) Mesoscale simulation

The mesoscale simulation techniques ignore the atomistic details and can be applied to larger system size and longer time scale. One example is coarse-grain (CG) model[18-22]. To simulate larger system and longer time, CG models use pseudo-atoms to represent the group of atoms instead of using full atomic representations. To retain the atomic-scale characters, the interaction parameters of these pseudo-atoms are trained with the experimental data or full atomic simulations, such as solubility parameters for polymers. Another example is the kinetic Monte Carlo (KMC) method[23] which is widely used to simulate a large system over a rather long time based on the known mechanisms. Other examples include dislocation dynamics[24] which is based on the dislocation theory, and phase field models[25] for solving the interfacial problems. Dislocation dynamics could be applied to simulate plastic deformation and radiation -induced brittleness of metals. The phase-field models are widely used in solidification dynamics[26], viscous fingering[27], fracture dynamics[28], vesicle dynamics[29], etc.

(4) Continuum simulations

In continuum simulations, the systems are considered as a continuum medium. The fully developed theories, such as statistical mechanics, kinetic mechanics, and continuum mechanics are employed to explore the material properties in much larger spatial and temporal scales.

1.3 Topics of interest

The work presented here utilizes molecular dynamics simulations with recently developed novel methods (ReaxFF and eFF) and traditional methods (embedded atom method (EAM)) to examine the properties of various materials (energetic materials, binary liquids, single elements, etc.) under extreme conditions, including:

(1) Energetic materials under extreme conditions

Chapter 3 illustrates the molecular origin of anisotropic shock sensitivity. The compress-and-shear reactive dynamics (CS-RD) technique is used to study the anisotropic shock sensitivity of cyclotrimethylene trinitramine (RDX) crystal. The simulations demonstrate that the molecular origin of anisotropic shock sensitivity is the steric hindrance to shearing of adjacent slip planes.

Chapter 4 presents the initiation processes at the atomic scale, using a realistic model of PBXs as an example. It is observed that a hot spot forms at the nonplanar interface due to pronounced local shear relaxation, a mechnism of particular significance for detonation of energetic materials.

(2) Cavitation in binary metallic liquids

In Chapter 5 we simulate the cavitation process in binary metallic liquids with MD simulations and the EAM potentials, and demonstrate the stochastic nature of this phenomenon. We find that classical nucleation theory can predict the cavitation rate if we incorporate the Tolman length derived from the MD simulations.

(3) Single-component metallic glass formation via nanodroplets spraying on amorphous substrate

In Chapter 6 we show that the formation of single-component metallic glasses (SCMGs) can be achieved by thermal spray coating of nanodroplets onto an amorphous substrate (ND-AS). We demonstrate this using a molecular-dynamics simulation of nanodroplets up to 30 nm. Although the spreading of the nanodroplets during impact on a substrate leads to sufficiently rapid cooling (10^{12}–10^{13} K/sec) sustained by the large temperature gradients between the thinned nanodroplets and the bulk substrate, it is essential that the substrate be amorphous in order to ensure that the glass transition outruns crystal nucleation.

(4) Carbon and hydrogen phases under extreme conditions

In Chapter 7, we report on the use of eFF in the characterization of the Hugoniot relationship of carbon, which includes consecutive phase transitions also captured by experiments. We also report the Hugoniot states of hydrogen centered at various initial densities simulated with eFF, and compare the eFF results with experiments as well as other theories.

1.4 References

[1] A. Jaramillo-Botero, J. Su, Q. An and W. A. Goddard III, Large-scale long-term nonadiabatic electron molecular dynamics for describing material properties and phenomena in extreme environments, *J. Comp. Chem.*, 32 (3), 497−512, 2011.

[2] E. Wigner, H. B. Huntington, On the possibility of a metallic modification of hydrogen, *J. Chem. Phys.*, 3, 764−770, 1935

[3] Office of Science, U.S. Department of Energy, *Basic research needs for materials under extreme environment*s Technical Report, 2008, http://www.sc.doe.gov/bes/reports/files/MUEE_rpt.pdf.

[4] M. Ross, Linear-mixing model for shock-compressed liquid deuterium, *Phys. Rev. B*, 58(2), 669−677, 1998.

[5] A. Sengupta, M. Kim, and C. K. Yoo, Polymerization of Carbon Dioxide: A Chemistry View of Molecular-to-Nonmolecular Phase Transitions, *J. Phys. Chem. C*, 116, 2061−2067, 2012.

[6] M. S. Plesset and A. Prosperetti, Bubble Dynamics and Cavitation, *Annu. Rev. Fluid Mech.*, 9, 145–185. 1977.

[7] X. Wang, S. Scandolo, and R. Car, Carbon Phase Diagram from Ab Initio Molecular Dynamics, *Phys. Rev. Lett.*, 95, 185701, 2005.

[8] M. R. Showalter, Detection of Centimeter-Sized Meteoroid Impact Events in Saturn's F Ring, *Science*, 282, 1099−1102, 1998.

[9] R. J. Hemley and N. W. Ashcroft, The Revealing Role of Pressure in the Condensed Matter Sciences, *Physics Today*, 51 (8), 26, 1998.

[10] M. D. Knudson and M. P. Desjarlais, Shock Compression of Quartz to 1.6 TPa: Redefining a Pressure Standard, *Phys. Rev. Lett.*, 103, 225501, 2009.

[11] D. M. Ceperley, Path integrals in the theory of condensed helium, *Rev. Mod. Phys.*, 67 (2), 279–355, 1995.

[12] R. Car and M. Parrinello, Unified Approach for Molecular Dynamics and Density-Functional Theory, *Phys. Rev. Lett.*, 55, 2471−2474, 1985.

[13] J. T. Su and W. A. Goddard III, Excited electron dynamics modeling of warm dense matter, *Phys. Rev. Lett.*, 99, 185003, 2007.

[14] D. R. Hartree, The Wave Mechanics of an Atom with a Non-Coulomb Central Field. Part I. Theory and Methods, *Proc. Camb. Phil. Soc.*, 24, 89−110, 1928.

[15] F. Fock, Näherungsmethode zur Lösung des quantenmechanischen Mehrkörperproblems, *Z. Phys.*, 61, 126 (1930).

[16] A. Szabo and N. S. Ostlund, *Modern Quantum Chemistry: Introduction to Advanced Electronic Structure Theory*, McGraw-Hill Publishing Company, New York, 1989.

[17] P. Hohenberg and W. Kohn, Inhomogeneous Electron Gas, *Phys. Rev.*, 136, B 864−871, 1964.

[18] W. Kohn and L. J. Sham, Self-Consistent Equations Including Exchange and Correlation Effects, *Phys. Rev.*, 140, A1133−1138, 1965.

[19] A. Smith, C. K. Hall, Alpha-Helix Formation: Discontinuous Molecular Dynamics on an Intermediate-Resolution Protein Model, *Proteins*, 44 (3): 344–360, 2011

[20] F. Ding, J. M. Borreguero, S. V. Buldyrey, H. E. Stanley and N. V. Dokholyan, Mechanism for the alpha-helix to beta-hairpin transition, *J. Am. Chem. Soc.*, 53 (2): 220–228, 2003.

[21] E. Paci, M. Vendruscolo and M. Karplus, Validity of Go Models: Comparison with a Solvent-Shielded Empirical Energy Decomposition, *Biophys. J.*, 83 (6): 3032–3038, 2002.

[22] A. Chakrabarty and T. Cagin, Coarse grain modeling of polyimide copolymers, *Polymer*, 51, 2786–2794. 2010.

[23] V. V. Bulatov, J. F. Justo, W. Cai, S. Yip, A. S. Argon, T. Lenosky, M. de Koning, and T. D. de la Rubia, Parameter-free Modeling of Dislocation Motion: The Case of Silicon, *Philos. Mag. A*, 81 (5), 1257−1281, 2001.

[24] L. Kubin, G. Canova, M. Condat, B. Devincre, V. Pontikis, and Y. Brechet, *Solid State Phenom.*, 23/24 , 455–472, 1992.

[25] L. Q. Chen, Phase-field models for microstructure evolution, *Annual Review of Materials Research*, 32: 113−140, 2002.

[26] W. J. Boettinger et al; Phase-field simulation of solidification, *Annual Review of Materials Research*, 32, 163−194, 2002.

[27] R. Folch et al; Phase-field model for Hele-Shaw flows with arbitrary viscosity contrast. II. Numerical study, *Phys. Rev. E,* 60, 1734–1740, 1999.

[28] A. Karma et al; Phase-Field Model of Mode III: Dynamic Fracture, *Phys. Rev. Lett.*, 87, 045501, 2001.

[29] T. Biben et al; Phase-field approach to three-dimensional vesicle dynamics, Phys. Rev. E 72, 041921, 2005.

Chapter 2 Atomistic Simulation Methods

2.1 Overview

Over the past sixty years, atomistic simulations have been widely used in various research areas, such as homogeneous or heterogeneous catalysts, fuel cells, nano devices, G-protein coupled receptors, protein folding, and material properties under extreme conditions[1−6]. The most common models are quantum mechanics and molecular mechanics. These models calculate the system energy based on the arrangement of atoms and molecules. Furthermore they can determine how the energy changes as the positions of the atoms and molecules change.

These computational methods provide the tools to understand physical, chemical, and biological phenomena on the atomic scale and help to devise the new generation of materials based on these understandings. As the computational capability of modern computers grows, the atomistic simulations provide the potential to tackle a wide range of scientific issues in the future.

In this chapter we first describe the conventional force field[7] to understand the development of the force-field method. Then we focus on the methods adopted in this thesis, which include the bond-order-based reactive force field (ReaxFF)[8] and the Rossato–Guillope–Legrand (RGL) multiparticle potential for metal alloys[9]. We also discuss the recently developed *ab initio* force field method: the electron force field (eFF), which includes electrons explicitly using Pauli potential for complex electron interactions[10].

2.2 Molecular mechanics and conventional force field

Molecular mechanics is based on the classical, physical description of molecule structures. It is an empirical "ball-and-spring" model where atoms (balls) are connected by springs (bonds) that can be stretched or compressed due to intra- or intermolecular forces [7].

The potential energy of the system is calculated based on the atomic positions. The potential energy is expressed as a sum of valence or bond interactions and non-bonded interactions as shown in Eq. (2.1).

$$U = U_r + U_\theta + U_\varphi + U_\omega + U_{vdW} + U_{el} \qquad (2.1)$$

The valence interactions consist of bond stretching (U_r) and angular distortions. The angular distortion includes the bond angle bending terms (U_θ), the dihedral angle torsion terms (U_φ), and the inversion terms (U_{inv}), if needed. The non-bond interactions include the van der Waals terms (U_{vdW}), which describe the long-range attractive terms due to the London dispersion and the short-range repulsive terms due to two electron overlaps, and the electrostatic terms (U_{el}), which describe the ionic character of the system. It is also noted that some special terms should be added if hydrogen bonding is considered. The geometric representations of the valence bond interactions are shown in Fig. 2.1, and the function forms describing these interactions are discussed below.

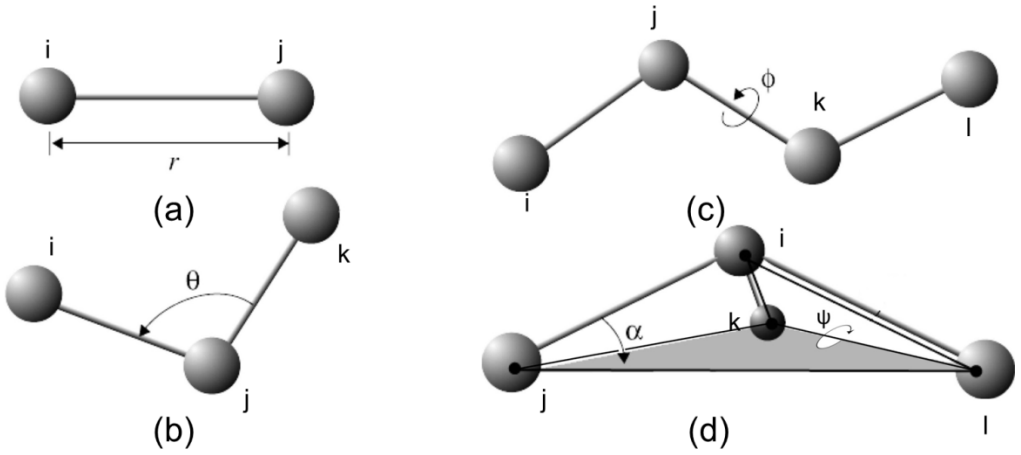

Figure 2.1 Geometric representation of valence bond interaction: (a) bond stretch, (b) angle bend, (c) torsion, (d) inversion

The bond stretching interaction of two atoms (I, J) is represented by the harmonic function shown in Eq. (2.2) where r_{IJ} is the bond distance between two atoms, and k_{IJ} is the force constant.

$$U_r = \frac{1}{2} k_{IJ}(r - r_{IJ})^2 \qquad (2.2)$$

To describe the dissociation more precisely, the Morse function is used for bond stretching rather than the harmonic function. The function form is shown in Eq (2.3), where D_{IJ} is the bond energy, r_{IJ} is the unstrained bond distance, and α is related with force constant k_{IJ} by equation $\alpha = (k_{IJ}/D_{IJ})^{1/2}$.

$$U_r = D_{IJ}(e^{-\alpha(r-r_{IJ})} - 1)^2 \qquad (2.3)$$

The angle bend interactions, as shown in Fig. 2.1b, are normally taken as harmonic function of angle θ in Eq. (2.4), where k_{IJK} is the bending force constant and θ_{IJK} is the unstrained bond angle.

$$U_\theta = \frac{1}{2} k_{IJK}(\theta - \theta_{IJK})^2 \qquad (2.4)$$

A torsion potential is the attractive or repulsive force of two bonds, or four center interactions between centers I and J and centers K and L which are connected by a common bond JK. The interaction is shown in Fig. 2.1c. The torsion potential is usually described by the cosine expansion in φ, as shown in Eq. (2.5), where φ is the torsional angle, and k_{IJKL} is the force constant. The coefficient C_n is determined by the torsional barrier U_φ, the periodicity of the potential, and the natural angle φ_{IJKL}.

$$U_\varphi = k_{IJKL} \sum_{n=0}^{m} c_n cosn\varphi \qquad (2.5)$$

In order to describe the molecular structure and vibrational frequencies, an inversion term is required in the force field (the amines and sp^2 carbon centers are shown in Fig. 2.1 d). Various ways could be used to describe the inversion interaction. For example, an MM2 inversion term[11] uses the distance R between atom I and the plane containing J, K, L, as shown in Eq. (2.6), where k_{IJKL} is the force constant.

$$U_{inv} = \frac{1}{2} k_{IJKL} R^2 \qquad (2.6)$$

The van der Waals interaction could be described by a Lennard-Jones 6-12 function or a Buckingham potential. Eq. (2.7) is for Lennard-Jones function and Eq. (2.8) is for

Buckingham potential, where ρ is the nonbonded distance, $A_{IJ,}$ A, and B are inner-wall repulsion parameters, and B_{IJ} and C_6 are the attraction parameters.

$$U_{vdw} = \frac{A_{IJ}}{\rho^{12}} - \frac{B_{IJ}}{\rho^{6}} \tag{2.7}$$

$$U_{vdw} = Ae^{-B\rho} - \frac{C_6}{\rho^{6}} \tag{2.8}$$

The electrostatic interaction can be described using either point partial charges or bond dipoles. The point charge energy is given by Eq. (2.9), where q_I and q_J are partial charges, ρ is the nonbonded distance, ε is the dielectric constant, and C is used for energy unit conversion. The bond dipole description is given by Eq. (2.10), where μ_I and μ_J are the dipoles, α_i and α_j is the angle between the dipole and the bond, and χ is the angle between two dipoles.

$$U_{el} = C\frac{q_I q_J}{\epsilon\rho} \tag{2.9}$$

$$U_{el} = C\frac{\mu_I \mu_J}{\epsilon\rho^3}\left(cos\chi - 3cos\alpha_i cos\alpha_j\right) \tag{2.10}$$

For the non-bond interactions, it is the usual convention in molecular mechanics to exclude them for the atoms that are bonded to each other (1, 2 interactions) or bonded to a common atom (1, 3 interactions).

The pre-eminent force field for organic chemistry is MM2[11], developed by Allinger and coworkers. MM2 have been developed to reproduce experimental structure, conformational energy differences, and heats of formation. The successor force field,

MM3, can also reproduce the vibration of frequencies, and for the solid state, heat of sublimation and crystal-packing geometries[12−14]. It is worth noting that the stretch-bend, stretch-torsion, bend-torsion, and bend-bend cross terms are used in MM2 and MM3 to provide a good description of small variations in structures as a function of steric interactions and intra-molecular strain.

A number of empirical potential functions have been proposed to describe biological systems. The common force fields include AMBER (assisted model building and energy refinement)[15], CHARMM (chemistry at Harvard macromolecular mechanics)[16], GROMOS (Groningen molecular simulation system)[17]. These force fields all originated as extensions to the Gelin-Karplus protein force field[18]. Other force fields include OPLS (optimized potentials for liquid simulations)[19], DREIDING[20], UFF (universal force field)[21], and Tripos[22]. OPLS is developed for liquid simulations which also include polarization effects, and UFF is developed for the whole elemental periodic table.

2.3 Reactive Force field

The conventional force fields may provide accurate predictions of geometry, conformation energy difference, and heat of formation. But they will fail when there are chemical reactions, since no bond breaking or formation is allowed. Recently developed ReaxFF[8] is a bond-order−bond-distance-dependent force field. All the valence terms (bonds, angles, and torsions) depend on bond orders which are determined uniquely from the interatomic distance. ReaxFF can describe smoothly the changes of bond connectivity

during chemical reactions and provide a useful tool to examine the process where chemical reactions play important roles.

ReaxFF has been demonstrated as capable of reproducing the potential energy surface, geometry, and barriers for chemical reactions of various materials, including hydrocarbon[8,23], nitramines[24], ceramics[25], metal[26], metal oxides[27], and energetic materials[28]. This indicates that ReaxFF can be applied to various complex environments, including extreme conditions.

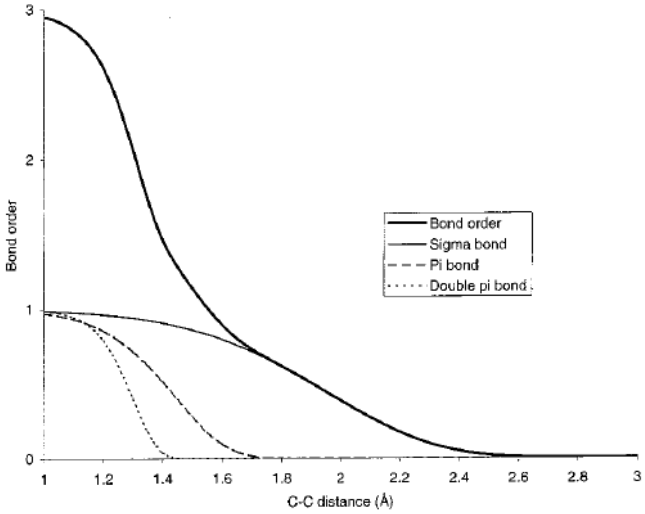

Figure 2.2 Distance dependency of carbon-carbon bond order in ReaxFF, from Ref. [8]

2.3.1 Overall system energy

Equation (2.11) describes the ReaxFF total system energy. We will describe the partial energies introduced in Eq. (2.11) in the next paragraphs.

$$E_{system} = E_{bond} + E_{lp} + E_{over} + E_{under} + E_{val} + E_{pen} + E_{coa} + E_{tors} + E_{conj} + E_{H-bond} + E_{vdWaals} + E_{Coulomb} \quad (2.11)$$

2.3.2. Bond order and bond energy

A fundamental assumption of ReaxFF is that the bond order BO'_{ij} between a pair of atoms can be obtained directly from the interatomic distance r_{ij}, as given in Eq. (2.12). In calculating the bond orders, ReaxFF distinguishes contributions from σ-bonds, π-bonds, and double- π-bonds.

$$BO_{ij}^{n} = BO_{ij}^{\sigma} + BO_{ij}^{\pi} + BO_{ij}^{\pi\pi} = \exp\left[p_{bo1} \cdot \left(\frac{r_{ij}}{r_o^{\sigma}} \right)^{p_{bo2}} \right] + \exp\left[p_{bo3} \cdot \left(\frac{r_{ij}}{r_o^{\pi}} \right)^{p_{bo4}} \right] + \exp\left[p_{bo5} \cdot \left(\frac{r_{ij}}{r_o^{\pi\pi}} \right)^{p_{bo6}} \right] \tag{2.12}$$

Based on the uncorrected bond orders BO'_{ij}, derived from Eq. (2.12), an uncorrected overcoordination Δ' can be defined for the atoms as the difference between the total bond order around the atom and the number of its bonding electrons, *Val*.

$$\Delta_i' = -Val_i + \sum_{j=1}^{neighbors(i)} BO_{ij}' \tag{2.13a}$$

$$\Delta_i'^{boc} = -Val_i^{boc} + \sum_{j=1}^{neighbors(i)} BO_{ij}' \tag{2.13b}$$

ReaxFF then uses these uncorrected overcoordination definitions to correct the bond orders BO'_{ij} using the scheme described in Eq. (2.14a−f). To soften the correction for atoms bearing lone electron pairs, a second overcoordination definition Δ'^{boc} (Eq. (2.13b)) is used in Eq. (2.14e) and (2.14f). This allows atoms like nitrogen and oxygen, which bear lone

electron pairs after filling their valence, to break up these electron pairs and involve them in bonding without obtaining a full bond-order correction.

$$
\begin{aligned}
BO_{ij}^{\sigma} &= BO_{ij}^{'\sigma} \cdot f_1(\Delta_i^{'}, \Delta_j^{'}) \cdot f_4(\Delta_i^{'}, BO_{ij}^{'}) \cdot f_5(\Delta_j^{'}, BO_{ij}^{'}) \\
BO_{ij}^{\pi} &= BO_{ij}^{'\pi} \cdot f_1(\Delta_i^{'}, \Delta_j^{'}) \cdot f_1(\Delta_i^{'}, \Delta_j^{'}) \cdot f_4(\Delta_i^{'}, BO_{ij}^{'}) \cdot f_5(\Delta_j^{'}, BO_{ij}^{'}) \\
BO_{ij}^{\pi\pi} &= BO_{ij}^{'\pi\pi} \cdot f_1(\Delta_i^{'}, \Delta_j^{'}) \cdot f_1(\Delta_i^{'}, \Delta_j^{'}) \cdot f_4(\Delta_i^{'}, BO_{ij}^{'}) \cdot f_5(\Delta_j^{'}, BO_{ij}^{'}) \\
BO_{ij} &= BO_{ij}^{\sigma} + BO_{ij}^{\pi} + BO_{ij}^{\pi\pi}
\end{aligned}
\tag{2.14a}
$$

$$
f_1(\Delta_i, \Delta_j) = \frac{1}{2} \cdot \left(\frac{Val_i + f_2(\Delta_i^{'}, \Delta_j^{'})}{Val_i + f_2(\Delta_i^{'}, \Delta_j^{'}) + f_3(\Delta_i^{'}, \Delta_j^{'})} + \frac{Val_j + f_2(\Delta_i^{'}, \Delta_j^{'})}{Val_j + f_2(\Delta_i^{'}, \Delta_j^{'}) + f_3(\Delta_i^{'}, \Delta_j^{'})} \right) \tag{2.14b}
$$

$$
f_2(\Delta_i^{'}, \Delta_j^{'}) = \exp(-p_{boc1} \cdot \Delta_i^{'}) + \exp(-p_{boc1} \cdot \Delta_j^{'}) \tag{2.14c}
$$

$$
f_3(\Delta_i, \Delta_j) = -\frac{1}{p_{boc2}} \cdot \ln\left\{ \frac{1}{2} \cdot \left[\exp\left(-p_{boc2} \cdot \Delta_i\right) + \exp\left(-p_{boc2} \cdot \Delta_j\right) \right] \right\} \tag{2.14d}
$$

$$
f_4(\Delta_i^{'}, BO_{ij}^{'}) = \frac{1}{1 + \exp(-p_{boc3} \cdot (p_{boc5} \cdot BO_{ij}^{'} \cdot BO_{ij}^{'} - \Delta_i^{'boc}) + p_{boc5})} \tag{2.14e}
$$

$$
f_5(\Delta_j^{'}, BO_{ij}^{'}) = \frac{1}{1 + \exp(-p_{boc3} \cdot (p_{boc4} \cdot BO_{ij}^{'} \cdot BO_{ij}^{'} - \Delta_j^{'boc}) + p_{boc5})} \tag{2.14f}
$$

A corrected overcoordination Δ_i can be derived from the corrected bond orders using Eq. (2.15).

$$
\Delta_i = -Val_i + \sum_{j=1}^{neighbors(i)} BO_{ij} \tag{2.15}
$$

Equation (2.16) is used to calculate the bond energies from the corrected bond orders, BO_{ij}.

$$E_{bond} = -D_e^{\sigma} \cdot BO_{ij}^{\sigma} \cdot \exp\left[p_{be1}\left(1-\left(BO_{ij}^{\sigma}\right)^{p_{be2}}\right)\right] - D_e^{\pi} \cdot BO_{ij}^{\pi} - D_e^{\pi\pi} \cdot BO_{ij}^{\pi\pi} \qquad (2.16)$$

2.3.3. Lone pair energy

Equation (2.18) is used to determine the number of lone pairs around an atom. Δ_i^e is determined in Eq. (2.17) and describes the difference between the total number of outer shell electrons (6 for oxygen, 4 for silicon, 1 for hydrogen) and the sum of bond orders around an atomic center.

$$\Delta_i^e = -Val_i^e + \sum_{j=1}^{neighbors(i)} BO_{ij} \qquad (2.17)$$

$$n_{lp,i} = \text{int}\left(\frac{\Delta_i^e}{2}\right) + \exp\left[-p_{lp1} \cdot \left(2 + \Delta_i^e - 2 \cdot \text{int}\left\{\frac{\Delta_i^e}{2}\right\}\right)^2\right] \qquad (2.18)$$

For oxygen with normal coordination (total bond order = 2, Δ_i^e = 4), Eq. (2.18) leads to 2 lone pairs. As the total bond order associated with a particular O starts to exceed 2, Eq. (2.18) causes a lone pair to gradually break up, causing a deviation Δ_i^{lp}, defined in Eq. (2.19), from the optimal number of lone pairs $n_{lp,opt}$ (e.g., 2 for oxygen, 0 for silicon and hydrogen).

$$\Delta_i^{lp} = n_{lp,opt} - n_{lp,i} \qquad (2.19)$$

This is accompanied by an energy penalty, as calculated by Eq. (2.20).

$$E_{lp} = \frac{p_{lp2} \cdot \Delta_i^{lp}}{1 + \exp\left(-75 \cdot \Delta_i^{lp}\right)} \qquad (2.20)$$

2.3.4. Overcoordination

For an overcoordinated atom ($\Delta_i > 0$), Eq. (2.21a–b) impose an energy penalty on the system. The degree of overcoordination Δ is decreased if the atom contains a broken-up lone electron pair. This is done by calculating a corrected overcoordination (Eq. (2.21b)), taking the deviation from the optimal number of lone pairs, as calculated in Eq. (2.19), into account.

$$E_{over} = \frac{\sum_{j=1}^{nbond} p_{ovun1} \cdot D_e^{\sigma} \cdot BO_{ij}}{\Delta_i^{lpcorr} + Val_i} \cdot \Delta_i^{lpcorr} \cdot \left[\frac{1}{1 + \exp\left(p_{ovun2} \cdot \Delta_i^{lpcorr} \right)} \right] \qquad (2.21a)$$

$$\Delta_i^{lpcorr} = \Delta_i - \frac{\Delta_i^{lp}}{1 + p_{ovun3} \cdot \exp\left(p_{ovun4} \cdot \left\{ \sum_{j=1}^{neighbors(i)} \left(\Delta_j - \Delta_j^{lp} \right) \cdot \left(BO_{ij}^{\pi} + BO_{ij}^{\pi\pi} \right) \right\} \right)} \qquad (2.21b)$$

2.3.5 Undercoordination

For an undercoordinated atom ($\Delta_i < 0$), we want to take into account the energy contribution to the resonance of the π-electron between the attached undercoordinated atomic centers. This is done by Eq. (2.22) where E_{under} is only important if the bonds between the undercoordinated atom *i* and its undercoordinated neighbor *j* partly have π-bond character.

$$E_{under} = -p_{ovun5} \cdot \frac{1-\exp\left(p_{ovun6} \cdot \Delta_i^{lpcor}\right)}{1+\exp(-p_{ovun2} \cdot \Delta_i^{lpcor})} \cdot \frac{1}{1+p_{ovun7} \cdot \exp\left[p_{ovun8} \cdot \left\{\sum_{j=1}^{neighbors(i)} \left(\Delta_j - \Delta_j^{lp}\right) \cdot (BO_{ij}^{\pi} + BO_{ij}^{\pi\pi})\right\}\right]} \quad (2.22)$$

2.3.6 Valence Angle Terms

2.3.6.1 Angle energy.

Just as for bond terms, it is important that the energy contribution from valence angle terms goes to zero as the bond orders in the valence angle go to zero. Equations (2.23a–g) are used to calculate the valence angle energy contribution. The equilibrium angle Θ_0 for Θ_{ijk} depends on the sum of π-bond orders (SBO) around the central atom j as described in Eq. (2.23d). Thus, the equilibrium angle changes from around 109.47° for sp^3 hybridization (π-bond = 0) to 120° for sp^2 (π-bond = 1) to 180° for sp (π-bond = 2) based on the geometry of the central atom j and its neighbors. In addition to including the effects of π-bonds on the central atom j, Eq. (2.23d) also takes into account the effects of over- and under-coordination in central atom j, as determined by Eq. (2.23e), on the equilibrium valency angle, including the influence of a lone electron pair. Val^{angle} is the valency of the atom used in the valency and torsion angle evaluation. Val^{angle} is the same as Val^{boc} used in Eq. (2.13c) for non-metals. The functional form of Eq. (2.23f) is designed to avoid singularities when SBO = 0 and SBO = 2. The angles in Eq. (2.23a)–(2.23g) are in radians.

$$E_{val} = f_7(BO_{ij}) \cdot f_7(BO_{jk}) \cdot f_8(\Delta_j) \cdot \left\{p_{val1} - p_{val1} \exp\left[-p_{val2}\left(\Theta_o(BO) - \Theta_{ijk}\right)^2\right]\right\} \quad (2.23a)$$

$$f_7(BO_{ij}) = 1 - \exp\left(-p_{val3} \cdot BO_{ij}^{p_{val4}}\right) \quad (2.23b)$$

$$f_8(\Delta_j) = p_{val5} - \left(p_{val5} - 1\right) \cdot \frac{2 + \exp\left(p_{val6} \cdot \Delta_j^{angle}\right)}{1 + \exp\left(p_{val6} \cdot \Delta_j^{angle}\right) + \exp\left(-p_{val7} \cdot \Delta_j^{angle}\right)} \quad (2.23c)$$

$$SBO = \sum_{n=1}^{neighbor(j)} \left(BO_{jn}^{\pi} + BO_{jn}^{\pi\pi}\right) + \left[1 - \prod_{n=1}^{neighbors(j)} \exp\left(-BO_{jn}^{8}\right)\right] \cdot \left(-\Delta_j^{angle} - p_{val8} \cdot n_{lp,j}\right) \quad (2.23d)$$

$$\Delta_j^{angle} = -Val_j^{angle} + \sum_{n=1}^{neighbors(j)} BO_{jn} \quad (2.23e)$$

$$\begin{aligned} &SBO2 = 0 \text{ if } SBO \le 0 \\ &SBO2 = SBO^{p_{val9}} \text{ if } 0 < SBO < 1 \\ &SBO2 = 2 - (2 - SBO)^{p_{val9}} \text{ if } 1 < SBO < 2 \\ &SBO2 = 2 \text{ if } SBO > 2 \end{aligned} \quad (2.23f)$$

$$\Theta_0\left(BO\right) = \pi - \Theta_{0,0} \cdot \left\{1 - \exp\left[-p_{val10} \cdot \left(2 - SBO2\right)\right]\right\} \quad (2.23g)$$

2.3.6.2 Penalty energy

To reproduce the stability of systems with two double bonds sharing an atom in a valency angle, like allene, an additional energy penalty, as described in Eq. (2.24a–b) is imposed for such systems. Eq. (2.19b) deals with the effects of over/undercoordination in central atom *j* on the penalty energy.

$$E_{pen} = p_{pen1} \cdot f_9(\Delta_j) \cdot \exp\left[-p_{pen2} \cdot \left(BO_{ij} - 2\right)^2\right] \cdot \exp\left[-p_{pen2} \cdot \left(BO_{jk} - 2\right)^2\right] \quad (2.24a)$$

$$f_9(\Delta_j) = \frac{2 + \exp\left(-p_{pen3} \cdot \Delta_j\right)}{1 + \exp\left(-p_{pen3} \cdot \Delta_j\right) + \exp\left(p_{pen4} \cdot \Delta_j\right)} \quad (2.24b)$$

2.3.6.3 Three-body conjugation term

The hydrocarbon ReaxFF potential contains only a four-body conjugation term, which is sufficient to describe most conjugated hydrocarbon systems. However, this term fails to

describe the stability obtained from conjugation by the –NO2-group. To describe the stability of such groups a three-body conjugation term is included (Eq. 2.25).

$$E_{coa} = p_{coa1} \cdot \frac{1}{1+\exp\left(p_{coa2} \cdot \Delta_j^{val}\right)} \cdot \exp\left[-p_{coa3} \cdot \left(-BO_{ij} + \sum_{n=1}^{neighbors(i)} BO_{in}\right)^2\right] \cdot \exp\left[-p_{coa3} \cdot \left(-BO_{jk} + \sum_{n=1}^{neighbors(i)} BO_{kn}\right)^2\right] \cdot \exp\left[-p_{coa4} \cdot \left(BO_{ij} - 1.5\right)^2\right] \cdot \exp\left[-p_{coa4} \cdot \left(BO_{jk} - 1.5\right)^2\right] \quad (2.25)$$

2.3.7. Torsion angle terms

2.3.7.1 Torsion rotation barriers

Just as with the angle terms, we need to ensure that the energy of torsion angle ω_{ijkl} accounts properly for BO close to 0 and for BO greater than 1. This is done by Eq. (2.26a–c).

$$E_{tors} = f_{10}(BO_{ij}, BO_{jk}, BO_{kl}) \cdot \sin\Theta_{ijk} \cdot \sin\Theta_{jkl} \cdot \left[\frac{1}{2}V_2 \cdot \exp\left\{p_{tor1} \cdot \left(BO_{jk}^{\pi} - 1 + f_{11}(\Delta_j, \Delta_k)\right)^2\right\} \cdot \left(1 - \cos 2\omega_{ijkl}\right) + \frac{1}{2}V_3 \cdot \left(1 + \cos 3\omega_{ijkl}\right)\right] \quad (2.26a)$$

$$f_{10}(BO_{ij}, BO_{jk}, BO_{kl}) = \left[1 - \exp\left(-p_{tor2} \cdot BO_{ij}\right)\right] \cdot \left[1 - \exp\left(-p_{tor2} \cdot BO_{jk}\right)\right] \cdot \left[1 - \exp\left(-p_{tor2} \cdot BO_{kl}\right)\right] \quad (2.26b)$$

$$f_{11}(\Delta_j, \Delta_k) = \frac{2 + \exp\left[-p_{tor3} \cdot \left(\Delta_j^{angle} + \Delta_k^{angle}\right)\right]}{1 + \exp\left[-p_{tor3} \cdot \left(\Delta_j^{angle} + \Delta_k^{angle}\right)\right] + \exp\left[p_{tor4} \cdot \left(\Delta_j^{angle} + \Delta_k^{angle}\right)\right]} \quad (2.26c)$$

2.3.7.2 Four body conjugation term.

Eq. (2.27a–b) describe the contribution of conjugation effects to the molecular energy. A maximum contribution of conjugation energy is obtained when successive bonds have bond order values of 1.5, as in benzene and other aromatics.

$$E_{conj} = f_{12}(BO_{ij}, BO_{jk}, BO_{kl}) \cdot p_{\cot 1} \cdot \left[1 + \left(\cos^2 \omega_{ijkl} - 1\right) \cdot \sin\Theta_{ijk} \cdot \sin\Theta_{jkl}\right] \quad (2.27a)$$

$$f_{12}(BO_{ij}, BO_{jk}, BO_{kl}) = \exp\left[-p_{\cot 2} \cdot \left(BO_{ij} - 1\frac{1}{2}\right)^2\right] \cdot \exp\left[-p_{\cot 2} \cdot \left(BO_{jk} - 1\frac{1}{2}\right)^2\right] \cdot \exp\left[-p_{\cot 2} \cdot \left(BO_{kl} - 1\frac{1}{2}\right)^2\right] \quad (2.27b)$$

2.3.8. Hydrogen bond interactions

Equation (2.28) describes the bond-order dependent hydrogen bond term for a X-H—Z system as incorporated in ReaxFF.

$$E_{Hbond} = p_{hb1} \cdot \left[1 - \exp\left(p_{hb2} \cdot BO_{XH}\right)\right] \cdot \exp\left[p_{hb3}\left(\frac{r_{hb}^o}{r_{HZ}} + \frac{r_{HZ}}{r_{hb}^o} - 2\right)\right] \cdot \sin^8\left(\frac{\Theta_{XHZ}}{2}\right) \quad (2.28)$$

2.3.9. Nonbond interactions

In addition to the valence interactions which depend on overlap, there are repulsive interactions at short interatomic distances due to Pauli principle orthogonalization and attraction energies at long distances due to dispersion. These interactions, comprised of van der Waals and Coulomb forces, are included for all atom pairs, thus avoiding awkward alterations in the energy description during bond dissociation.

2.3.9.1 Taper correction

To avoid energy discontinuities when charged species move in and out of the non-bonded cutoff radius, ReaxFF employs a Taper correction. Each nonbonded energy and derivative is multiplied by a Taper term, which is taken from a distance-dependent 7th-order polynomial (Eq. (2.29)).

$$Tap = Tap_7 \cdot r_{ij}^7 + Tap_6 \cdot r_{ij}^6 + Tap_5 \cdot r_{ij}^5 + Tap_4 \cdot r_{ij}^4 + Tap_3 \cdot r_{ij}^3 + Tap_2 \cdot r_{ij}^2 + Tap_1 \cdot r_{ij} + Tap_0 \quad (2.29)$$

The terms in this polynomial are chosen to ensure that all 1st, 2nd, and 3rd derivatives of the non-bonded interactions to the distance are continuous and go to zero at the cutoff boundary. To that end, the terms Tap_0 to Tap_7 in Eq. (2.29) are calculated by the scheme in Eq. (2.30), where R_{cut} is the non-bonded cutoff radius.

$$\begin{aligned} Tap_7 &= 20 / R_{cut}^7 \\ Tap_6 &= -70 / R_{cut}^6 \\ Tap_5 &= 84 / R_{cut}^5 \\ Tap_4 &= -35 / R_{cut}^4 \\ Tap_3 &= 0 \\ Tap_2 &= 0 \\ Tap_1 &= 0 \\ Tap_0 &= 1 \end{aligned} \quad (2.30)$$

2.3.9.2 Van der Waals interactions

To account for the van der Waals interactions we use a distance-corrected Morse-potential (Eq. 2.31a–b). By including a shielded interaction (Eq. 2.31b) excessively high repulsions between bonded atoms (1–2 interactions) and atoms sharing a valence angle (1–3 interactions) are avoided.

$$E_{vdWaals} = Tap \cdot D_{ij} \cdot \left\{ \exp\left[\alpha_{ij} \cdot \left(1 - \frac{f_{13}(r_{ij})}{r_{vdW}} \right) \right] - 2 \cdot \exp\left[\frac{1}{2} \cdot \alpha_{ij} \cdot \left(1 - \frac{f_{13}(r_{ij})}{r_{vdW}} \right) \right] \right\} \quad (2.31a)$$

$$f_{13}(r_{ij}) = \left[r_{ij}^{p_{vdW1}} + \left(\frac{1}{\gamma_w} \right)^{p_{vdW1}} \right]^{\frac{1}{p_{vdW1}}} \quad (2.31b)$$

2.3.9.3 Coulomb Interactions

As with the van der Waals-interactions, Coulomb interactions are taken into account between all atom pairs. To adjust for orbital overlap between atoms at close distances, a shielded Coulomb-potential is used.

$$E_{coulomb} = Tap \cdot C \cdot \frac{q_i \cdot q_j}{\left[r_{ij}^3 + \left(1/\gamma_{ij} \right)^3 \right]^{1/3}} \quad (2.32)$$

Atomic charges are calculated using the electronegativity equalization method (EEM) approach[29]. The EEM charge-derivation method is similar to the QEq scheme[30]; the only differences, apart from parameter definitions, are that EEM does not use an iterative scheme for hydrogen charges (as in QEq) and that QEq uses a more rigorous Slater orbital approach to account for charge overlap.

2.4 Rossato–Guillope–Legrand multiparticle potential

To examine the material properties of metallic alloys, we need to find a force field for metallic systems. From many previous studies of metal alloys, it is clear that simple two-body pair potentials are inadequate to describe metal systems[31]. For example, pair potentials always lead to elastic constants C_{12}=C_{44} (Cauchy relation) in cubic solids and the

ratio of the vacancy formation energy to cohesive energy as unity, both of which strongly deviate from the fundamental properties of metallic solids.

To describe the cohesive forces in normal metals requires a many-body description. Several such force fields have been used successfully, including the embedded atom model (EAM), ReaxFF, Sutton-Chen, and RGL forms.

In the multi particle potentials, the cohesive energy can be written in the form [32,33]

$$E_{coh} = E_{rep} + E_{bond} , \qquad (2.33)$$

where E_{rep} is the repulsive energy which can be represented as a sum of pair-repulsive energy, and E_{bond} is the binding energy which is expressed in terms of the total density of states D(E).

In the tight-binding model the contribution of a pair of atoms to the binding energy depends on the distance between the atoms and the character of the neighbors. For this reason, in RGL potential the binding energy is of a multi particle character and can be represented as

$$E_{bond} = -\{\sum_{j\neq i} \xi_{\alpha\beta}^2 \, e^{-2q_{\alpha\beta}(\frac{r_{ij}}{r_0^{\alpha\beta}}-1)}\}^{1/2} , \qquad (2.34)$$

where r_{ij} is the distance between the atoms i and j, $r_0^{\alpha\beta}$ is the distance between the nearest neighbors in the αβ lattice, ξ is the effective exchange overlap integral, and q determines the dependence of the latter on distance. To ensure stability of the system, a Born-Mayer pair repulsion is added to the binding energy.

$$E_{rep}^{i} = \sum_j A_{\alpha\beta} e^{-p_{\alpha\beta}(r_{ij}-1)} . \quad (2.35)$$

The total cohesive energy is

$$E_{coh} = \sum_i (E_{rep}^{i} + E_{bond}^{i}) \quad (2.36)$$

The force-field parameters are optimized to reproduce QM-calculated or experimental properties, including the equilibrium lattice constants, cohesive energies, bulk modulus, and equation of states.

2.5 Electron force field

In the classical force field discussed above, a single potential energy surface is represented in the force field which is the consequence of Born-Oppenheim approximation, while in the extreme conditions where the electronic excited states play important roles, the Born-Oppenheim approximation breaks down. One way to incorporate these non-adiabatic effects is to use *ab initio* molecular dynamics, such as time-dependent density functional theory (TDDFT)[34]. But the TDDFT method is a very expensive approach and can only be applied to very small system (limit ~ 100 atoms). Recently developed eFF[6,10] is another non-adiabatic wave function MD approach that overcomes the heavy computational cost by using approximation in the electronic structure calculation with near- first-principles accuracy.

In eFF, the nucleus is represented by point charge and the electron is represented by single Gaussian wave package ($\varphi = \exp[(\boldsymbol{r} - \boldsymbol{x_i})^2/s_i^2]$), where **r** is the nucleus position,

$\mathbf{x_i}$ is the electron position and $\mathbf{s_i}$ is the electron size. The electron size is a dynamical variable. The N-electron wave function is described as the Hartree product of the single Gaussian waves. Eq. (2.37) shows the energy expression of eFF, which includes the electron kinetic energy (E_{KE}), the electrostatic potential energy (nucleus-nucleus E_{NN}, nucleus-electron E_{Ne}, electron-electron E_{ee}), and the spin-dependent Pauli exclusion interaction (E_{pauli}), which accounts for the anti-symmetry property of electrons.

$$E(R,r,s) = E_{NN}(R) + E_{Ne}(R,r,s) + E_{ee}(r,s) + E_{KE}(r,s) + E_{pauli}(\uparrow\downarrow,S) \quad (2.37)$$

The energy expressions for the terms in Eq. (2.37) are shown below:

$$E_{KE} = \sum_i \frac{3}{2s_i^2}$$

$$E_{NN} = \sum_{i<j} \frac{Z_i Z_j}{R_{ij}}$$

$$E_{Ne} = -\sum_{ij} \frac{Z_i}{R_{ij}} Erf\left(\frac{\sqrt{2}R_{ij}}{s_j}\right)$$

$$E_{ee} = \sum_{i<j} \frac{1}{r_{ij}} Erf\left(\frac{\sqrt{2}r_{ij}}{\sqrt{s_i^2+s_j^2}}\right) \quad (2.38)$$

$$E_{pauli} = \sum_{\sigma_i=\sigma_j} E(\uparrow\uparrow)_{ij} + \sum_{\sigma_i\neq\sigma_j} E(\uparrow\downarrow)_{ij}$$

$$E(\uparrow\uparrow)_{ij} = \left(\frac{S_{ij}^2}{1-S_{ij}^2} + (1-\rho)\frac{S_{ij}^2}{1+S_{ij}^2}\right)\Delta T_{ij}$$

$$E(\uparrow\downarrow)_{ij} = \left(\rho\frac{S_{ij}^2}{1+S_{ij}^2}\right)\Delta T_{ij},$$

where ΔT_{ij} is a measure of the change in the kinetic energy of the electrons upon antisymmetrization, and S_{ij} is the overlap between the two wave packets, which are both dependent on the scaled sizes, s_i' and s_j', of the electrons and the scaled distance separating them, r_{ij}'. The ρ, size-scaling parameter, and distance-scaling parameters are the three universal fitting parameters used to reproduce small-molecule geometries such as CH_4, C_2H_6, LiH, and B_2H_6.

The Pauli principle for fermions requires that the antisymmetric wave function is a Slater determinant which contains *N!* product terms. But evaluating the energy of such wave function requires N^4 operations, mostly for the four-center electron-electron repulsive integrals. To avoid this, eFF electrons are independent Gaussian wave packets. The Pauli potential is proposed for the difference in energy between Slater determinant and the Hartree products of the orbitals. It is derived by considering the difference between the antisymmetric and symmetric combinations of valence bond states, and assuming that kinetic energy differences predominate. Fig. 2.3 shows the Pauli potential and electrostatic energy of two electrons.

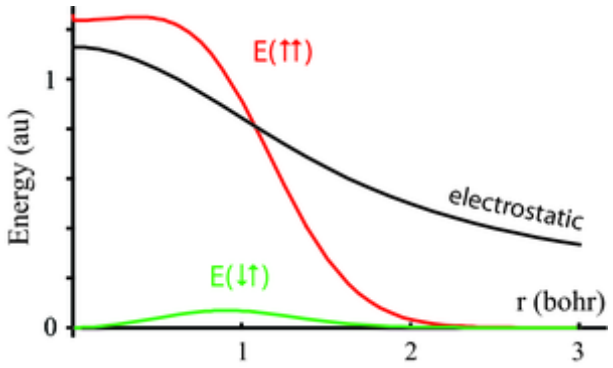

Figure 2.3 The general functional form of E_{pauli}, and the particular Pauli repulsion between two electrons with size s = 1 Bohr, as a function of their separation, r, and spin (↑ and ↓). The Pauli repulsion between two same-spin electrons increases more steeply at short distances than the electrostatic repulsion.

2.6 **References**

[1] W. A. Goddard III, J. E. Mueller, K. Chenoweth, and A. Van Duin, ReaxFF Monte Carlo reactive dynamics: Application to resolving the partial occupations of the M1 phase of the MoVNbTeO catalyst, *Catalysis Today*, 157 (1−4): 71−76, 2010.

[2] W. A. Goddard III, B. Merinov, A. Van Duin, T. Jacob, M. Blanco, V. Molinero, S. S. Jang, and Y. H. Jang, Multi-paradigm multi-scale simulations for fuel cell catalysts and membranes, *Molecular Simulations*, 32, 251−268, 2006.

[3] R. J. Trabanino, S. E. Hall, N. Vaidehi, W. B. Floriano, V. W. T. Kam, and W. A. Goddard III, First principles predictions of the structure and function of G-protein-coupled receptors: Validation for bovine rhodopsin, *Biophysical Journal*, 86 (4): 1904−1921, 2004.

[4] H. B. Su, R. J. Nielsen, A. Van Duin, and W. A. Goddard III, Simulations on the effects of confinement and Ni-catalysis on the formation of tubular fullerene structures from peapod precursors, *Physical Review B*, 75 (13): 134107, 2007.

[5] Y. Duan and P. A. Kollman, Pathways to a Protein Folding Intermediate Observed in a 1-Microsecond Simulation in Aqueous Solution, Science, 282 (5389), 740−744, 1998.

[6] A. Jaramillo-Botero, J. Su, Q. An, and W. A. Goddard III, Large-scale long-term nonadiabatic electron molecular dynamics for describing material properties and phenomena in extreme environments, *Journal of Computational Chemistry*, 32 (3), 497−512, 2011.

[7] A. K. Rappe and C. J. Casewit, *Molecular mechanics across chemistry*, University Science Books, 1997

[8] A.C.T. van Duin, S. Dasgupta, F. Lorant and W. A. Goddard III, ReaxFF: A Reactive Force Field for Hydrocarbons, *Journal of Physical Chemistry* A, 105(41): 9396−9409, 2001

[9] V. Rosato, M. Guillope, and B. Legrand, Thermodynamical and structural properties of fcc transition metals using a simple tight-binding model, *Philosophical Magazine A*, 59, 321−336, 1989.

[10] J. T. Su and W. A. Goddard III, Excited electron dynamics modeling of warm dense matter, *Physical Review Letter*, 99, 185003, 2007.

[11] N. L. Allinger, A hydrocarbon force field utilizing V_1 and V_2 torsion terms, *Journal of the American Chemical Society*, 99, 8127−8134, 1977.

[12] N. L. Allinger, Y. H. Yuh, J. H. Lii, Molecular mechanics. The MM3 force field for hydrocarbons, *Journal of the American Chemical Society*, 111, 8551−8566, 1989.

[13] J. H. Lii and N. L. Allinger, Molecular Mechanics. The MM3 force field for hydrocarbons. 2. Vibrational frequencies and thermodynamics, *Journal of the American Chemical Society*, 111, 8566−8575, 1989.

[14] H. Lii and N. L. Allinger, Molecular Mechanics. The MM3 force field for hydrocarbons. 3. The van der Waals' potentials and crystal data for aliphatic and aromatic hydrocarbons, *Journal of the American Chemical Society*, 111, 8576−8582, 1989.

[15] P. K. Weiner and P. A. Kollman, AMBER: Assisted model building with energy refinement. A general program for modeling molecules and their interactions, *Journal of Computational Chemistry*, 2, 287−303, 1981.

[16] B. R. Brooks, R. E. Bruccoleri, B.D. Olafson, D. J. States, S. Swaminathan, and M. Karplus, CHARMM: A program for macromolecular energy, minimization, and dynamics calculations, *Journal of Computational Chemistry*, 4, 187−217, 1983.

[17] W. F. van Gunsteren and H. J. C. Berendsen, Computer simulation of molecular dynamics: methodology, applications, and perspectives in chemistry, *Angew, Chem. Int. Ed. Engl.*, 29, 992−1023, 1990.

[18] B. R. Gelin and M. Karplus, Side-Chain torsional potentials: effects of dipeptide, protein, and solvent environment, *Biochemistry*, 18, 1256−1268, 1979.

[19] W. L. Jorgensen and J. Tirado-Rives, The OPLS Force Field for Proteins. Energy Minimizations for Crystals of Cyclic Peptides and Crambin, *Journal of the American Chemical Society*, 110 (6): 1657–1666, 1988.

[20] S. L. Mayo, B. D. Olafson, and W. A. Goddard III, DREIDING: A generic force field for molecular simulations, *Journal of Physical Chemistry*, 94, 8897−8909, 1990.

[21] A. K. Rappe, C. J. Casewit, K. S. Colwell, W. A. Goddard III, and W. M. Skiff, UFF, a Full Periodic Table Force Field for Molecular Mechanics and Molecular Dynamics Simulations, *Journal of the American Chemical Society*, 114, 10024−10035, 1992.

[22] M. Clark, R. D. Cramer III, and N. Van Opdenbosch, Validation of the general purpose Tripos 5.2 force field, *Journal of Computational Chemistry*, 10, 982−1012, 1989.

[23] K. Chenoweth, A.C.T. van Duin, and W.A. Goddard III, ReaxFF Reactive Force Field for Molecular Dynamics Simulations of Hydrocarbon Oxidation, *Journal of Physical Chemistry A*, 112, 1040−1053, 2008.

[24] A. Strachan, A.C.T. van Duin, S. Dasgupta, D. Chakraborty, and W.A. Goddard III, Shock Waves in High-Energy Materials: The Initial Chemical Events in Nitramine RDX, *Physical Review Letter*, 91, 098301, 2003.

[25] A.C.T. van Duin, A. Strachan, S. Stewman, Q. Zhang, and W.A. Goddard III, $ReaxFF_{SiO}$ Reactive Force Field for Silicon and Silicon Oxide Systems, *Journal of Physical Chemistry A*, 107, 3803−3811, 2003.

[26] Q. Zhang, T. Cagin, A.C.T. van Duin, and W.A. Goddard III, Adhesion and nonwetting-wetting transition in the Al/alpha-Al2O3 interface, *Physical Review B*, 69, 045423, 2004.

[27] K.D. Nielson, A.C.T. van Duin, J. Oxgaard, W. Deng, and W.A. Goddard III, Development of the ReaxFF Reactive Force Field for Describing Transition Metal

Catalyzed Reactions, with Application to the Initial Stages of the Catalytic Formation of Carbon Nanotubes, *Journal of Physical Chemistry A*, 109, 493−499, 2005.

[28] Q. An, S. V. Zybin, W. A. Goddard III, A. Jaramillo-Botero, M. Blanco, and S. N. Luo, Elucidation of the dynamics for hot-spot initiation at nonuniform interfaces of highly shocked materials, *Physical Review B*, 84, 220101, 2011.

[29] L.E. Chirlian and M.M. Francl, Atomic charges derived from electrostatic potentials: A detailed study, *Journal of Computational Chemistry*, 8, 894−905, 1987.

[30] A. K. Rappe and W. A. Goddard III, Charge Equilibration for Molecular Dynamics Simulations, *Journal of Physical Chemistry*, 95, 3358−3363, 1991.

[31] F. Cleri and V. Rosato, Tight-binding potentials for transition metals and alloys, *Physical Review B*, 48, 22−33, 1993

[32] A. P. Sutton and J. Chen, Long-range Finnis-Sinclair potentials, *Philosophical Magazine Letter*, 61, 139−146, 1990.

[33] M. W. Finnis and J. E. Sinclair, A Simple Empirical N-Body Potential For Transition-metals, *Philosophical Magazine A*, 50, 45−55, 1984

[34] E. Runge and E. K. U. Gross, Density functional theory for time dependent systems, *Physical Review Letter*, 52, 997−1000, 1984

Chapter 3 Anisotropic shock sensitivity of cyclotrimethylene trinitramine (RDX) from compress and shear reactive dynamics

3.1 Overview

We applied the compress-and-shear reactive dynamics (CS-RD) simulation model to study the anisotropic shock sensitivity of cyclotrimethylene trinitramine (RDX) crystal. We predict that for mechanical shocks between 3 and 7 GPa, RDX is most sensitive to shocks perpendicular to the (100) and (210) planes; while it is insensitive for shocks perpendicular to the (120), (111), and (110) planes. These results are all consistent with available experimental information, further validating the CS-RD model for distinguishing between sensitive and insensitive shock directions. We find that for sensitive directions the shock impact triggers a slip system that leads to large shear stresses arising from steric hindrance, causing increased energy inputs that increase the temperature, leading to dramatically increased chemical reactions. Thus our simulations demonstrate that the molecular origin of anisotropic shock sensitivity results from steric hindrance toward shearing of adjacent slip planes during shear deformation. Thus strain energy density, temperature rise, and molecule decomposition are effective measures to distinguish anisotropic sensitivities. We should emphasize that CS-RD has been developed as a tool to distinguish rapidly (within a few picoseconds) between sensitive and insensitive shock directions of energetic materials. If the high stresses and rates used here continued for much longer and for larger systems, they would ultimately result in detonation for all directions, but we have not demonstrated this.

3.2 Introduction

Energetic materials (EM) are critical to applications ranging from civil constructions and military armaments, to propulsion systems important in the aerospace and outer space industries. Effective strategies for developing new energetic materials with high energy density have led to drastic improvements. However there is little understanding about the origin of the detonation sensitivity of energetic materials that is important to safe storage and transport. Real energetic materials are heterogeneous with many interfaces, impurities, and defects, making it difficult to extract information about specific causes of sensitivity. A breakthrough was the experimental demonstration by Dick et al.[1–3] that large single crystals of pentaerythritol tetranitrate (PETN) display dramatically different sensitivities to shocks in different directions, so that one could ignore many complicating issues involving interfaces, impurities, and defects. For example, the pressure threshold of detonation perpendicular to the (100) shock plane is at least ~ 4 times that of the (110) shock plane for PETN[4]. In a previous report we developed the compress-and-shear reactive dynamics (CS-RD) strategy to examine the anisotropic shock sensitivity of PETN[5] using the ReaxFF reactive force field[6]. Our simulations showed drastically different sensitivities for various shock directions that agreed completely with available experimental observations. A second study for HMX[7] also showed excellent agreement between the predicted sensitive shock directions and experimental observations.

The anisotropic detonation sensitivity of single crystals is explained by various hypotheses such as steric hindrance[1] and the formation of dislocation pileup released by plasticity[8, 9]. There are some indentation experiments[10–16] and direct shock experiments [17, 18] on RDX crystals that suggest the possible slip systems under different shock directions. However, direct experimental investigation on anisotropic detonation sensitivity is challenging because it is hard to synthesize large single crystals and measure the anisotropic detonations that are required in such experiments. In this paper we use CS-RD to investigate the mechanism of sensitivity for the cyclotrimethylene trinitramine (RDX) single crystal for various shock directions.

3.3 Simulation methods and procedures

3.3.1 Simulation models

Three phases of RDX, α, β, and γ[19–23] have been identified experimentally. The most stable phase at ambient conditions is the α phase with orthorhombic symmetry (space group *Pbca*). The α phase transforms to the γ phase at ~ 4.5 GPa and 300 K, as detected by Raman spectroscopy[22,23]. The β phase is formed either by evaporation of boiling solvent containing RDX[24], deposition of RDX from solution on a glass substrate[25], or under high temperature above 470 K and high pressure above 3.6 GPa[23].

For our simulations we focus on the most stable α phase. Starting from a unit cell of α RDX crystal consisting of eight molecules with experimental lattice parameters[19], we relaxed the structure with NPT molecular dynamics using the ReaxFF reactive force field at 10 K and 0 GPa, using a time step of 0.1 fs for one ps. This leads to lattice parameters

of a = 13.392 Å, b = 11.828 Å, c = 11.238 Å, compared with experimental values at 300 K of a = 13.182 Å, b = 11.574 Å, and c = 10.709 Å.

We then compressed the RDX crystal uniaxially by 10% and 20% for various shock directions. This pre-compression leads to initial hydrostatic stresses between 3.0 and 7.0 GPa. Previous shock experiments on RDX[17, 18] measured the pressure over the range of P < 2.25 GPa and for 7 ~ 20 GPa. Considering the temperature increase and plastic deformation in real shock experiments, we consider that our simulations with direct 10% and 20% compression can be compared to real experiments.

We considered shocks perpendicular to five low-index planes: (100), (210), (111), (110), and (120). For the sake of computational convenience, we rotated the compressed unit cell for each case so that the *x*-*z* plane formed the slip plane and *x* formed the slip direction in a Cartesian coordinate system. We then expanded the unit cell to 10×10×2 supercells (1600 molecules or 33600 atoms) or 8×8×3 supercells (1536 molecules or 32256 atoms), which were used in reactive dynamics shear simulations.

3.3.2 Resolved shear stress

After compressing the 2×2×2 supercell of RDX crystal, we minimized the structure using the steepest descents for 5000 steps. Here the energy difference converged to < 10^{-9} kcal/mol after 1000 steps. Then we performed molecular dynamics minimization (NVT at 10 K) for one ps. After minimization, we averaged the full stress tensors over the structures obtained from the last 500 steps. We then projected this stress tensor onto various slip systems, defined by a combination of slip plane and direction, to obtain the resolved shear stresses (RSS) for each slip system. Since RSS reflects the driving force

for shear deformation, we expect that the slip systems with larger RSS are more likely to be activated. We expect also that the angles between the slip plane/direction and the shock plane/direction should be close to 45 degrees for the preferred slip system. Based on these criteria, we considered the largest RSS of the slip systems with angles in the range of 30 ~ 60 degrees. In addition we considered the possible slip systems suggested from previous experiments[17−23]. This led to 22 possible slip systems for 10% pre-compression and 24 slip systems for 20% pre-compression for the five shock directions on which we performed CS-RD simulations.

3.3.3 Compressive shear reactive dynamics

Starting with the compressed and minimized cells described above, we heated the systems from 10 K to 300 K over 0.2 ps to ensure that no chemical bonds were broken during heating. We then equilibrated the system with NVT for one ps at 300 K. We then expanded the unit cells to large supercells ($10\times10\times2$ or $8\times8\times3$) for each of the selected slip systems under the five shock directions (Table 3.12 and 3.13). Finally, we carried out shear deformation reactive dynamics (RD) on the compressed and rotated supercells for up to 10 ps by deforming the supercells every 10 timesteps at a constant shear rate 0.5/ps. No temperature constraint was applied during the shear RD.

3.3.4 Steric hindrance counter maps

A schematic illustration of the molecule contacts during shear deformation is shown in Figure 3-1. To examine the correlation between sensitivity and steric hindrance, we propose a geometry-based method to visualize and measure the extent of steric hindrance. First, we compressed the molecular crystal along a given shock direction. Then we

projected the geometry of molecules onto a plane that is perpendicular to both the shear plane and shear direction. We define a scoring scheme for molecule overlaps using covalent bond radius for each atom as follows: If molecules on adjacent planes overlap after projection, a point is given to the position on the project plane. Based on the overlap scores, we plot a 2D *steric hindrance contour map* where the overlapped regions indicate the areas where steric hindrance may occur during shear process. The areas of the overlapped regions are summed up, followed by normalization by the area of projected cross section. The ratio of overlapped regions relative to the projected cross section provides a quantitative measure of the extent of steric hindrance, hereafter denoted as the *steric hindrance index* (SHI). This SHI analysis method is efficient and independent of force fields, since it only requires crystal structures as input without the need of expensive dynamic simulations. On the other hand, SHI analysis based on rigid molecule geometry does not take into account geometry relaxation and chemical reactions.

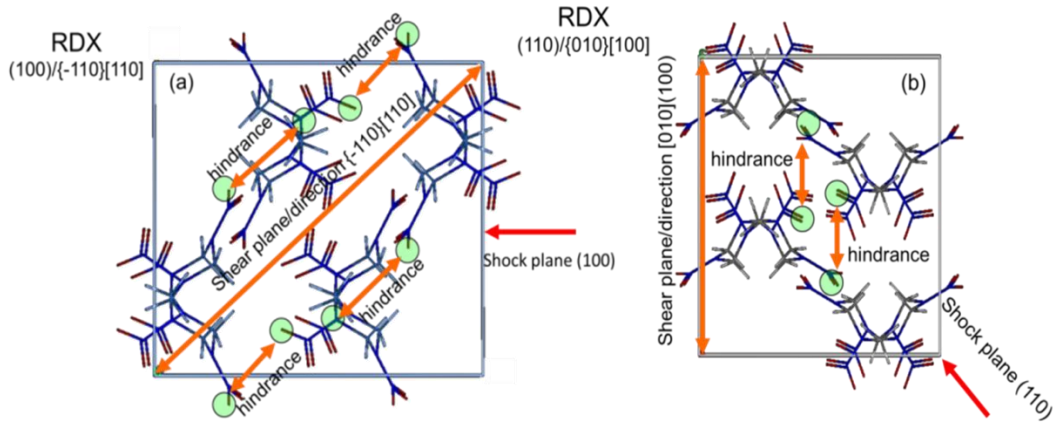

Figure 3.1 Unit cells of RDX crystal including schematic illustrations of molecule contacts during shear deformation: (a) sensitive shock plane (100) with slip system {-110}/ <110> with large steric hindrance; (b) insensitive shock plane (110) with slip system {010}/ <100> with small steric hindrance

3.3.5 Bond fragment analysis

For the analysis of numerous reactions during the ReaxFF simulation, we need a systematic criterion to identify molecular fragments. To enable the automatic and systematic analysis of chemical reactions from ReaxFF simulation trajectories, we developed a molecular fragment analysis program, *BondFrag*. One general criterion determining the atomic connectivity is based on the comparison of inter-atomic distances with the van der Waals (vdW) radii. However, it is inadequate to apply the vdW radii defined under ambient conditions into the highly compressed and detonative conditions. Instead, we used the bond-order values defined in ReaxFF, ranging 0 to 1 for the systems considered here, to provide a quantitative criterion for defining the presence of chemical bonds. We optimized the bond order cutoff values from simulations of several energetic materials systems. These cutoff values are tabulated at Table 3.1 for various atom pairs.

Table 3.1 Bond order cutoff values for different atom pairs. *BondFrag* program uses these values as a default parameter set (can be adjusted by the user) to determine molecular fragments.

	C	**H**	**O**	**N**
C	0.55	0.40	0.80	0.30
H		0.55	0.40	0.55
O			0.65	0.55
N				0.45

To ignore instantaneous fluctuations that might appear to dissociate (or form) a bond, we excluded the newly created (or annihilated) bond if it was annihilated (or created) again within the time window of one ps from our fragment analysis.

After determining the molecular fragments based on bond-order cutoff values and a time window of one ps, the *BondFrag* program assigns unique identification numbers into molecular fragments to trace the reaction pathways and calculate the molecular properties such as a center-of-mass, dipole moments, and molecular charges.

3.4 Results and discussions

3.4.1 Resolved shear stress

We calculated the stress tensors of the minimized and compressed crystals for the five shock planes under consideration. Then we projected the stress tensor onto all the low-index slip systems ranging from {-2-2-2} to {222} to obtain the RSS of each slip system for each shock plane. Table 3.2 to Table 3.11 shown below list the RSS results of some selected slip systems for five shock planes under two pre-compressions, together with the angles between shock plane/slip plane (φ) and shock direction/slip direction (ψ) for the possible slip systems.

Previous solution-etch pitting experiments[11] on RDX crystal suggested that (010) is the primary slip plane, which was confirmed by x-ray crystallography studies [16]. Microindentation experiments on the (120), (010), (111), and (-210) planes indicated that {021}/<100> is an alternative primary slip system[12–15]. The recent nanoidentation experiment also suggested that {011}/<100> is a slip system[10,12,15]. In addition, {021}/±<01-2> were also suggested as possible slip systems based on geometric considerations of intermolecular displacement[12–16].

Table 3.2 Slip systems considered based on minimized systems with 10% compression for (100) shock. Resolved shear stress (RSS), angle of shock plane/slip plane (φ), and angle of shock direction/slip direction (ψ) after minimization of 10% compression under (100) shock. Since no slip systems were observed for (100) shock, the two slip systems with large RSS and good angles (close to 45 degree; marked by asterisks) were selected for CS-RD simulations. Table.1 shows that these two directions lead to very similar CS-RD results. The stress tensor (Pxx, Pyy, Pzz, Pxy, Pyz, Pxz) = (4.14, 1.52, 2.42, 0.01, -0.02, -0.01) GPa is used to calculate RSS.

Slip plane	Slip direction	φ	ψ	RSS (GPa)
*{110}	<1-10>	45.54	44.46	1.31
*{-110}	<110>	134.46	44.46	1.31
{110}	<111>	45.54	53.55	1.08
{210}	<1-20>	26.70	63.00	1.06
{120}	<-210>	63.86	153.86	1.04
{101}	<10-1>	47.00	43.00	0.86
{20-1}	<102>	28.20	61.80	0.71
{2-10}	<001>	26.70	90.00	0.01

Table 3.3 Slip systems considered based on minimized systems with 10% compression for (210) shock. Resolved shear stress (RSS), angle of shock plane/slip plane (φ), and angle of shock direction/slip direction (ψ) after minimization of 10% compression under (210) shock. The six slip systems marked by asterisks were selected for CS-RD simulations. These five cases with low RSS were selected because they had previously been suggested as possible slip systems for (210) shock. The CS-RD finds that the top-selected slip system is preferred. The stress tensor (Pxx, Pyy, Pzz, Pxy, Pyz, Pxz) = (3.38, 1.72, 1.97, 0.45, 0.00, 0.00) GPa is used to calculate RSS.

Slip plane	Slip direction	φ	ψ	RSS (GPa)
*{120}	<-210>	33.82	123.82	0.94
*{010}	<100>	57.83	32.17	0.59
*{021}	<100>	67.71	32.17	0.53
*{0-21}	<100>	118.29	32.17	0.53
{102}	<20-1>	68.33	39.56	0.51
{100}	<010>	27.00	63.00	0.45
*{011}	<100>	68.16	32.17	0.41
*{0-11}	<100>	111.84	32.17	0.41
{100}	<011>	27.00	71.01	0.32
{100}	<012>	27.00	78.02	0.20
{021}	<0-12>	67.71	101.98	0.08

Table 3.4 Slip systems considered based on minimized systems with 10% compression for (111) shock. Resolved shear stress (RSS), angle of shock plane/slip plane (φ), and angle of shock direction/slip direction (ψ) after minimization of 10% compression under (111) shock. The seven slip systems marked by asterisks were selected for CS-RD simulations. These seven slip systems had previously been suggested as possible slip systems for (111) shock. The CS-RD finds that the second-selected slip system is preferred. The stress tensor (Pxx, Pyy, Pzz, Pxy, Pyz, Pxz) = (2.04, 1.18, 2.13, 0.14, 0.39, 0.16) GPa is used to calculate RSS.

Slip plane	Slip direction	φ	ψ	RSS (GPa)
*{011}	<100>	28.70	61.30	0.38
{001}	<100>	48.76	61.30	0.38
{001}	<110>	48.76	41.80	0.36
{100}	<011>	55.94	34.19	0.36
*{021}	<100>	33.16	61.30	0.33
*{010}	<001>	51.94	54.63	0.19
*{010}	<100>	51.94	61.30	0.18
*{0-11}	<100>	100.71	118.70	0.16
*{001}	<010>	48.76	56.78	0.10
*{0-21}	<100>	104.87	118.70	0.02

Table 3.5 Slip systems considered based on minimized systems with 10% compression for (110) shock. Resolved shear stress (RSS), angle of shock plane/slip plane (φ), and angle of shock direction/slip direction (ψ) after minimization of 10% compression under (110) shock. The three slip systems marked by asterisks were selected for CS-RD simulations. These three slip systems had previously been suggested as possible slip systems at ambient conditions. The CS-RD finds that the top selected slip system is preferred. The stress tensor (Pxx, Pyy, Pzz, Pxy, Pyz, Pxz) = (2.52, 1.63, 1.89, 0.30, 0.00, -0.01) GPa is used to calculate RSS.

Slip plane	Slip direction	φ	ψ	RSS (GPa)
*{010}	<100>	38.48	51.52	0.39
*{021}	<100>	45.44	51.52	0.35
{0-21}	<100>	134.56	51.52	0.35
{100}	<010>	45.54	44.46	0.30
{101}	<10-1>	62.41	62.10	0.30
{010}	<101>	38.48	62.10	0.28
*{011}	<100>	56.19	51.52	0.27
{0-11}	<100>	123.81	51.52	0.27
{100}	<011>	45.54	59.78	0.21
{001}	<100>	90.00	51.52	0.00
{001}	<010>	90.00	44.46	0.00
{100}	<001>	45.54	90.00	0.00

Table 3.6 Slip systems considered based on minimized systems with 10% compression for (120) shock. Resolved shear stress (RSS), angle of shock plane/slip plane (φ) and angle of shock direction/slip direction (ψ) after minimization of 10% compression under (120) shock. The four slip systems marked by asterisks were selected for CS-RD simulations. Three cases were selected despite a low RSS because they had previously been suggested as possible slip systems in ambient conditions. The CS-RD finds that the second-selected slip system is preferred. The stress tensor (Pxx, Pyy, Pzz, Pxy, Pyz, Pxz) = (1.48, 2.18, 1.92, 0.55, -0.03, -0.03) GPa is used to calculate RSS.

Slip plane	Slip direction	φ	ψ	RSS (GPa)
*{-120}	<210>	44.64	45.36	0.65
{100}	<010>	63.86	26.14	0.55
*{010}	<100>	21.68	68.32	0.49
{-110}	<110>	62.91	27.09	0.49
{201}	<010>	67.65	26.14	0.46
*{0-21}	<100>	146.87	68.32	0.45
{021}	<100>	33.13	68.32	0.43
{100}	<0-11>	63.86	128.57	0.40
*{0-11}	<100>	132.04	68.32	0.37
{011}	<100>	47.96	68.32	0.33
{012}	<100>	64.63	68.32	0.20
{102}	<-201>	80.03	70.14	0.19
{102}	<010>	80.03	26.14	0.19

Table 3.7 Slip systems considered based on minimized systems with 20% compression for (100) shock. Resolved shear stress (RSS), angle of shock plane/slip plane (φ), and angle of shock direction/slip direction (ψ) after minimization of 20% compression under (100) shock. Since no slip systems were observed for (100) shock, four slip systems with large RSS and good angle (close to 45 degree) marked by asterisks were selected for CS-RD simulations. The CS-RD finds that the third-selected slip system is preferred. The stress tensor (Pxx, Pyy, Pzz, Pxy, Pyz, Pxz) = (10.48, 7.12, 5.31, 0.02, 0.03, -0.15) GPa is used to calculate RSS.

Slip plane	Slip direction	φ	ψ	RSS (GPa)
*{101}	<10-1>	43.63	46.37	2.58
*{-101}	<101>	136.37	46.37	2.58
*{110}	<1-10>	42.17	47.83	1.67
*{-110}	<110>	137.83	47.83	1.67
{120}	<-210>	61.10	151.10	1.45
{210}	<1-20>	24.37	65.64	1.19
{130}	<-310>	69.80	159.8	1.14
{310}	<1-30>	16.80	73.20	0.85
{2-10}	<001>	24.37	90.00	0.13

Table 3.8 Slip systems considered based on minimized systems with 20% compression for (210) shock. Resolved shear stress (RSS), angle of shock plane/slip plane (φ), and angle of shock direction/slip direction (ψ) after minimization of 20% compression under (210) shock. The six slip systems marked by asterisks were selected for CS-RD simulations. Five cases with low RSS were selected because they had previously been suggested as possible slip systems. The CS-RD finds that the top-selected slip system is preferred. The stress tensor (Pxx, Pyy, Pzz, Pxy, Pyz, Pxz) = (8.70, 5.19, 5.57, -0.12, 0.09, 0.04) GPa is used to calculate RSS.

Slip plane	Slip direction	φ	ψ	RSS (GPa)
*{120}	<-210>	30.77	126.88	1.61
*{010}	<100>	54.72	35.29	0.54
*{021}	<100>	58.80	35.29	0.52
*{0-21}	<100>	121.20	35.29	0.45
*{011}	<100>	65.73	35.29	0.44
*{0-11}	<100>	114.27	35.29	0.33
{021}	<0-12>	58.80	100.68	0.20
{100}	<010>	24.37	65.64	0.12
{100}	<011>	24.37	72.99	0.02
{100}	<012>	24.37	79.32	0.02

Table 3.9 Slip systems considered based on minimized systems with 20% compression for (111) shock. Resolved shear stress (RSS), angle of shock plane/slip plane (φ), and angle of shock direction/slip direction (ψ) after minimization of 20% compression under (111) shock. The six slip systems marked by asterisks were selected for CS-RD simulations. These six slip system had previously been suggested as possible slip systems. {0-11}/<100> slip system is not selected due to the small RSS although it was suggested by a previous study. The CS-RD finds that the second selected slip system is preferred. The stress tensor (Pxx, Pyy, Pzz, Pxy, Pyz, Pxz) = (7.01, 5.85, 5.77, 0.83, 0.72, 0.45) GPa is used to calculate RSS.

Slip plane	Slip direction	φ	ψ	RSS (GPa)
*{011}	<100>	25.95	64.05	1.16
*{021}	<100>	30.15	64.05	1.12
{001}	<110>	45.40	45.17	1.10
{100}	<011>	52.75	37.38	1.10
{001}	<100>	45.40	64.05	0.89
*{010}	<100>	47.71	64.05	0.88
{100}	<001>	52.75	57.74	0.72
*{010}	<001>	47.71	57.74	0.55
*{001}	<010>	45.40	64.05	0.55
*{0-21}	<100>	106.62	115.95	0.40
{0-11}	<100>	86.87	115.95	0.05

Table 3.10 Slip systems considered based on minimized systems with 20% compression for (110) shock. Resolved shear stress (RSS), angle of shock plane/slip plane (φ), and angle of shock direction/slip direction (ψ) after minimization of 20% compression under (110) shock. The four slip systems marked by asterisks were selected for CS-RD simulations. Three of these cases were selected despite a low RSS because they had previously been suggested as possible slip systems at ambient conditions. The CS-RD finds that the second-selected slip system is preferred. The stress tensor (Pxx, Pyy, Pzz, Pxy, Pyz, Pxz) = (9.93, 6.00, 4.53, 0.26, 0.02, 0.00) GPa is used to calculate RSS.

Slip plane	Slip direction	φ	ψ	RSS (GPa)
*{101}	<10-1>	59.55	64.80	2.63
*{010}	<100>	35.24	54.76	1.07
*{021}	<100>	42.07	54.76	0.98
{0-21}	<100>	137.93	54.76	0.97
*{011}	<100>	53.00	54.76	0.80
{010}	<101>	35.24	64.80	0.79
{0-11}	<100>	127.00	54.76	0.78
{100}	<010>	42.17	47.83	0.26
{100}	<011>	42.17	62.63	0.19
{010}	<001>	35.24	90.00	0.00
{001}	<100>	90.00	54.76	0.02
{001}	<010>	90.00	47.83	0.00
{100}	<001>	42.17	90.00	0.02

Table 3.11: Slip systems considered based on minimized systems with 20% compression for (120) shock. Resolved shear stress (RSS), angle of shock plane/slip plane (φ), and angle of shock direction/slip direction (ψ) after minimization of 20% compression under (120) shock. The four slip systems marked by asterisks were selected for CS-RD simulations. Three cases were selected despite a low RSS because they had previously been suggested as possible slip systems at ambient conditions. The CS-RD finds that the second-selected slip system is preferred. The stress tensor (Pxx, Pyy, Pzz, Pxy, Pyz, Pxz) = (5.11, 5.99, 4.74, 1.26, 0.03, -0.05) GPa is used to calculate RSS.

Slip plane	Slip direction	φ	ψ	RSS (GPa)
*{-120}	<210>	41.28	48.73	1.33
{100}	<010>	61.10	28.90	1.26
{201}	<010>	22.66	28.90	1.07
*{010}	<100>	19.46	70.54	1.05
*{021}	<100>	30.12	70.54	0.98
{-110}	<110>	60.08	29.92	0.97
{0-21}	<100>	149.88	70.54	0.95
*{011}	<100>	44.59	70.54	0.82
{100}	<0-11>	61.102	125.33	0.81
{0-11}	<100>	135.41	70.54	0.77
{012}	<100>	61.92	70.54	0.56
{102}	<010>	78.81	28.90	0.46
{110}	<1-10>	14.26	104.26	0.36
{102}	<-201>	78.81	72.20	0.09

We chose six possible slip systems for the (210) shock: {120}/<-210>, {021}/<100>, {0-21}/<100>, {010}/<100>, {011}/<100>, and {01-1}/<100>. The {120}/<-210> slip system has the largest RSS with the angle in the range of 30 ~ 60 degrees, while the other five slip systems were proposed in previous study[18].

For the (111) shock, we chose the five slip systems proposed for (210) shock above, {010}/<001> as suggested by Dang et al.[18], and {001}/<100> as suggested by previous non-reactive force-field MD simulation[26].

No slip systems were suggested experimentally for (100) shocks, so we chose the slip systems with the largest RSS and appropriate angles between 30 and 60 degrees.

For the shock planes (120) and (210), we chose the slip systems with the largest RSS and angles in the range of 30 ~ 60 degrees or those that were suggested in previous nanoidentation experiments[19–23].

All together we chose 22 slip systems for the five shock planes: two slip systems for (100) shock, six for (210) shock, seven for (111) shock, four for (120) shock, and three for (110) shock, respectively, as listed in Table 3.12.

3.4.2 Compressive shear reactive dynamics

The hint that shear deformation is critical to understanding sensitivity of energetic materials was provided by Plazkins's experiment showing the initiation of detonation along directions with the maximum shear stress[27]. The CS-RD model was developed to mimic the shock process by first compressing the crystals (by 10% and 20%), followed by shear deformation along various slip systems. For the selected slip systems, we compressed the crystals and equilibrated for 1 ps NVT MD at T = 300 K. This leads to

calculated total pressures of 2.6−3.2 GPa after 10% compression and 7.0−7.6 GPa after 20% compression. We focus our discussions on the shear simulations from the 10% compression since α phase is still the most stable phase under the pressure of 2.6 ~ 3.2 GPa. We also present the results of 20% compression-shear simulations which correspond to the multiple shock experiments leading to decomposition[18]. The results of 10% and 20% compression are compared to examine the effects of compression ratio.

Table 3.12 (10% pre-compression) tabulates the results from shear simulations for the 22 selected slip systems, while Table 3.13 (20% pre-compression) does the same for the 24 slip systems. For each of the for five shock planes we selected the most probable slip system, with the results summarized in Fig. 3.2 (10% pre-compression) and Fig. 3.6 (20% pre-compression). These results from the early stage of the shear process are expected to be important in understanding the anisotropic sensitivity under mechanical shock compression.

Table 3.12 Results from CS-RD simulations on the 22 slip systems selected for the five shock directions based on 10% compression-shear. The shear stress barrier over initial shear stress $(\tau_{max} - \tau_0)/\tau_0$ represents the shear driving force required to initiate shear along a slip system. We used this relative stress barrier to predict the slip system expected to prevail for each shock direction, which is marked by an asterisk (*). The strain energy density (W) is the imposed mechanical work required to initiate shear deformation over 4 ps. This strain energy density indicates the extra work needed to overcome the stress barrier, and correlates directly with sensitivity. Also shown are the temperatures at 8 ps, the reaction product ratio, NO_2/RDX at 10 ps, and the stress overshoot.

Sensitivity	Shock plane	Slip system	T (K) at 8 ps	NO_2/RDX (%) at 10 ps	$\tau_{max} - \tau_c$ (GPa)	$(\tau_{max} - \tau_0)/\tau_0$	W (GPa)
sensitive	**(210)**	***{120}<-210>**	**1177**	**3.67**	**0.55**	**0.9**	**1.26**
		{0-21}<100>	1107	1.85	0.44	3.0	1.12
		{021}<100>	1096	1.80	0.44	3.2	1.12
		{010}<100>	1101	2.63	0.43	4.2	1.07
		{0-11}<100>	1132	2.80	0.37	5.0	1.16
		{011}<100>	1128	1.82	0.37	5.0	1.15
sensitive	**(100)**	***{-110}<110>**	**1165**	**2.81**	**0.69**	**1.0**	**1.25**
		{110}<1-10>	1173	3.76	0.60	1.2	1.25
insensitive	**(111)**	***{021}<100>**	**1098**	**1.90**	**0.47**	**3.3**	**1.15**
		{010}<100>	1071	1.19	0.35	4.4	1.06
		{011}<100>	1143	2.78	0.58	5.6	1.14
		{010}<001>	1163	3.38	1.17	5.6	1.27
		{0-21}<100>	1064	1.55	0.42	5.9	1.03
		{001}<010>	985	0.05	0.16	10.7	0.93
		{0-11}<100>	1115	2.41	0.47	14.5	1.15
insensitive	**(120)**	***{010}<100>**	**1094**	**1.44**	**0.31**	**2.1**	**1.08**
		{0-21}<100>	1117	2.34	0.40	2.6	1.13
		{-120}<210>	1200	4.84	0.92	2.9	1.36
		{0-11}<100>	1140	2.28	0.47	3.1	1.19
insensitive	**(110)**	***{010}<100>**	**1093**	**1.63**	**0.42**	**1.4**	**1.15**
		{021}<100>	1102	2.27	0.41	2.1	1.12
		{011}<100>	1134	2.60	0.45	3.5	1.17

Table 3.13 Results from CS-RD simulations on the 24 slip systems selected for the five shock directions based on 20% compression-shear. The shear stress barrier over the initial shear stress (τ_{max}- τ_0)/ τ_0 represents the shear driving force required to initiate shear along a slip system. We use this relative stress barrier to predict the slip system expected to prevail for each shock direction, which is marked by an asterisk (*). The strain energy density (W) is the imposed mechanical work required to initiate shear deformation over 3 ps. This strain energy density indicates the extra work needed to overcome the stress barrier, and correlates directly with sensitivity. Also shown are the temperatures at 5 ps, the reaction product ratio, NO_2/RDX at 8 ps, and the shear stress overshoot.

Sensitivity	Shock plane	Slip system	T (K) at 5 ps	NO_2/RDX (%) at 8 ps	$\tau_{max} - \tau_c$ (GPa)	($\tau_{max} - \tau_0$)/ τ_0	W (GPa)
sensitive	**(100)**	***{110}<1-10>**	**1199**	**21.2**	**1.61**	**0.7**	**1.67**
		{-110}<110>	1185	17.2	1.51	0.8	1.65
		{101}<10-1>	1095	11.8	0.47	2.6	1.49
		{-101}<101>	1109	13.4	0.43	2.6	1.50
sensitive	**(210)**	***{120}<-210>**	**1131**	**11.7**	**0.85**	**1.9**	**1.62**
		{021}<100>	1017	5.6	0.45	2.3	1.33
		{010}<100>	992	5.0	0.72	2.4	1.27
		{0-21}<100>	1039	7.5	0.40	2.7	1.33
		{011}<100>	1054	9.3	0.50	2.9	1.38
		{0-11}<100>	1054	8.9	0.53	4.3	1.41
insensitive	**(111)**	***{021}<100>**	**1045**	**8.1**	**0.65**	**2.6**	**1.42**
		{010}<001>	1056	8.1	0.94	2.9	1.44
		{001}<010>	986	5.1	0.36	3.5	1.31
		{0-21}<100>	971	3.9	0.36	3.8	1.23
		{011}<100>	1128	14.3	0.73	4.8	1.43
		{010}<100>	957	4.5	0.27	8.7	1.27
insensitive	**(120)**	***{010}<100>**	**1018**	**5.3**	**0.94**	**1.9**	**1.37**
		{-120}<210>	1167	17.2	1.81	2.0	1.77
		{021}<100>	1052	9.1	1.10	2.5	1.47
		{011}<100>	1092	10.4	1.19	3.1	1.56
insensitive	**(110)**	***{010}<100>**	**979**	**5.1**	**0.38**	**1.2**	**1.24**
		{101}<10-1>	1139	17.4	0.75	1.2	1.61
		{021}<100>	1041	7.4	0.82	1.3	1.39
		{011}<100>	1091	10.4	0.78	1.9	1.50

The criterion to select most probable slip systems is the shear-stress barrier with respect to the initial shear stress, $(\tau_{max}^{-} \tau_0)/\tau_0$. This relative stress barrier correlates with the initial driving force required to activate a slip system. We expect that the slip system with minimum relative stress barrier would be more likely to be activated. It may be possible to trigger multiple slip systems for a particular shock, but we only choose the most probable slip system for further comparisons of sensitivities among various shock directions. Based on the relative shear-stress barrier, we chose five most probable slip systems corresponding to the five shock directions: {-110}/<110> for (100) shock, {120}/<-210> for (210) shock, {021}/<100> for (111) shock, {010}/<100> for (120) shock, and {010}/<100> for (110) shock under 10% pre-compression.

Shear deformation imposes mechanical work into the systems which we determine from the total integrated energy to induce shearing until the shear stress is a constant for all directions. The imposed mechanical work can be quantified by strain energy density that is obtained by integrating the shear stress along stress-strain curve before most mechanical work converts to thermal and chemical energies. Since the shear rate in our simulation is constant (0.5/ps), the integration can be carried out using the stress-time curve [Fig. 3.2(b) and Fig. 3.6(b)] and converting the time to the shear strain. We did the integration to four ps for 10% pre-compression and to three ps for 20% pre-compression when the shear stresses converged to constant values for all five shock directions.

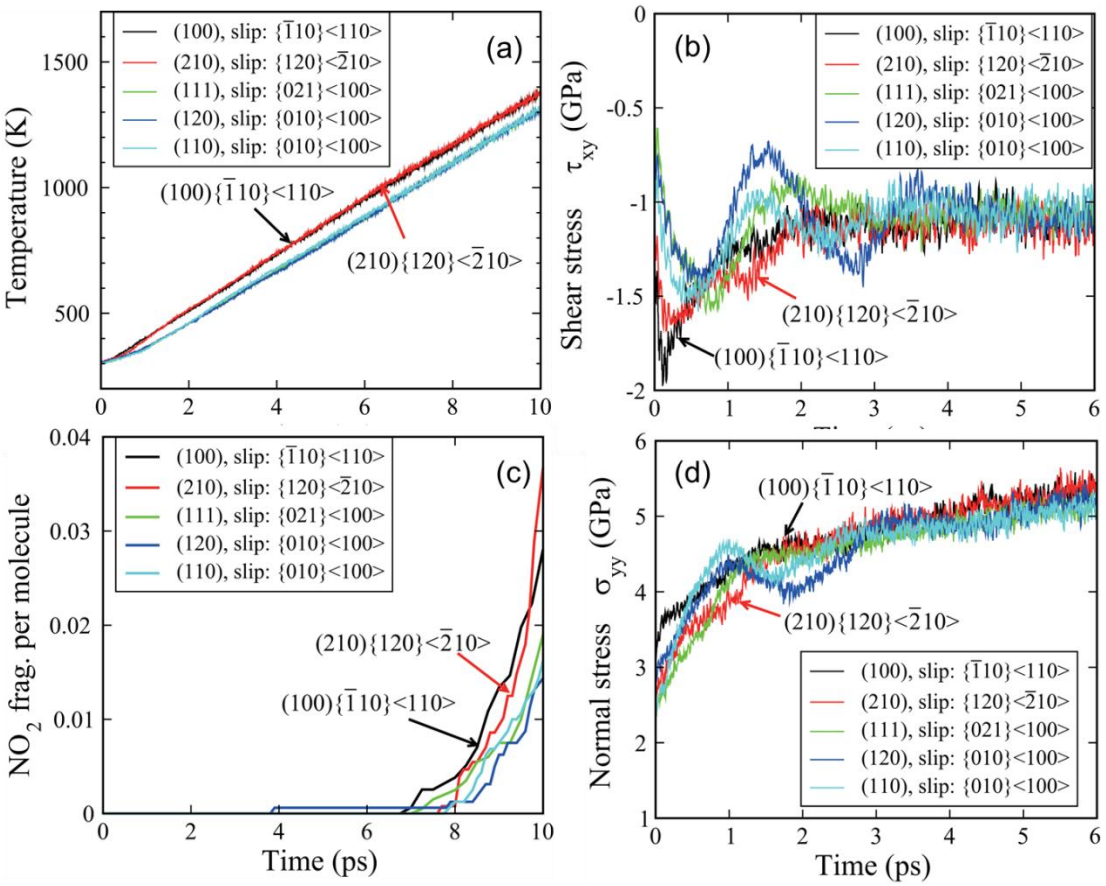

Figure 3.2 CS-RD results for the preferred slip system predicted for each of the five shock directions (after 10% pre-compression). (a) Temperature, (b) shear stress, (c) NO_2 products, and (d) normal stress as a function of time under the five shock directions in shear simulation. These calculations identify the (210)/{120}<-210> and (100)/{-110}<110> shock/slip systems as the two most sensitive cases. In both cases the large shear stress overshoot in (b) for 0 to 0.5 ps results from an initial bad steric overlap. This bad steric contact is manifested in the large normal stress observed for 0−0.5 ps in (d). The external mechanical work necessary to overcome the large stress barrier (see Fig. 3.3c) induces the larger temperature increase by 1 ps compared with the other slip systemsm as shown in (a). This extra temperature remains for the rest of the simulation, leading to significantly more molecule decomposition starting at 7 ps, as shown in (c).

For 10% pre-compression, the (100) and (210) shock led to strain energy density 1.25 GPa and 1.26 GPa, respectively. The (111), (120), and (110) shocks led to smaller strain energy densities: 1.15 GPa, 1.08 GPa, and 1.15 GPa, respectively. The large strain energy density for (100) and (210) shocks correlates with their large sensitivity because it indicates that more mechanical work is imposed, some of which would in turn convert to thermal or chemical energies, leading to higher temperatures and more chemical decompositions until detonation. For sensitive directions, more mechanical work is required during the shearing process. After molecules overcome the first large barriers (before 4 ps), the shear stress decreases, indicating that some imposed mechanical work converts to heat continuously being used to break chemical bonds starting at ~ 6.5 ps.

Figure 3-2 shows the evolution of temperature, NO_2 production, shear stress, and normal stress (σ_{yy}) during the 10 ps shear simulations for 10% pre-compression. We found that temperature increased most significantly, from 300 K to 1165 K after 8 ps for the (100) shock and {-110}/<110> slip system, and to 1177 K for the (210) shock and {120}/<-210> slip system. The temperatures increased moderately to 1098 K for the (111) shock and {021}/<100> slip system, to 1094 K for the (120) shock and {010}/<100> slip system, and to 1093 K for the (110) shock and {010}/<100> slip system. The temperature rises also indicate that (100) and (210) are the most sensitive shock directions, whereas (120), (110), and (111) are the insensitive shock directions.

To track the chemical processes as the CS-RD process of RDX, we analyze the molecular fragments from the corresponding ReaxFF MD trajectories based on a bond-order cutoff criterion. The sensitivity prediction based on the strain energy density is

further supported by the fragment analysis for NO_2, the product of the initial dissociation of RDX under shock compression. Figure 3.2c shows that the most sensitive (100) and (210) shocks led to 2.81% and 3.67% NO_2 per RDX molecule at 10 ps, respectively. On the other hand, the less-sensitive (111), (120), and (110) shocks led to 1.90%, 1.44%, and 1.63% NO_2/RDX, respectively. We found that the NO_2 production mainly occurs after 6.5 ps when temperature increases above 1000 K.

The overshooting of the shear stress, defined as τ_{max}- τ_c, is correlated to the imposed mechanical work during shear. The most sensitive (100) and (210) shock led to a shear stress overshoot of 0.69 GPa and 0.55 GPa, respectively, the largest among all shock directions. The less sensitive (111), (120), and (110) shocks led to stress overshoots of 0.47 GPa, 0.31 GPa, and 0.42 GPa respectively.

The shear-stress barrier measures the energy barrier of shear deformation. As Fig. 3.2b shows, the shear stresses maximize within the first ps. For the most-sensitive (100) shock, the shear stress maximizes at ~ 0.2 ps and then relaxes to constant values. On the other hand, for the less-sensitive (120) shocks, the shear stress oscillates before relaxing to constant values. This indicates that the shear deformation encounters several small energy barriers in these slip systems. The normal stress shown in Fig. 3.2d also indicates the dramatic difference in various slip systems.

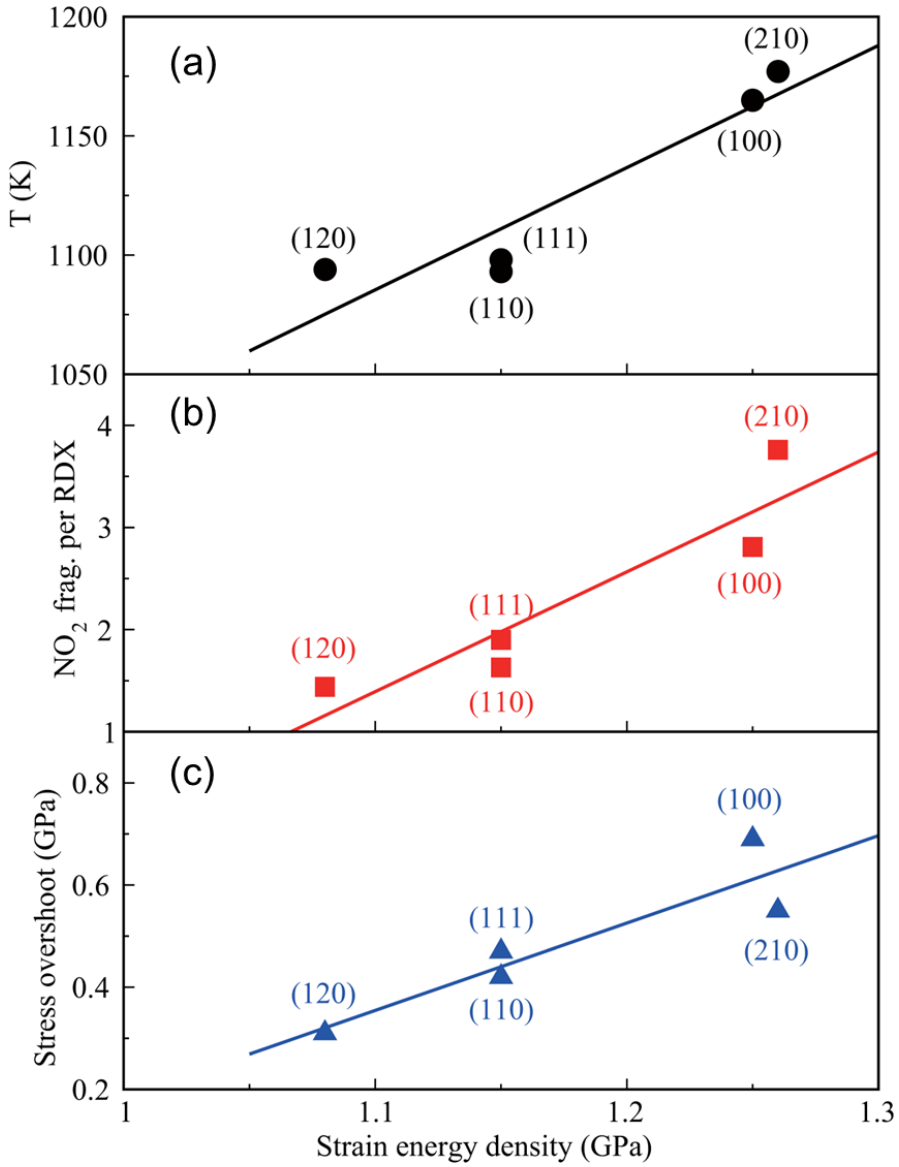

Figure 3.3: Correlations between strain energy density (integration of shear stress up to 4.0 ps in Fig. 2b) and other sensitivity measurements for 10% pre-compression: (a) temperature at 8 ps, (b) NO_2 production at 10 ps, (c) stress overshoot during CS-RD. The large strain energy density for the (210) and (100) shock planes leads to the large temperature increase, the increased NO_2 dissociation, and the large stress overshoot during CS-RD. This makes these the sensitive shock directions and indicates that strain energy density is the determining factor for sensitivity.

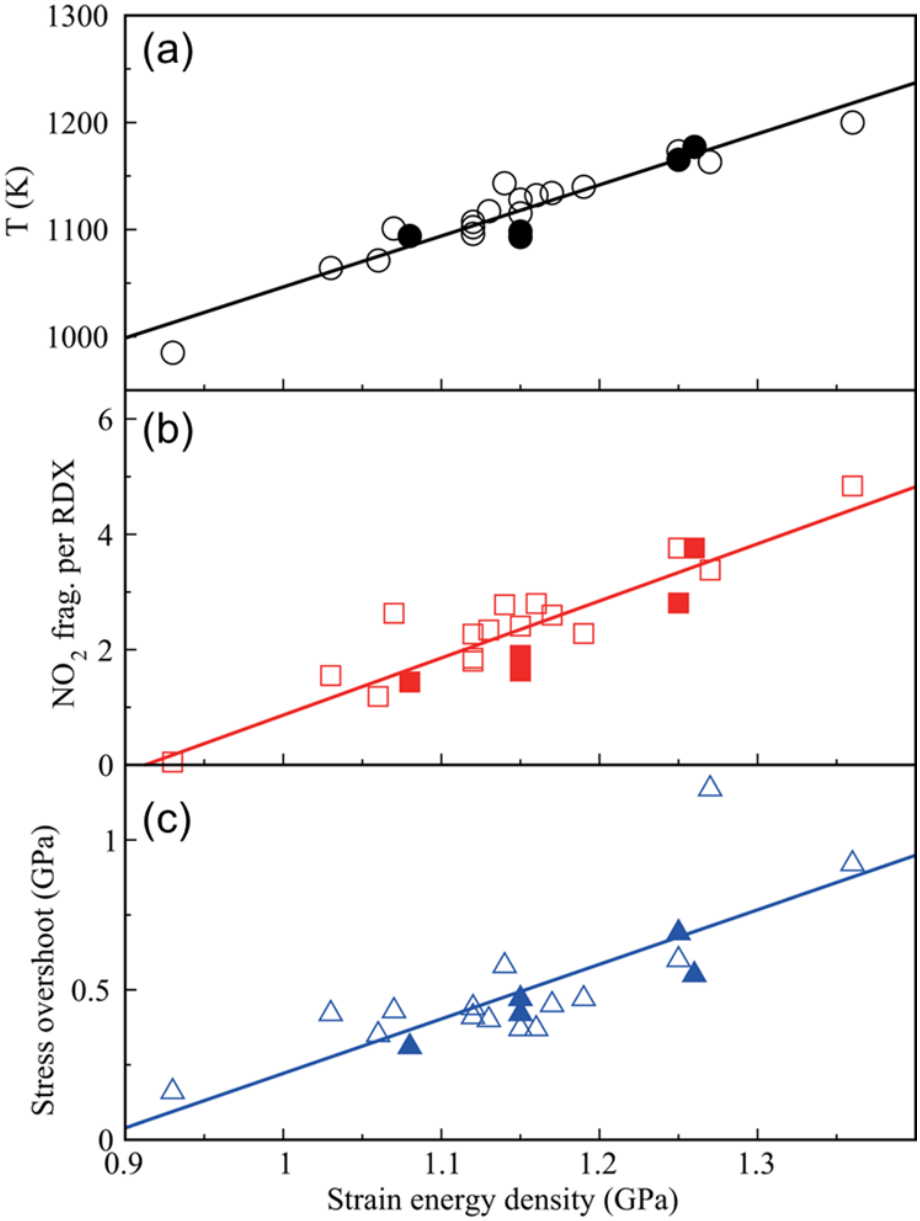

Figure 3.4 Correlations between strain energy density (integration of shear stress up to 4.0 ps in Fig. 2b) and other sensitivity measurements for all the CS-RD cases for 10% pre-compression: (a) temperature at 8 ps, (b) NO_2 production at 10 ps, (c) stress overshoot during CS-RD. The strain energy density shows a linear relationship with other sensitivity measurements. The filled symbols are the results of selected possible slip system for the five shock planes shown in Fig. 3.3.

Fig. 3.3 (10% pre-compression) and Fig. 3.7 (20% pre-compression) show good correlations between strain energy density and temperature, NO_2 population, and stress overshoot. Results of all the CS-RD simulations summarized in Fig. 3.4 show clearly a linear relationship between the strain energy density and temperature, NO_2 production, and stress overshoot. The imposed mechanical work is the origin of the temperature increase and NO_2 production for various shock directions. Since shear stresses converge to similar values when the system becomes amorphous, the strain energy density integrated at an early stage represents mostly the characteristics of energy landscape specific to a given shock and slip system. Thus the strain energy density can be a useful criterion with which to distinguish the anisotropic sensitivities among various shock directions. After overcoming the initial stress barriers, the temperature rise and molecule decomposition become major measurements for sensitivity, since the thermal energy and chemical energy, together with residual strain energy, comes from the imposed mechanical work.

The process of shear deformation is described as follows. First, molecules on adjacent slip planes are pushed into each other as they shear along a given slip direction, indicated by the increased shear stress. After passing through the first energy barrier (< 1 ps), there are few additional barriers to overcome. After about three ps, the system becomes amorphous, as indicated by radial distribution functions (RDF) and coordination numbers (CN) shown in Fig. 3.5 for the (100) shock and {-110}/<100> slip system. The work done to overcome molecular interactions raises the temperature until it is high enough to break the N-N bonds to form NO_2 products.

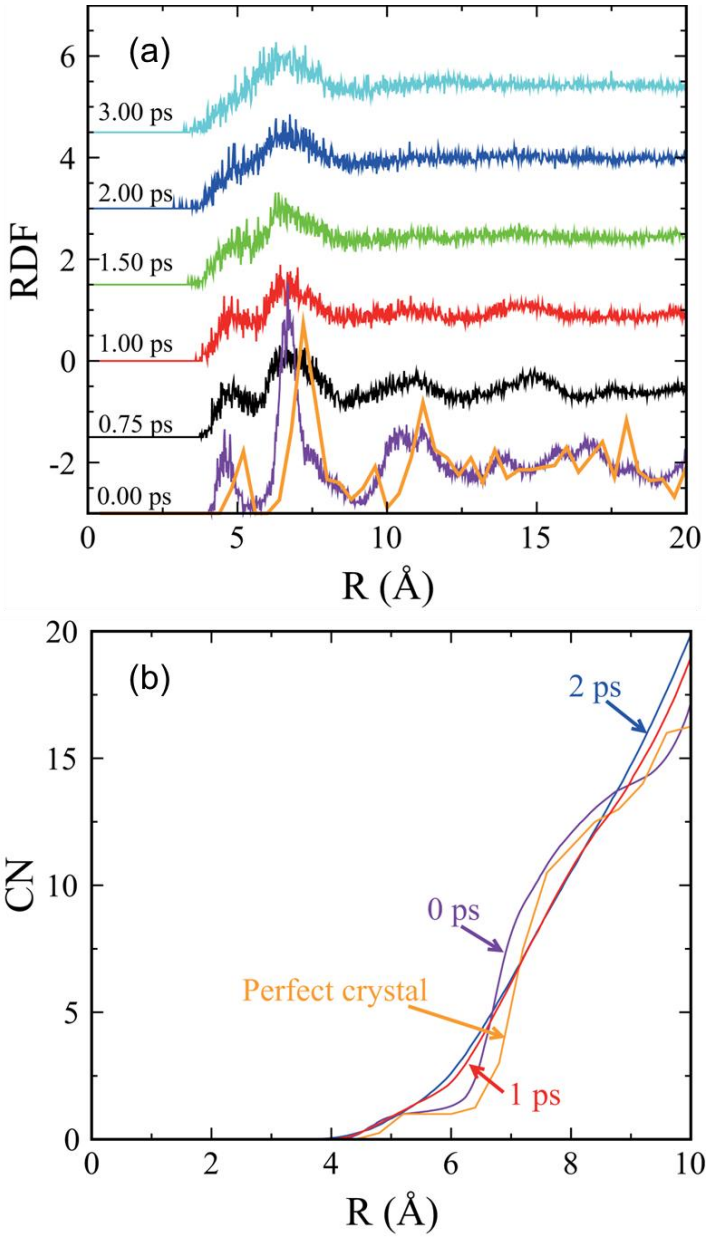

Figure 3.5 Structural analysis for the sensitive (100) shock and {-110}/<110> slip system (10% pre-compression). The radial distribution function (RDF) for the center of mass of each RDX molecule is shown in (a), indicating that the crystalline character is retained up to ~ 1 ps, and the integrated coordination numbers (CN) in (b) remains that of the experimental structure at room temperature (the orange line). Compared with perfect crystal, the RDF at 0 ps in (a) is shifted to the left due to the 10% pre-compression. By 2 ps the system has the amorphous structural characteristics of the liquid phase of RDX condensed systems.

After the system becomes amorphous, the shear stresses reach constant values, leading to the viscosity:

$$\tau_{xy} = \eta \gamma_{xy} \ . \tag{1}$$

Here τ_{xy} is the converged shear stress (GPa) for the RDX amorphous, γ_{xy} is the shear rate 0.5 ps^{-1}, and η is viscosity in the unit of poise. We calculate a viscosity of 2.1 centipoise for 10% compression (5 GPa for pressure when shear stress converged) and 3.6 centipoise for 20% compression (11 GPa for pressure when shear stress converged).

For 20% pre-compression, we chose 24 slip systems for CS-RD simulations of the five shock directions (See Table 3.7 to Table 3.11 for more details). Under 20% pre-compression, we selected the same slip systems based on the shear stress barrier over the initial shear stress as the possible activated slip system for the five shock directions except for the (100) shock. Based on the strain energy density, shear-stress overshoot, temperature rise, stress barrier, and NO_2 production, we found that (100) and (210) shocks are still most sensitive, while (111), (120), and (110) are insensitive shock directions.

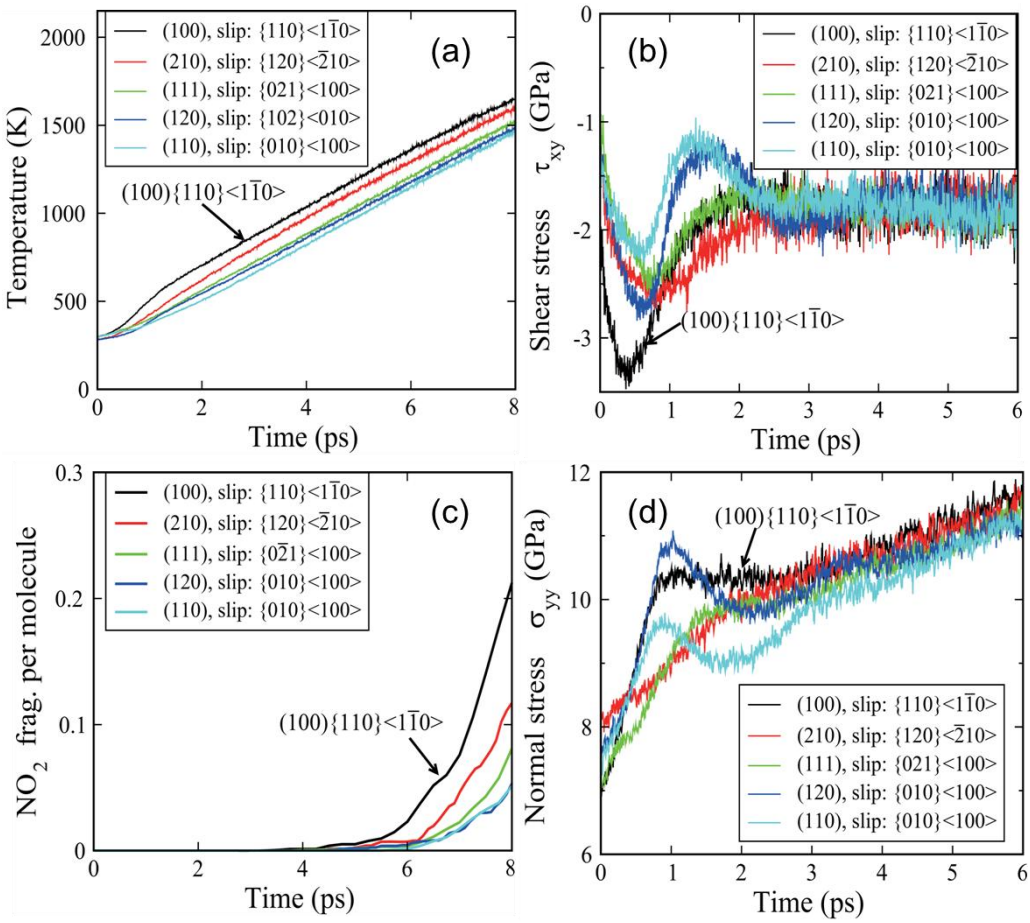

Figure 3.6 CS-RD results for the preferred slip system predicted for each of the 5 shock directions (after 20% pre-compression). (a) Temperature, (b) shear stress, (c) NO_2 products, and (d) normal stress as a function of time under various shock directions in shear simulation. These calculations identify the (210)/{120}<-210> and the (100)/{110}<1-10> shock/slip system are the two most sensitive cases. In both cases, the large shear stress overshoot in (b) for 0 to 0.5 ps results from an initial bad steric overlap. This bad steric contact causes the large normal stress observed between 0−0.5 ps in (d). The external mechanical work necessary to overcome the large stress barrier leads to the large extra temperature increase by 1 ps compared with the other slip systems shown in (a). This extra temperature remains for the rest of the simulation, leading to significantly more molecule decomposition starting at 4 ps, as shown in (c).

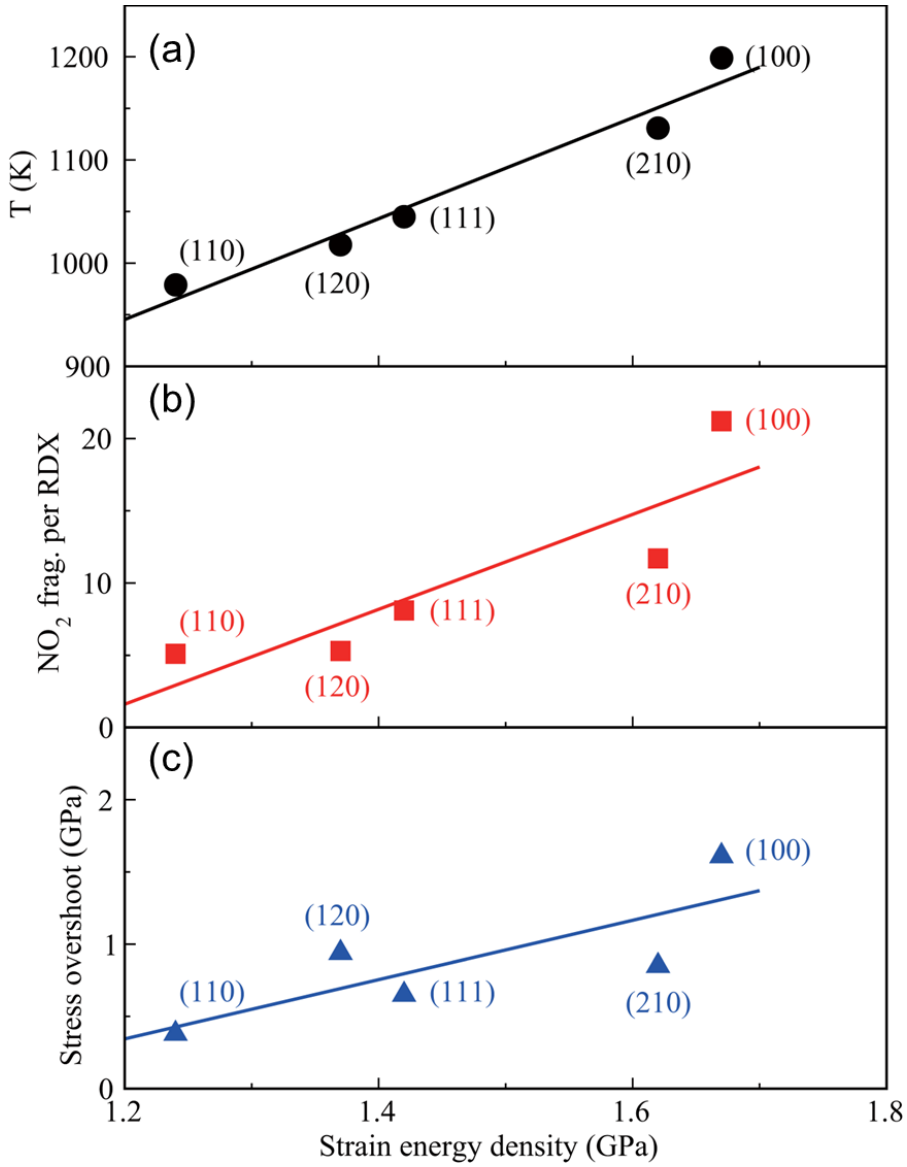

Figure 3.7 Correlations between the strain energy density (integration of shear stress up to 3.0 ps in Fig. 3.5b) and other sensitivity measurements for 20% pre-compression: (a) temperature at 5 ps, (b) NO_2 production at 8 ps, (c) stress overshoot during CS-RD. The large strain energy density for the sensitive (100) shock plane and somewhat less for the (210) plane lead to the high temperature increase, increased NO_2 production, and large stress overshoot during CS-RD.

We also performed the CS-RD simulation on 30% pre-compression for the (100), (110) and (111) shock planes. The CS-RD results are in Table 3.14 shown below. It is found that (100) is still sensitive shock plane, while (110) and (111) are insensitive shock planes. These results are consistent with 10% and 20% pre-compression.

Table 3.14 Temperatures (at 2 ps), NO_2/RDX ratio (at 4 ps), shear stress overshoot (τ_{max}-τ_c), and strain energy density W (integration of stress up to 2 ps) for 30% compression-shear simulations for three shock directions

Sensitivity	Shock plane	Slip system	T (K)	NO_2/RDX (%)	$\tau_{max} - \tau_c$ (GPa)	W (GPa)
sensitive	(100)	*{-110}<110>	1186	18.8	4.31	2.25
insensitive	(111)	*{021}<100>	806	3.85	2.23	1.98
insensitive	(110)	*{010}<100>	650	1.13	1.02	1.33

Our CS-RD results of 10% pre-compression and 20% pre-compression are consistent with the shock experiments[18], suggesting that (100) and (210) are sensitive shock directions while (111) is an insensitive shock direction at the pressures 7−20 GPa[18].

The slip system {120}/<-210> for (210) shock plane is not observed in the nanoindentation experiment[19−23], but it is suggested as the possible slip system under high compression based on our CS-RD simulation. We believe that this slip system may not be easily activated under low pressure due to the multiple shear-stress barriers shown in Fig. 2b. The high compression is necessary to increase the initial shear stress and activate this slip system.

3.4.3 Steric hindrance analysis

To understand the molecular origin of sensitivity, we now examine the relationship between sensitivity and steric hindrance estimated from initial molecular geometry. Figure

3.8 shows the steric hindrance contour maps for the (100) shock and {-110}/<110> slip system, and the (110) shock and {010}/<100> slip system. The steric hindrance contour map represents the overlapped regions and possible contact areas during shear deformation. It can be seen from the maps that the shear deformation induced by (100) shock would encounter more bad contacts than those for (110) shock. For (100) shock, the interconnected contact patterns indicates more intensive contacts and the higher overlap score represents more multiple contacts.

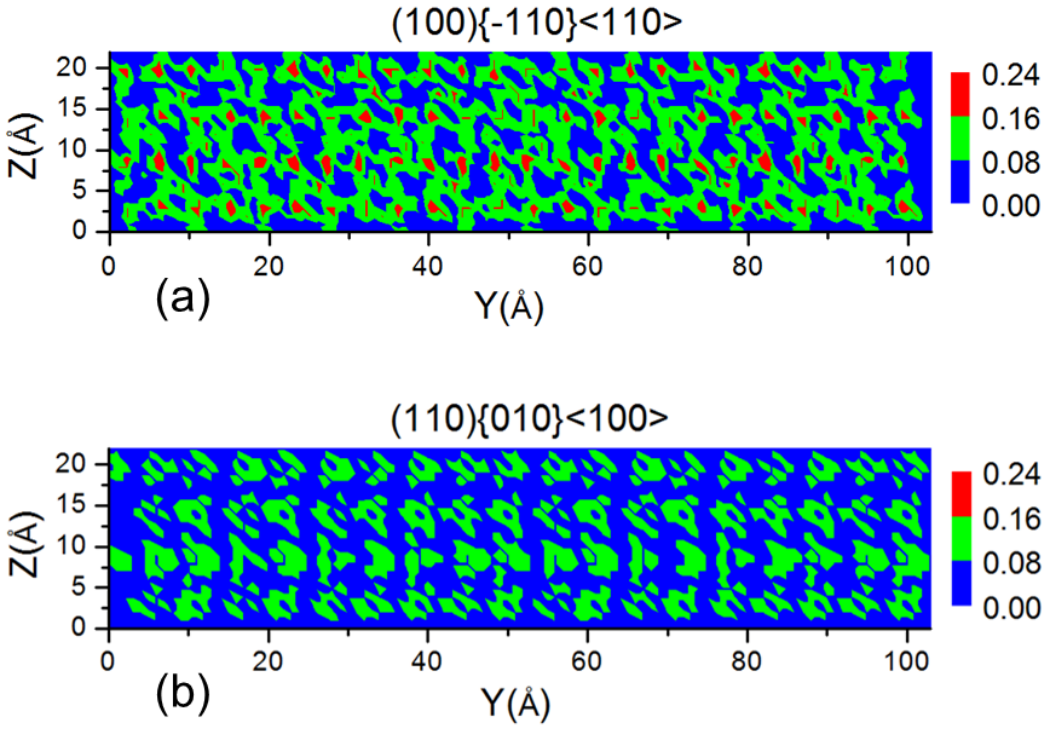

Figure 3.8 Steric hindrance counter maps projected along *x* slip direction for (a) the (100) shock with the {-110}/<110> slip system found to be most sensitive, with steric hindrance index (SHI) 0.59, and (b) (110) shock and {010}/<100> slip systems found to be least sensitive, with SHI 0.43 after 10% pre-compression. The larger contact areas/scores and interconnected contact pattern for (100) shock indicate larger molecular steric hindrance during shear deformation, which is responsible for its large sensitivity.

On the other hand, for (110) shock, the gaps between contact regions provide more rooms for geometry relaxation when molecules conflict. Indeed, the SHI of the sensitive (100) shock is 0.59, indicating 16% more overlap region than the insensitive (110) shock with SHI 0.43. Our calculations also show that SHI increases with the compression ratio. This means strong shock with large compression causes more steric hindrance than weak shock. The analyses of steric hindrance contour map and SHI support the steric hindrance explanation for anisotropic sensitivity.

3.5 Conclusions

We find that the CS-RD protocol successfully predicts that (100) and (210) are the most sensitive shock directions while (120), (111), and (110) shocks are insensitive. The predicted relative sensitivities are consistent with the previous RDX shock experiments at pressures around 7−20 GPa.

Now that the CS-RD protocol has been validated for PETN, HMX, and RDX, for which the experimental data are most complete, we can proceed now to examine new energetic systems to predict which ones would be least sensitive. Also we can consider heterogeneous systems, with defects and impurities, to determine their roles in determining sensitivity.

We should emphasize here that CS-RD is aimed toward a rapid assay of anisotropic sensitivity that can be used when considering new energetic materials. We deliberately impose rather severe conditions to involve stresses comparable to experiments but driven at high rates to examine sensitivity rapidly. The high shear rates used here already lead to continuously shearing fluid system by 10 ps and all slip systems considered here would

rapidly detonate under these conditions. However, even so, we find dramatic differences between sensitive and insensitive slip systems as reflected in strain energy density, temperature rise, and molecule decomposition.

Our reactive dynamics studies for PETN, HMX, and RDX support the concept that molecular steric hindrance contributes to the origin of anisotropic sensitivity of energetic materials. Molecular steric hindrance is thus critical to the development of energetic materials with reduced sensitivity.

3.6 References

[1] J. J. Dick, Effect of crystal orientation on shock initiation sensitivity of pentaerythritol tetranitrate explosive, *Appl. Phys. Lett.*, 44, 859, 1984.

[2] J. J. Dick and J. P. Ritchie, Molecular mechanics modeling of shear and the crystal orientation dependence of the elastic precursor shock strength in pentaerythritol tetranitrate, *J. Appl. Phys.*, 76, 2726, 1994.

[3] J. J. Dick, R. N. Mulford, W. J. Spencer, D. R. Pettit, E. Garcia, and D. C. Shaw, Shock response of pentaerythritol tetranitrate single crystals, *J. Appl. Phys.*, 70, 3572, 1991.

[4] C. S. Yoo, N. C. Holmes, P. C. Souers, C. J. Wu, F. H. Ree, and J. J. Dick, Anisotropic shock sensitivity and detonation temperature of pentaerythritol tetranitrate single crystal, *J. Appl. Phys.*, 88, 70, 2000.

[5] S. V. Zybin, W. A. Goddard, P. Xu, A. C. T. van Duin, and A. P. Thompson, Physical mechanism of anisotropic sensitivity in pentaerythritol tetranitrate from compressive-shear reaction dynamics simulations, *Appl. Phys. Lett.*, 96, 081918, 2010.

[6] T. Zhou, S. V. Zybin, Y. Liu, F. Huang, and W. A. Goddard, Anisotropic shock sensitivity for β-HMX energetic material under compressive-shear loading from ReaxFF -lg reactive dynamics simulations, *J. App. Phys.*, 2012 (in review).

[7] A. C. T. van Duin, S. Dasgupta, F. Lorant, and W. A. Goddard, A Reactive Force Field for Hydrocarbons, *J. Phys. Chem. A.*, 105, 9396−9409, 2001.

[8] R. W. Armstrong, Dislocation-assisted initiation of energetic materials, *Cent. Eur. J. Energetic Mater.*, 2, 55, 2005.

[9] S. M. Walley, J. E. Field, and M. W. Greenaway, Crystal sensitivities of energetic materials, *Mater. Sci. Tech.*, 22, 402−413, 2006.

[10] K. Ramos, D. Hooks, and D. Bahr, Direct Observation of Plasticity and Quantitative Hardness Measurements in Single Crystal Cyclotrimethylene Trinitramine by Nanoindentation, *Phil. Mag.*, 89(27), 2381−2402, 2009.

[11] W. Connick and F. G. J. May, Dislocation etching of cyclotrimethylene trinitramine crystals, *J. Cryst. Growth*, 5, 65−69, 1969.

[12] W. L. Elban, J. C. Hoffsommer, and R. W. Armstrong, X-ray orientation and hardness experiments on RDX explosive crystals, *J. Mater. Sci.*, 19, 552−566, 1984.

[13] P. J. Halfpenny, K. J. Roberts, and J. N. Sherwood, Dislocations in energetic materials, *J. Mater. Sci.*, 19, 1629−1637, 1984.

[14] W. L. Elban, R. W. Armstrong, K. C. Yoo, R. G. Rosemeier, and R. Y. Yee, X-ray reflection topographic study of growth defect and microindentation strain fields in an RDX explosive crystal, *J. Mater. Sci.*, 24, 1273−1280, 1989.

[15] H. G. Gallagher, P. J. Halfpenny, J. C. Miller, and J. N. Sherwood, Dislocation Slip Systems in Pentaerythritol Tetranitrate (PETN) and Cyclotrimethylene Trinitramine (RDX), *Phil. Trans. Roy. Soc. Lond. A*, 339, 293−303, 1992.

[16] I. T. Mcdermott and P. P. Phakey, A method of correlating dislocations and etch pits: application to cyclotrimethylene trinitramine, *J. Appl. Crystallogr.*, 4, 479−481, 1971.

[17] D. E. Hooks, K. J. Ramos, and A. R. Martinez, Elastic-plastic shock wave profiles in oriented single crystals of cyclotrimethylene trinitramine (RDX) at 2.25 GPa, *J. Appl. Phys.*, 100, 024908, 2006.

[18] N. C. Dang, Z. A. Dreger, Y. M. Gupta, and D. E. Hooks, Time-resolved spectroscopic measurements of shock-wave induced decomposition in cyclotrimethylene trinitramine (RDX) crystals: anisotropic response, *J. Phys. Chem. A*, 114, 11560−11566, 2010.

[19] C. S. Choi and E. Prince, The crystal structure of cyclotrimethylenetrinitramine, *Acta Cryst.*, B28, 2857−2862, 1972.

[20] R. J. Karpowicz, T. B. Brill, Comparison of the molecular structure of hexahydro-1,3,5-trinitro-s-triazine in the vapor, solution and solid phases, *J. Phys. Chem.*, 88, 348−352, 1984.

[21] W. C. McCrone, Crystallographic Data. 32. RDX(Cyclotrimethylenetrinitramine), *Anal. Chem.*, 22, 954−955, 1950.

[22] B, J. Baer, J. Oxley, and M. Nicol, The phase diagram of rdx (hexahydro-1,3,5-trinitro-s-triazine) under hydrostatic pressure, *High Pressure Res.*, 2, 99−108, 1990.

[23] Z. A. Dreger, and Y. M. Gupta, High pressure Raman spectroscopy of single crystals of hexahydro-1,3,5-trinitro-1,3,5-triazine (RDX), *J. Phys. Chem. B*, 111, 3893−3903, 2007.

[24] T.B. Brill, T. Sergio, and R. Karpowicz, A Fourier transform infrared spectroscopy study of an energetic material, *Ind. Eng. Chem. Prod. Res. DeV.*, 22, 363−365, 1983.

[25] P. Torres, I. Cotte, S.P. Hernandez, N. Mina, A. Santana, R. Chamberlain, R. Lareau, and M. Castro, Vibrational Spectroscopy Study of β and α RDX Deposits, *J. Phys. Chem. B*, 108, 8799−8805, 2004.

[26] M. J. Cawkwell, K. J. Ramos, D. E. Hooks, and T. D. Sewell, Homogeneous dislocation nucleation in cyclotrimethylene trinitramine under shock loading, *J. Appl. Phys.*, 107, 063512, 2010.

[27] I. Plaskin, C. S. Coffey, R. Mendes, J. Ribeiro, *J. Campos, and J. Direito, 13th Symposium International on Detonation*, ONR 351-07-01, p. 319, 2006.

Chapter 4 Elucidation of the dynamics for hotspot initiation at nonuniform interfaces of highly shocked materials

4.1 Overview

The fundamental processes in shock-induced instabilities of materials remain obscure, particularly for the detonation of energetic materials. We simulated these processes at the atomic scale on a realistic model of a polymer-bonded explosive (3.7 million atoms/cell) and observed that a hot spot forms at the nonuniform interface, arising from shear relaxation that results in shear along the interface that leads to a dramatic temperature increase that persists long after the shock front has passed the interface. For energetic materials this temperature increase is coupled to chemical reactions that lead to detonation. We show that decreasing the density of the binder eliminates the hot spot.

The interaction of shock waves with non-uniform interfaces plays essential roles in the interfacial instabilities in inertial confinement fusion (ICF), in shock-induced Richtmyer-Meshkov (RMI) instabilities, and in detonation in heterogeneous polymer-bonded explosives (PBXs). For detonation, it is generally accepted that hot spots form during the development of instabilities as shock waves pass through the interface or other defects[1−4]. Despite numerous experimental and theoretical studies the fundamental processes involved remain controversial. This is due to the complex environment and coupling of thermal, chemical, and mechanical degree of freedom, which is extremely difficult to unravel experimentally. It has also been most difficult to theoretically to include the reactive processes involved and yet cover the enormous size and time scales intrinsic to the phenomena.

4.2 Significance of modeling hotspot formation on realistic PBX

To discover the origin of shock-induced hotspot formation, we carried out reactive dynamics (RD) using the ReaxFF reactive force field on a realistic model of a real polymer-bonded explosive, PBX N-106. Energetic materials (EM) are essential for applications ranging from rocket engines, to building and dam construction, to armaments. Generally the EM is bound together in a matrix of polymer elastomers to form the PBX that can be molded to various shapes, while providing some control in resisting unintentional detonation due to shocks or friction. Unfortunately, current generations of PBX are sensitive to accidental detonation, despite many attempts to control the safety by improvements in materials and manufacturing practices. Here we use the ReaxFF reactive force field to examine the effect of shocks on realistic models of polymer-bonded explosives, where we use these simulations to extract the mechanism of hot-spot formation. Then, based on this model, we predict how to change the system to reduce the hot spot, and carry out simulations to validate this prediction.

ReaxFF has now been established to provide nearly the accuracy of quantum calculation in the various reaction barriers and rates, while providing a computational efficiency nearly that of ordinary molecular dynamics (MD) with ordinary force fields (FF), enabling us to study the complex processes involved in interfacial instabilities at the atomic scale, providing insights on such phenomenon. Thus ReaxFF provides the possibility of realistic simulations to probe the atomistic mechanism controlling detonation[5−12] and leads to an accurate description of the complex chemistry of RDX

under shock-loading conditions[6]; and similar calculations on polyethylene (PE) and poly (4-methyl-1-pentene) polymer lead to good agreement with the experimental Hugoniot[9].

It is generally accepted that detonation of PBXs is initiated at hot spots, but the mechanism responsible for hot-spot ignition is not clear[13]. Previous simulations[14–17] in relatively small molecular crystals and atomic-crystal-containing voids postulated that void collapse and nano-jets in voids are the source of hot-spot formation.

4.3 Simulation models of PBX

In order to develop an atomic-scale understanding of the nature of hot-spot formation of PBX materials, we used ReaxFF RD simulations to examine the effect of shocks on the materials configuration in Fig. 4.1, which involves a sawtooth interface between the RDX and the polymer (Hydroxyl terminated polybutadiene, HTPB). This system is 54 nm thick in the shock direction (x) with a period of 27 nm along the sawtooth direction (y) and is uniform with a periodic length of 25 nm in the z direction, leading to a simulation cell with 3, 695, 375 independent atoms. For shock velocities of 2.5 and 3.5 km/sec it takes ~ 10 ps for the shock wave to traverse the interface. Such a simulation cell and time interval is far beyond the capabilities of current QM methods but can be treated using the QM-based ReaxFF reactive force field.

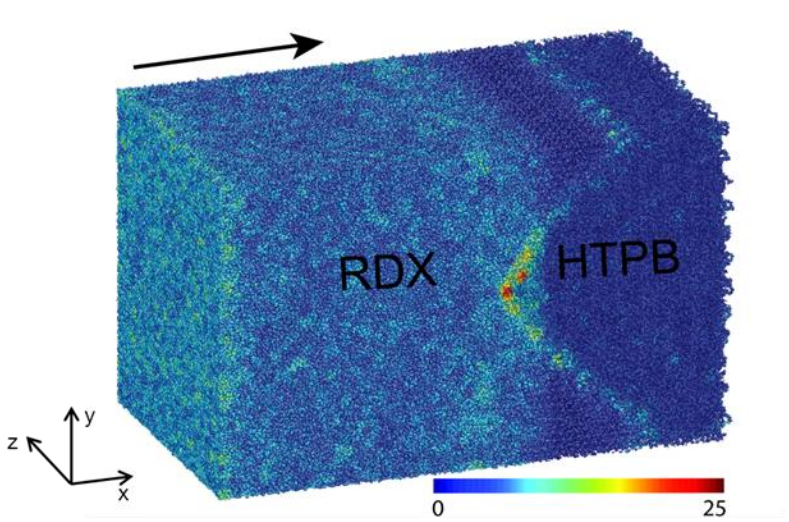

Figure 4.1 Snapshot of PBXs during shock loaded at Up = 2.5 km/s (for 6.0 ps). The shading is based on the total slip in Angstroms. This system is 54 nm thick in the shock direction (x) with a period of 27 nm along the sawtooth direction (y), and is uniform with a periodic length of 25 nm in the z direction. Arrow indicates shock direction.

Our simulations model the PBXN-106 material, which consists of cyclotrimethylene trinitramine (RDX) crystals bound together using hydroxyl-terminated polybutadiene (HTPB) and isophorone-diisocyanate (IPDI)-based polyurethane rubber. HTPB is a copolymer, containing 80% trans and cis butadiene monomers with 20% 1,2-vinyl monomers, with the chains terminated by hydroxyl groups. One HTPB monomer is shown in Fig. 4.2. Our MD simulations use 100% trans monomers, leading to a molecular weight of 1518 Daltons per chain. A plasticizer agent di-octyl adipate (DOA) is added (40% by weight) to the binder to improve casting properties. To determine the conformational state of the polymer at 300 K and 1 atm pressure, we used the CED Monte Carlo method[18, 19] designed to predict accurate cohesive energy densities of polymers. (CED combines repeated cycles of temperature annealing and quenching simultaneously with density

annealing and quenching to ensure that polymer chains are fully equilibrated). We used CED to build 10 independent samples of each polymer within a unit cell containing two independent molecular chains and 8 DOA molecules. We chose the mass ratio of binder over DOA to be 1.03, which leads to the optimum viscosity and compression strength[20]. Each chain contains 10 HTPB repeat units connected via 1 IPDI crosslinking molecule to 4 terminal HTPB repeat units per end. The initial conformation was based on rotational isomeric states (RIS) statistics, to determine the dihedral angle values for each chain and its repeating units. The torsional barriers for the RIS and the charges (Mulliken) were determined (from B3LYP hybrid density functional calculations using the 6-311 G^{**} basis set) on polybutadiene trimer. The same level of QM calculations was also performed on the IPDI and DOA to determine the charges and structures for the binder model. These QM results and are provided below from Fig. 4.2 to Fig. 4.4 and in Table 4.1.

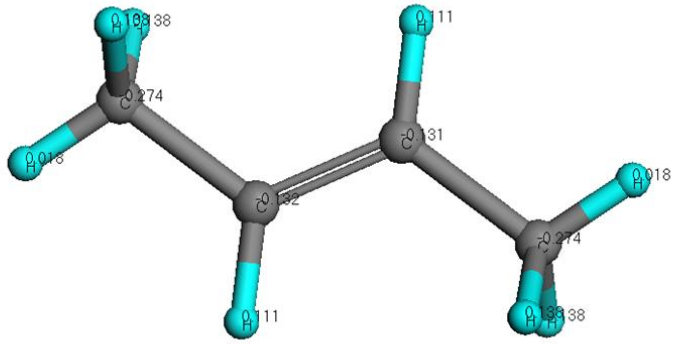

Figure 4.2 QM charge and geometry of HTPB monomer

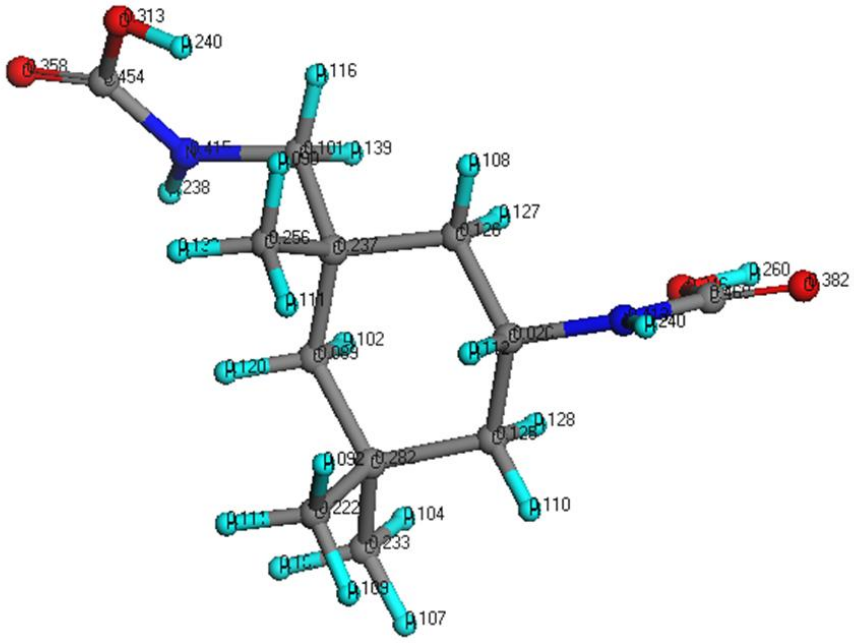

Figure 4.3 QM charge and geometry of IPDI molecular

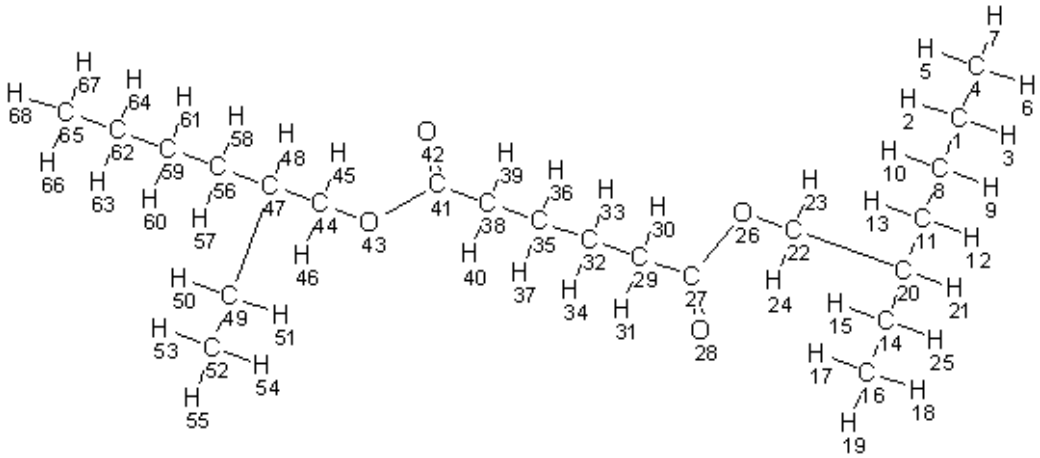

Figure 4.4 Geometry of DOA molecular

Table 4.1 QM charge of DOA molecular

C1	H2	H3	C4	H5	H6	H7	C8	H9	H10
-0.2242	0.1052	0.1044	-0.2888	0.102	0.1024	0.107	-0.1996	0.1102	0.1019
C11	H12	H13	C14	H15	C16	H17	H18	H19	C20
-0.2024	0.1055	0.1088	-0.2161	0.1233	-0.2975	0.1064	0.1102	0.1038	-0.2106
H21	C22	H23	H24	H25	O26	C27	O28	C29	H30
0.119	0.0357	0.1189	0.1223	0.1109	-0.3451	0.3768	-0.3464	-0.2515	0.1378
H31	C32	H33	H34	C35	H36	H37	C38	H39	H40
0.1389	-0.2024	0.1189	0.1145	-0.2022	0.1157	0.1177	-0.2521	0.1388	0.1384
C41	O42	O43	C44	H45	H46	C47	H48	C49	H50
0.3808	-0.3468	-0.3447	0.0096	0.1288	0.1278	-0.2176	0.1143	-0.2055	0.1071
H51	C52	H53	H54	H55	C56	H57	H58	C59	H60
0.1186	-0.2944	0.1086	0.1014	0.1092	-0.1812	0.1167	0.1032	-0.2072	0.0989
H61	C62	H63	H64	C65	H66	H67	H68		
0.1093	-0.2241	0.1046	0.1045	-0.2889	0.1063	0.1018	0.1026		

For each of the 10 samples generated in CED procedure, the equilibrium unit cell volumes and densities were optimized through a series of compression/expansion and heating/cooling cycles using conventional MD with the non-reactive Dreiding force field[21] (to prevent bond breaking). The initial polymer molecular structure was built using the RIS statistics, in a cubic simulation cell, at a target density of 50% of the expected density, ρ_{exp} (assumed to be 0.90 g/cc for HTPB). A sequence of 5 compression/expansion cycles was performed, taking the system to a final density of 1.2ρexp. Each compression/expansion cycle is consisted of 500 steps of structure minimization, with fixed cell parameters, constant-rate isotropic cell deformations and 0.5 ps of NVT MD annealing up to a temperature of 700 K. The resulting structure was then optimized for an additional 500 steps and equilibrated using NPT MD for 10 ps at 298 K. Finally, a binder model was prepared (lattice parameter a = 21.674 Å, b = 22.337 Å, c = 21.9210 Å, α = 90.536, β =

89.840, γ = 90.581). Including the cross linker and plasticizer molecules in the final structure led to an optimum density of 0.94 g/cc, slightly larger than that of pure HTPB. Using ReaxFF, we optimized the RDX and polymer binder, leading to lattice parameters of a = 13.684 Å, b = 12.307 Å, and c = 11.563 Å for RDX at room temperature, in agreement with experimental values (13.182 Å, 11.574 Å, and 10.709 Å, respectively)[22]. For the binder system, the CED procedure led to a final density of 0.95 g/cc, after performing structure minimization and 25 ps NPT-MD at room temperature. We then combined a 32x22x22 RDX supercell of RDX with a 13x11x11 (2% compressed) binder supercell to produce the PBX model. Two separate complementary surfaces were built to form a triangular interface between the two materials, as shown in Fig. 4.1, and then relaxed using 4ps NVT-MD.

To simulate the propagation of shock waves in the PBX, we impacted the two-dimensionally periodic PBX slab onto a Lennard Jones 9-3 wall. The shock direction (x) was set to be finite. The slab was thermally equilibrated at T = 300 K for 4 ps and then propelled at the desired impact velocity, by adding a corresponding translational velocity on top of the thermal component. This procedure produces a shock wave with average particle velocity (U_p) equal to the impact velocity, propagating into the slab from the RDX side. Here we explore the shock response of the non-uniform interface in the PBX at U_p = 2.5, 3.5 km/s via adiabatic MD to follow the dynamic evolution of the system, using a time step of 0.1 femtosecond to integrate the equations of motion, for up to 10 ps.

Considering the heterogeneities normal to the shock direction (x), we partition the simulation cell into fine bins along the x, y directions and average all physical properties of

interest within each bin, including stress (σ_{ij}) and temperature (T) profiles in the xy plane at different stages of compression (i, j = 1, 2 and 3, corresponding to x, y, and z, respectively). The atomic stress is obtained from the atomic virial[23]. The stress calculation is based on the COM of each molecule to eliminate binning effects. The bin width is ~ 1 nm × 1 nm in the xy plane. The von Mises shear stress τ is also computed as the maximum shear stress, as $2\tau = \sigma_{xx} - (\sigma_{yy}+\sigma_{zz})/2$ under the assumption of $\sigma_{yy} = \sigma_{zz}$ which is true in our simulations.

To track the chemical processes as the shock wave propagates through the PBXs, we analyze the fragments resulting from the corresponding ReaxFF MD trajectories based on a time-windowed average of bond orders. Combining the fragment analysis results and the 2 dimensional binning analyses, we examined the chemistry in the xy plane at different stages of shock loading. To examine the atomic local shear, we use maximum relative displacement (MRD)[24,25] which is defined as $\mathbf{s_i} = \mathbf{x_{ij}} - \mathbf{X_{ij}}:|\mathbf{x_{ij}}-\mathbf{X_{ij}}|_{\mathbf{max}}$. Here the $\mathbf{x_{ij}}$ and $\mathbf{X_{ij}}$ vectors correspond to the difference between the current and reference configurations for atoms i and j (slipped neighbors of atom i), respectively. The reference configurations are taken to be the pre-shock structures.

4.4 Results and discussion

Fig. 4.6a–d shows the 2D profile of temperature T and shear stress τ at various stages of compression for Up = 2.5 km/s. The temperature at the angular tip interface region increases by around 400 K compared to other shocked regions once the shock wave has passed through, leading to the formation of a hot spot. The hot spot region expands into the explosive along the interface as the shock wave continues to propagate. The shock wave

converges as it propagates in the binder due to the wave refraction as it passes through the nonuniform interface. This shock wave convergence leads to a small, second-highest temperature region (~ 50 K higher, as shown in Fig. 4.5 below), to the right of the hotspot region in the binder. This hot spot also appeared at higher shock velocities.

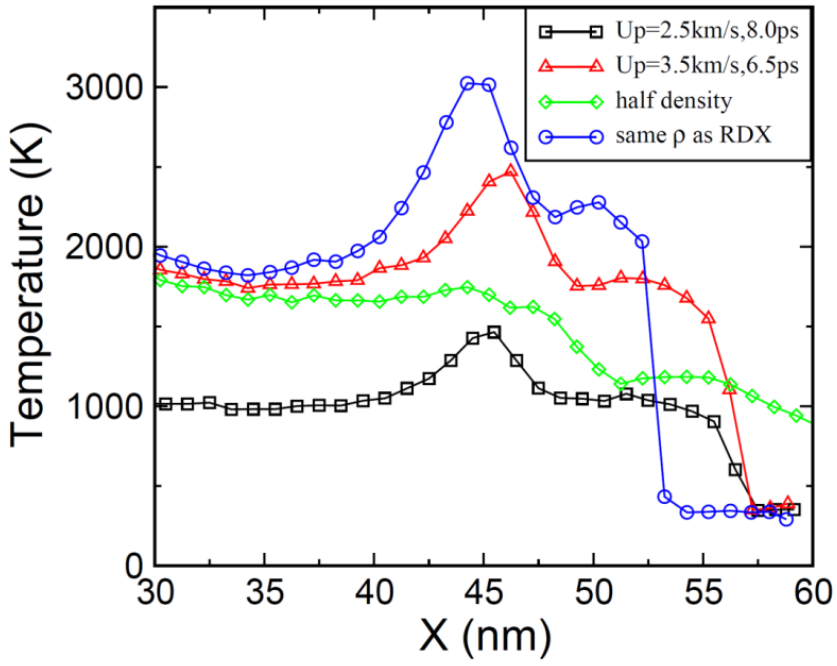

Figure 4.5 One-dimensional temperature profile of four different shocks. High-density polymer leads to much increase of temperature (blue circle). The hotspot will disappear if we reduce the density of polymer to half of its original value (green diamond). The first hotspot happened at the interface of RDX and polymer, which is about 400 K higher than the other shocked region for Up = 2.5 km/s, and 600 K higher than for Up = 3.5 km/s. The second hot spots are at the polymer region and are around 50 K higher for both cases due to the convergence of the shock wave.

To understand the mechanism underlying the hot-spot formation found in our study, we traced the von Mises shear stress at different stages. Upon shock arrival to the interface, we find reduction of shear stresses at the angular tip regions as manifested in Fig. 4.2g. This arises from rapid relaxation of the stress at the tip by the more compressible polymer,

possibly combined with the convergence of the shock wave at the tip, interfacial friction between RDX and binder, and perhaps collapse of tiny nanovoids at the angular tip. *This shear localization at the angular tip leads to nucleation of the hot-spot*. The stress decreases rapidly in the hotspot region, leading to large local shear deformations, as shown in fig. 4.2h. This small hotspot region expands rapidly as the shock wave propagates, causing additional shear localization near the interface in the explosive and an additional increase in the local temperature. Since the time scale is only ps, we consider this to be an adiabatic shear localization process. The expansion in the shear-localized region is depicted in Fig. 4.2 g–h. The MRD analysis in Fig. 4.1 shows that the regions with maximum local deformation correspond to the maximum local shear stress relaxation, and to the hot spot. Since the shock wave propagates from high density (RDX) explosives to low-density (binder) polymeric matrix, the reflective waves from the interface will decrease the stress in the explosive, which tends to suppress hot-spot formation, as discussed below. Thus we find that the hot-spot forms in our system as a compromise between shear localization and reflective wave relaxation in the angular tip and interface regions. Our atomically based hot spot ignition mechanism provides an understanding that differs from previously proposed mechanisms[26] involving adiabatic compression of a trapped gas, cavity collapse including viscous or plastic heating of the surrounding matrix material, or friction between the impacting surfaces, among other phenomena.

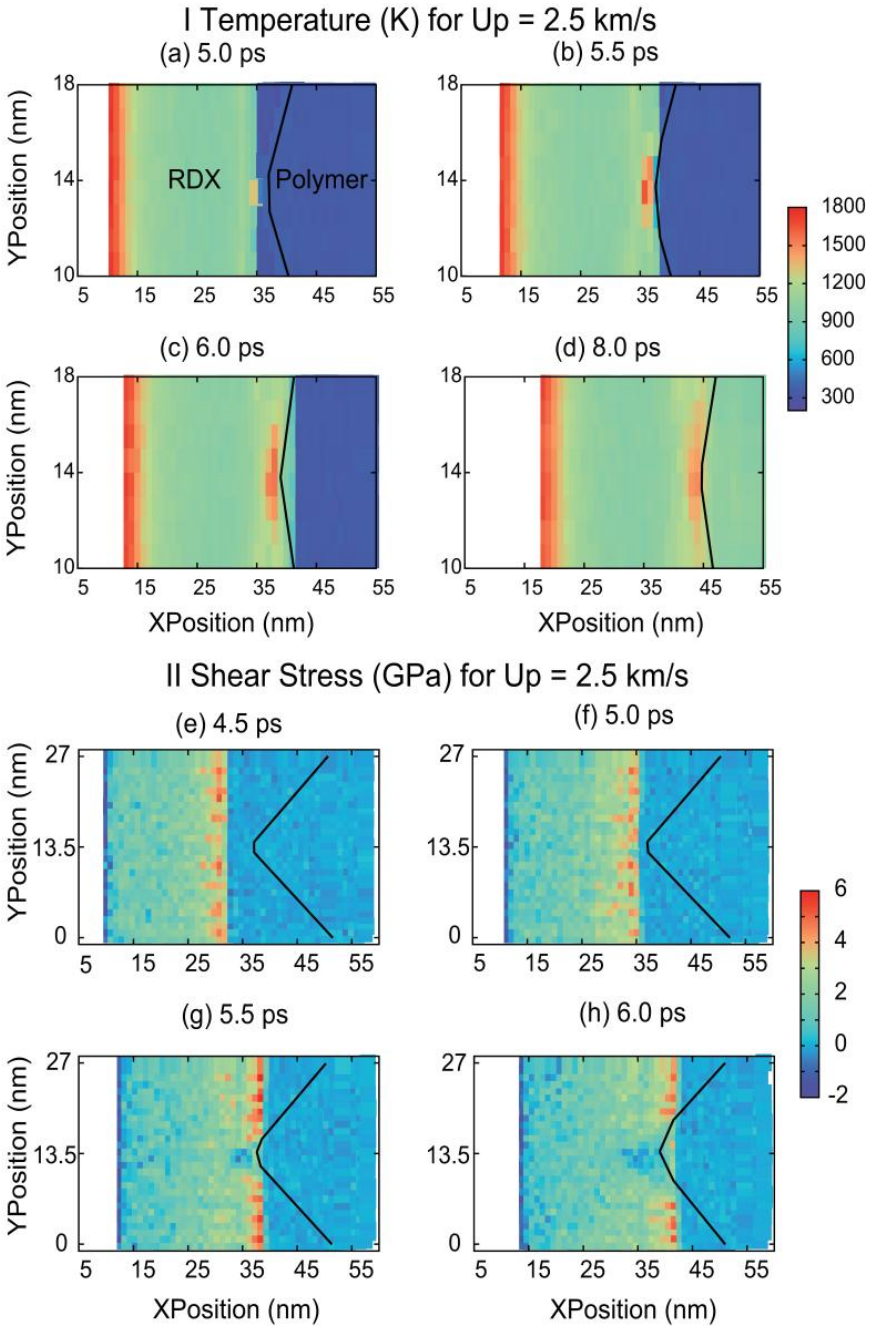

Figure 4.5 Time evolution of temperature and Von-Mises shear stress for Up = 2.5 km/s at various stages during the shock compression. The solid line represents the interface position between the RDX and the binder. Shock wave propagates from left (RDX) to right (binder). (e) 4.5 ps, shock wave has not propagated to polymer; (a,f) 5.0 ps, shock wave just reaches the interface; (b,g) 5.5 ps, adiabatic shear localization in a small triangle interface region; (c,h) 6.0 ps, shock wave has passed through the hot-spot region; (d) 8.0 ps, shock wave has passed through the interface

In order to follow the chemical processes as the shock wave propagates through the interface of the RDX and the binder, we plot the distribution of NO_2 production in the xy plane, since NO_2 dissociation is the main chemical product for U_p below 4 km/s (see previous study, Ref. [6]). Fig. 4.7 shows the time evolution of NO_2 for Up = 2.5 km/s and 3.5 km/s. We find few reactions for Up = 2.5 km/s, except those happening in the hot-spot region. The plastic shear deformation in the hot spot region produces enough energy for N−N bond excitations, leading to increased NO_2 formation. The same phenomenon occurs for Up = 3.5 km/s. The chemical reactions occurring in the hot spot region release additional energy, expanding it to induce even more shear deformation. Under the coupling effects of local shear relaxation, increased chemical reactions, increased local temperature, and the reflective wave relaxation, the hot spot expands until detonation (or at lower-input shock velocity it can disappear).

Our hot-spot ignition mechanism suggests that use of a binder with lower density would lead to decreased hot-spot formation and hence a less-sensitive EM for propulsion and explosives applications. To test this idea we changed the binder density to half the original value (0.95 g/cc), to ~ twice the value by scaling the atomic mass. We carried out shock simulations at U_p = 3.5 km/s. To analyze the hot-spot behavior we display a 2 nm segment in the y direction for a 1-dimensional binning analysis during shock compression. Fig. 4.8 shows the temperature-time and shear-stress-time diagrams from 3.6 ps, at which the shock wave has not reached the interface region. The temperature-time diagram shows that the hot-spot is dramatically increased for the high-density binder, but it disappears for

the half-density case (0.48 g/cm3). Indeed this low-density binder suppressed hot-spot formation due to the relaxation of the hot-spot.

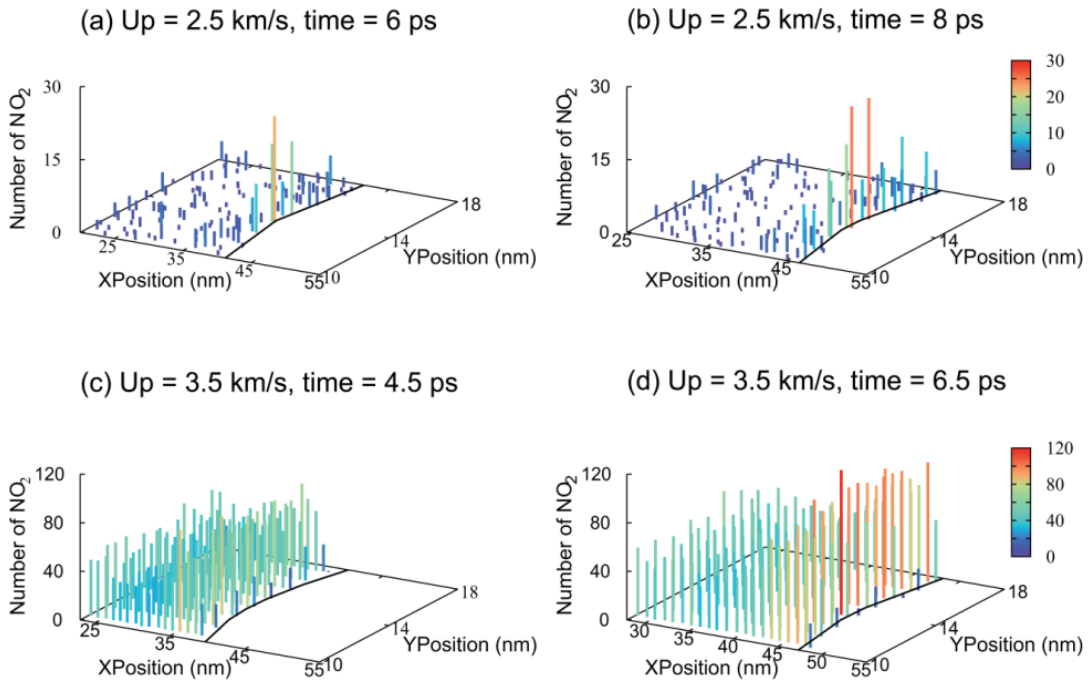

Figure 4.7 2D distribution and time evolution of chemistry (NO_2 formation) for various U_p. (a) Up = 2.5 km/s at t = 6.0 ps, chemical reaction has occurred mainly in the hot-spot region; (b) Up = 2.5 km/s at t = 8.0 ps, additional chemical reactions have occurred and a small amount of NO_2 has diffused to the polymer region (the right region of solid line in xy plane); (c) Up = 3.5 km/s at t = 4.5 ps, chemical reaction occurs in the shocked regions but many more occur in the hot-spot region; (d) Up = 3.5 km/s at t = 6.5 ps, we see diffusion of NO_2 into the polymer region.

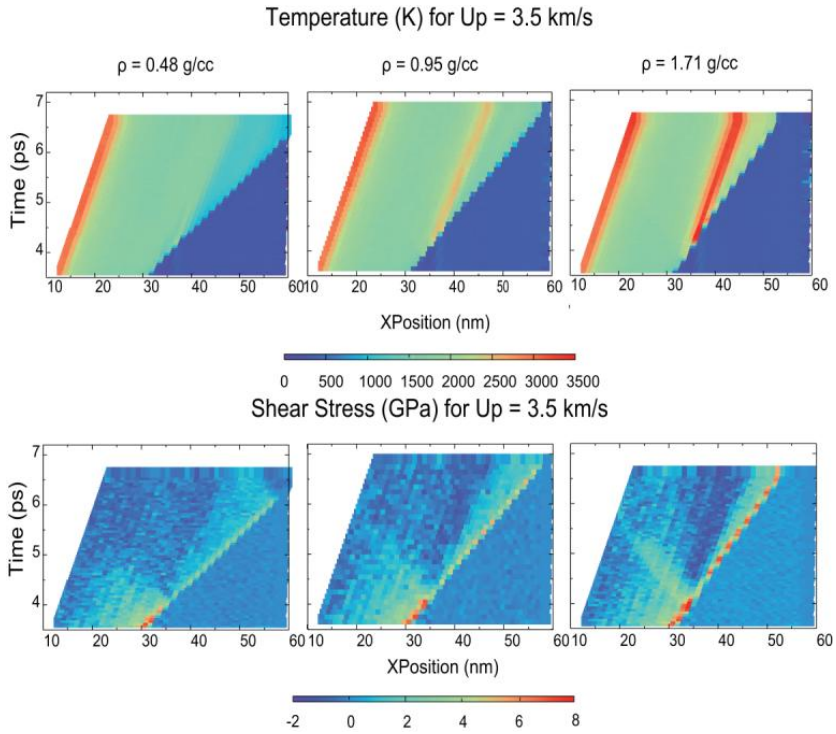

Figire 4.8 The dependence of hot-spot formation (temperature and shear stress) on the density of the polymer binder at shock velocity 3.5 km/s. The middle (0.95 g/cc) is normal density. Thus, using a polymer with ½ the normal density prevents hot-spot formation. This is due to the improved interface impedance which allows reflective rarefaction wave relaxation. In contrast, increasing binder density enhances the hot-spot due to the reflective shock waves reflected back into the RDX.

Previous studies[27,28] showed that a second shock wave (double shock) or a rarefaction wave will be reflected back into the original medium as the shock wave travels through the interface. These refraction wave patterns are determined by the shock impedance, which is the function of the incident wave angle, sound speed at shocked materials, and the pressures in two regions. As shown in the normal stress-time behavior (σ_{11}-t, Fig. 4.9), a high-density polymer matrix leads to a reflected shock wave due to the higher shock impedance at the interface, while the low-density polymer matrix leads to a rarefaction wave. The Von-Mises shear-stresses diagram in Fig. 4.8 shows the same character: a high-

shear-stressed reflective wave forms for the high-density case a modest one for normal density, and not at allfor low density (here the reflective wave relaxes the system, avoiding the hot-spot). These results indicate that the hot-spot arises from the complex variation of shock impedance at this nonuniform interface. We also note from the x-t diagram that the shock wave propagates at a slower speed through high-density binder matrix.

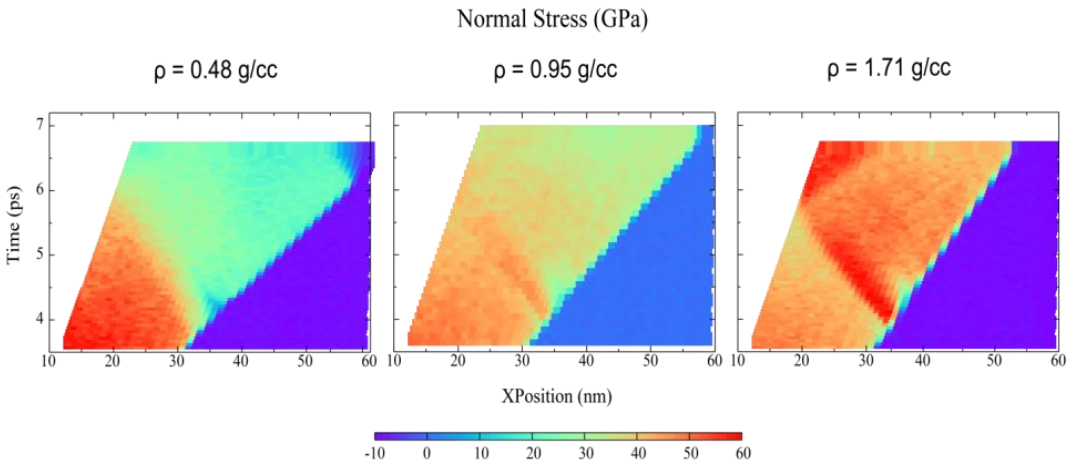

Figure 4.9 The x-t diagram for PBX with different binder densities. Color coding is based on normal stress σ_{11}.

These results suggest that a critical design strategy for developing insensitive EM for propulsion and explosives is to use binder with significantly lower mechanical impedance than that of EM. Thus merely reducing the density of the polymer by a factor of two eliminates the hot spot.

4.5 Conclusion

Summarizing, we used reactive dynamics (RD) to examine the mechanical, chemical and thermal response of mechanically shocked polymer-bonded explosive (PBX) using a realistic model of a nonuniform interface with 3,695,375 independent atoms. We observed

that a hot spot develops at the first point at which the shock wave encounters the lower-density polymer at the non-uniform interface between the explosive and elastomer. Our analysis shows that the hot spot arises from adiabatic shear localization, which leads to a dramatic temperature increase that persists long after the shock front has passed the interface, followed, for energetic materials, by coupling to chemical reactions (NO2 and HONO dissociation) that ultimately lead to detonation.

We should emphasize the sequence of events here:

- Shock at the asperity of a non-uniform interface of heterogeneous materials leads to shear relaxation that causes shear stresses along the non-uniform interface.
- These shear-stresses relaxations result in energy deposition at the interface that leads to a local significant increase in temperature.
- This increase in temperature leads to bond breaking in energetic materials that leads eventually to detonation (which may be premature).

For non-energetic materials we also expect the first two phenomena (local shear stress and temperature increase). Thus for non-energetic materials we can expect that the hot spot may cause local melting and defect generation that would accelerate failure and perhaps instabilities (e.g. Richtmyer-Meshkov).

These results suggest that a critical design strategy in developing insensitive EM for propulsion and explosives is to use a binder with much lower density, 1/3 that of the explosive. We tested this by modifying the polymer system to have half the normal density (1/3 that of the explosive) and showed that no hot spot develops using the same shock conditions.

4.6 References

[1] J. P. Dear, J. E. Field, and A. J. Walton, Gas compression and jet formation in cavities collapsed by a shock wave, *Nature (London)*, 332, 505-508, 1988.

[2] R. Chéret, *Detonation of Condensed Explosives*, Springer-Verlag, New York, 1993.

[3] F. P. Bowden and A. D. Yoffe, *Initiation and Growth of Explosions in Liquids and Solids*, Cambridge University Press, Cambridge, England, 1952.

[4] P. Maffre and M. Peyrard, Molecular-dynamics investigations of shock-induced detonations in inhomogeneous energetic crystals, *Phys. Rev. B,* 45, 9551-9561, 1992.

[5] KI. Nomura, R. K. Kalia, A. Nakano, P. Vashishta, A. C. T. van Duin, and W. A. Goddard III, Dynamic Transition in the Structure of an Energetic Crystal during Chemical Reactions at Shock Front Prior to Detonation, *Phys. Rev. Lett.*, 99, 148303 (2007).

[6] A. Strachan, A. C. T. van Duin, D. Chakraborty, S. Dasgupta, and W. A. Goddard III, Shock Waves in High-Energy Materials: The Initial Chemical Events in Nitramine RDX, *Phys. Rev. Lett.*, 91,098301, 2003.

[7] A. C. T. van Duin, S. Dasgupta, F. Lorant, and W. A. Goddard III, ReaxFF: A Reactive Force Field for Hydrocarbons, *J. Phys. Chem. A*, 105, 9396-9409, 2001.

[8] A. Strachan, E. M. Kober, A. C. T. van Duin, J. Oxgaard, and W. A. Goddard III, Thermal decomposition of RDX from reactive molecular dynamics, *J. Chem. Phys.*, 122, 054502, 2005.

[9] T. R. Mattsson, J. M. D. Lane, K. R. Cochrane, M. P. Desjarlais, A. P. Thompson, F. Pierce, and G. S. Grest, First-principles and classical molecular dynamics simulation of shocked polymers, *Phys. Rev. B*, 81, 054103, 2010.

[10] L. Z. Zhang, S. V. Zybin, A. C. T. van Duin, S. Dasgupta, W. A. Goddard III, and E. M. Kober, Carbon Cluster Formation during Thermal Decomposition of Octahydro-1,3,5,7-tetranitro-1,3,5,7-tetrazocine and 1,3,5-Triamino-2,4,6-trinitrobenzene High Explosives from ReaxFF Reactive Molecular Dynamics Simulations, *J. Phys. Chem. A*, 113, 10619−10640, 2009.

[11] N. Rom, S. V. Zybin, A. C. T. van Duin, W. A. Goddard III, Y. Zeiri, G. Katz, and R. Kosloff, Density-Dependent Liquid Nitromethane Decomposition: Molecular Dynamics Simulations Based on ReaxFF, *J. Phys. Chem. A*, 115, 10181−10202, 2011.

[12] S. V. Zybin, W. A. Goddard III, P. Xu, A. C. T. van Duin, and A. P. Thompson, Physical mechanism of anisotropic sensitivity in pentaerythritol tetranitrate from compressive-shear reaction dynamics simulations, *Appl. Phys. Lett.*, 96, 081918, 2010.

[13] J. E. Field, Hot spot ignition mechanisms for explosives, *Acc. Chem. Res.*, 25, 489−496, 1992.

[14] B. L. Holian, T. C. Germann, J. B. Maillet, and C. T. White, Atomistic Mechanism for Hot Spot Initiation, *Phys. Rev. Lett.*, 89, 285501, 2002.

[15] J. W. Mintmire, D. H. Robertson, and C. T. White, Molecular-dynamics simulations of void collapse in shocked model-molecular solids, *Phys. Rev. B*, 49, 14859−14864, 1994.

[16] K. Nomura, R. K. Kalia, A. Nakano, and P. Vashishta, Reactive nanojets: Nanostructure-enhanced chemical reactions in a defected energetic crystal, *Appl. Phys. Lett.*, 91, 183109, 2007.

[17] T. Hatano, Spatiotemporal Behavior of Void Collapse in Shocked Solids, *Phys. Rev. Lett.*, 92, 015503, 2004.

[18] I. Cozmuta, M. Blanco, and W. A. Goddard, Gas Sorption and Barrier Properties of Polymeric Membranes from Molecular Dynamics and Monte Carlo Simulations, *J. Phys. Chem. B*, 111, 3151−3166, 2007.

[19] M. Belmares, M. Blanco et al; Hildebrand and Hansen solubility parameters from Molecular Dynamics with applications to electronic nose polymer sensors, *J. Comp. Chem.*, 25,1814−1826, 2004.

[20] J. S. Gharia, R. K. Sinha, V. V. Tadas, Vinay Prakash, and V. K. Phadke, Studies on Physico-Mechanical and Explosive Characteristics of RDX/HMX-Based Castable Plastic-Bonded Explosives, *Defence Science Journal*, 48,125−130, 1998.

[21] S. L. Mayo, B. D. Olafson, and W. A. Goddard III, DREIDING: A Generic Force Field for Molecular Simulations, *J .Phys. Chem.*, 94, 8897−8909, 1990.

[22] C. S. Choi and E. Prince, The crystal structure of cyclotrimethylenetrinitramine, *Acta Cryst.*, B28, 2857−2862, 1972.

[23] J. F. Lutsko, Generalized expressions for the calculation of elastic constants by computer simulation, *J. Appl. Phys.*, 65, 2991, 1989.

[24] J. A. Zimmerman, C. L. Kelchner, P. A. Klein, J. C. Hamilton and S. M. Foiles, Surface Step Effects on Nanoindentation, *Phys. Rev. Lett*., 87, 165507, 2001.

[25] C. Brandl, *Ph.D. Thesis*, Ecole Polytechnique Fdrale deLausanne, 2009.

[26] J. E. Field, N. K. Bourne, S. J. P. Palmer, S. M. Walley, J. Sharma, and B. C. Beard, Hot-Spot Ignition Mechanisms for Explosives and Propellants, *Phil. Trans. R. Soc. Load A.*, 339, 269−283, 1992.

[27] H. Polachek and R. J. Seeger, On Shock-Wave Phenomena; Refraction of Shock Waves at a Gaseous Interface, *Rhys. Rev.*, 84 (5), 922−929, 1951.

[28] L. F. Henderson, On shock impedance, *J. Fluid Mech.*, 40 (4), 719−735, 1970.

Chapter 5 Atomistic characterization of stochastic cavitation of a binary metallic liquid under negative pressure

5.1 Overview

Cavitation, or the formation of bubbles in metastable liquids, has been investigated experimentally and theoretically since Lord Rayleigh[1–6], yet there remain considerable uncertainties in the underlying descriptions. While it has been exploited for practical uses, including ultrasonic cleaning[7,8] and sonoluminescence[9], cavitation is directly relevant to undesirable natural events including volcanic eruptions and void formation in solids or glasses that degrade their mechanical, physical, and chemical properties (e.g., fracture, shear banding, and corrosion). In particular, cavitation during isochoric cooling of a metallic liquid may lead to voids at grain-boundary triple junctions or randomly dispersed in a metallic glass. This has been difficult to characterize for most metallic glasses because they are normally multicomponent. However, bulk binary metallic glasses have recently been developed (e.g., Ni-Nb and Cu-Zr glasses), thus simplifying the analysis for elucidating the physics underlying cavitation in engineering metallic glasses and alloys.

Cavitation in a metastable liquid is a fluctuation-driven process that is described using classic nucleation theory (CNT)[10–12]. However, direct application of CNT to cavitation is complex, considering the closeness of the thermodynamic state to the spinodal, and the lack of reliable constraints on such parameters as surface tension. Molecular simulations (molecular dynamics and Monte Carlo method) and statistical theories have provided some insights into this phenomenon at a more fundamental level[13–20]. However, recent

molecular-dynamics (MD) simulations of cavitation dynamics in liquids appear to disagree with the cavitation rate from CNT, likely due to uncertainties in estimating the surface tension[13,14]. Recent studies on the fracture of Lennard-Jones liquid evaluated the pressure-dependent surface tension using the Tolman model. They estimate the CNT nucleation rate by assuming a constant surface tension leading to disagreement with CNT and MD simulations[21]. In order to connect MD simulations with transition state and nucleation theories and with experiments, we report MD simulations of cavitation in a binary metallic liquid, $Cu_{46}Zr_{54}$, under negative pressure, using a potential function (force field) derived from QM. Our studies show that cavitation can be described as a random Poisson process. Thus, using the activation volume obtained from the transition state theory and the surface energy from the Tolman length model, we find that CNT predicts the cavitation rates in accord with direct MD simulations. We characterize the pressure dependence of the activation volume within a limited range of pressure and show that the extrapolation to lower pressures leads to good agreement with experiments.

5.2 Simulation methods

Our MD simulations use the Rosato-Guillope-Legrand potential[22,23] for Cu-Zr alloy extracted from density functional theory calculations on CuZr compounds and implemented in the ITAP molecular dynamics program[24]. Previous studies[23,25,26] showed that this potential is accurate: the predicted glass formation temperature ($T_g \sim 700$ K), bulk structure, elastic moduli, and viscosity agree with available experiments.

We first construct binary $Cu_{46}Zr_{54}$ systems ranging from 2000 atoms to 54000 atoms with random atom positions. Using an integration time step of 1 fs, we melt the systems at 1200 K and equilibrate them for 100 ps for subsequent cavitation simulations. For tensile

loading, we expand the cell at a uniform expansion rate of 2×10^8 s^{-1} at 1200 K using a single Nose-Hoover thermostat (constant volume-temperature or NVT ensemble, with a Nose-Hoover time constant of 20 fs). Various time constants (10 fs to 100 fs) we tested for thermostats were found to have no effect on simulation results. The strain rate we use enables the liquid to achieve equilibrium before cavitation occurs. In order to explore the stochastic nature of cavitation, we carried out 100 independent calculations for a given initial, metastable state. In each of such runs, we changed only the initial velocity distributions (via changing the random number seed for velocity assignment) and observe the cavitation dynamics. To calculate the cavity volume within the binary liquids we use a grid-based void analysis method[27]. Given the cavity volume, we can obtain the cavity radius by assuming that the cavity has a spherical shape.

5.3 Results and discussion

Fig. 5.1a shows the pressure evolution as a function of volume (or bulk strain) for the 54,000 atom system under tension at a constant strain rate and fixed temperature (T). With increasing strain, pressure (P) decreases steadily (AB) until it reaches the pressure minimum B. AB is the liquid equation of state at fixed temperature, and pressure minimum B is expected to be close to spinodal. There is a drastic decrease in the magnitude of P after B due to tensile stress relaxation accompanying rapid cavity nucleation and growth (BC). The system then reaches a steady state (CD) where P increases slowly. Cavitation during BCD is confirmed by direct analysis, and an example of the cavity is shown as an inset to Fig. 5.1a. The cavity is approximately spherical but with a rugged surface at the MD scale.

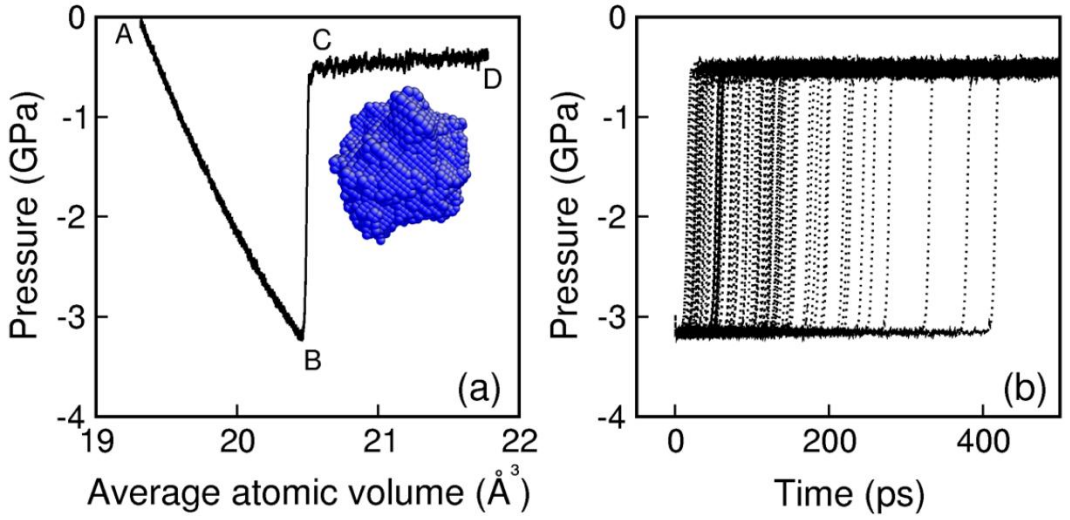

Figure 5.1 (a) Pressure-volume plot for the 54,000 atom system under hydrostatic tension at 1200 K; inset: an example of the cavity near C (~ 0.9 nm in radius). (b) Pressure evolutions for 100 independent NVT runs, all started with the same configuration at P = -3.16 GPa in (a).

In order to analyze the onset of cavitation of this metastable binary liquid, we follow its evolution under a fixed bulk volume and temperature. We choose various starting configurations from Fig. 5.1a prior to the pressure minimum B to explore homogeneous cavitation at different loading conditions. For each such configuration, we performed NVT simulations (with fixed bulk volume and temperature) and observed the cavitation dynamics under the prescribed tensile loading. The point of cavitation is obvious in the change of the instantaneous bulk pressure. Starting from a specific initial configuration (e.g., near B in Fig. 5.1a), we carried out 100 independent NVT runs; for each run, a different random number seed is used for initial velocity assignment. Fig. 5.1b shows the results from 100 runs all starting at a pre-cavitation loading of P = -3.16 GPa. For each run, P remains constant for a while and then increases rapidly as a result of cavity nucleation and growth, finally reaching a plateau in which the stress is in equilibrium (Fig. 5.1b). The

pre- and post-cavitation values of P are the same for all 100 independent runs. However, cavitation occurs at very different individual waiting times (t_{wait}). Here t_{wait} is the instant at which the pressure amplitude decreases to half of the pre-cavitation value. The exact cavitation time is the point at which the nuclei reach the critical point, which is hard to derive from direct MD simulations. Instead we define t_{wait}, which is easy to extract. This value is also reliable because the pressure drops fast over the ~ 10 ps initiating the cavitation process.

For a given pre-cavitation pressure, the statistical runs yield 100 values of t_{wait} used to construct the probability distribution (solid line in Fig. 5.2a). Here each point is broadened into a Gaussian of width 15[28]. Fitting the solid line to a Poisson process leads to the dashed line with an expected waiting time t = 97 ps. The nucleation or cavitation rate follows as $\upsilon=1/(Nt)$, where N is the system size. Here we obtain $\upsilon = 1.9 \times 10^5$ s^{-1} per atom for the 54000 atom system at pre-cavitation pressure of -3.16 GPa and temperature of 1200 K. To determine whether N = 54000 is sufficiently large for studying cavity nucleation, we performed similar simulations for N = 2000, 6750, and 16000. Fig. 5.2b shows that υ is similar for three different system sizes with N >= 6750 (~ 2×10^5 s^{-1} per atom or 10^{34} $s^{-1}m^{-3}$), indicating that cavity nucleation is a local phenomenon.

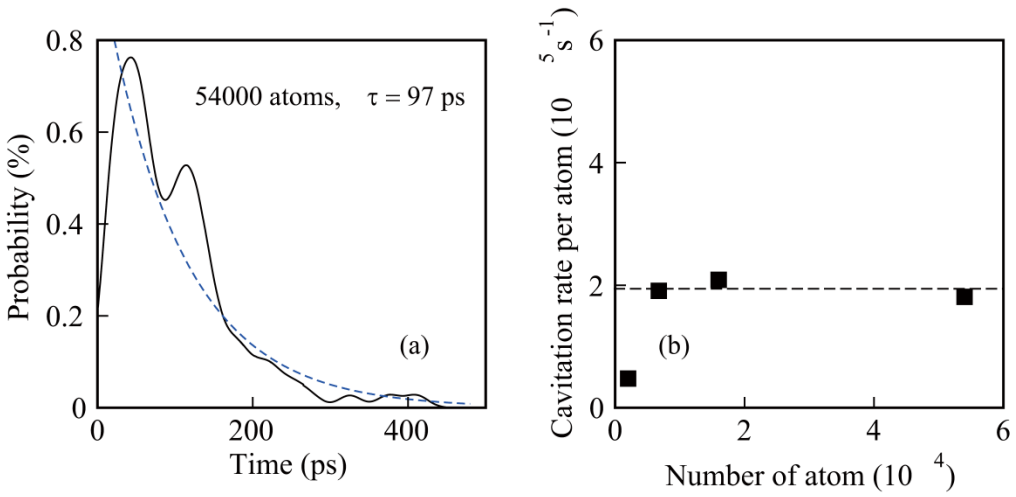

Figure 5.2 (a) Probability of cavitation obtained from 100 independent runs on the 54,000 atom system (solid line) and Poisson fitting (dashed line). T = 1200 K and P = -3.16 GPa. (b) Cavitation rates (per atom) for four different system sizes under the same loading conditions

Using transition state theory, we can write the cavitation rate as $\upsilon = \exp(-\Delta G^{\Theta}/k_B T)$, where k_B is the Boltzmann constant. The Gibbs energy of activation is $\Delta G = \Delta\Omega^{\Theta} P - \Delta S^{\Theta} T$ if we neglect the minor composition change near the cavity. The activation volume $\Delta\Omega^{\Theta} = (\frac{\partial \Delta G^{\Theta}}{\partial P})|_T$, and the activation entropy $\Delta S^{\Theta} = (\frac{\partial \Delta G^{\Theta}}{\partial T})|_P$. Our simulations are performed at a fixed temperature, so the ΔS^{Θ} term can be neglected. From transition-state theory and the definition of ν $(1/N\tau)$, we obtain

$$\Delta\Omega^{\Theta} = (\frac{\partial (k_B T ln\tau)}{\partial P})|_T . \qquad (5.1)$$

Thus, given τ for various tensile loadings, $\Delta\Omega^{\Theta}$ can be obtained as a function of P. (Similarly, the activation entropy can be obtained via varying temperature at a fixed pressure.) For the 54,000 atom system, we also performed runs at lower tensile loading to obtain longer waiting time τ. Figure 5.3 shows the plot of $k_B T\ ln\ \tau$ versus P, and its slope is the activation volume. Assuming a linear dependence of activation volume on P, we fit

the $k_B T\ ln\ \tau - P$ data points with a quadratic function. This leads to $\Delta\Omega^{\Theta} = 820.7 + 229.3$ at T = 1200 K, where pressure is in GPa and volume is in Å^3. For a precavitation pressure P = -3.16 GPa, the activation volume is 94 Å^3 at 1200 K, corresponding to about five vacancies under ambient conditions.

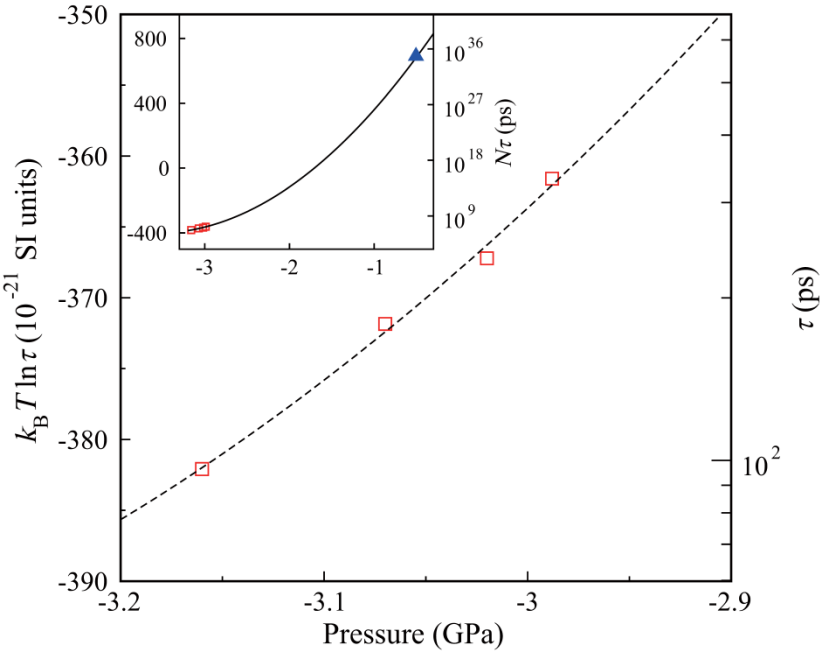

Figure 5.3 $k_B T ln\tau$ (left axis) and τ (right axis) as a function of initial pressure P for the 54 000 atom system at 1200 K. MD results: squares; dashed line: quadratic fitting. Inset: Extrapolation of MD results to experimental scales. The experiment point (triangle) has τ ≈ 7 s for a system size of 10^{22} atoms.

Cavitation nucleation experiments were carried out on $Zr_{41.2}Cu_{12.5}Ti_{13.8}Be_{22.5}Ni_{10}$ (Vitreloy 1) liquid inside fused quartz ampules of ~ 0.75 mL volume. Because the liquid has a higher coefficient of thermal expansion, we find that upon quenching below T_g the hot interior liquid cools and shrinks in volume more than the solid shell of fused silica and vitrified liquid that contains it. This results in the buildup of negative hydrostatic pressure in the liquid. Cavities formed within the quenching time scale of 7 s at an estimated temperature of ~ 1200 K and P = -0.5 GPa (triangle, inset to Fig. 5.3) (unpublished results).

To compare with the experiments, we extrapolated the fitted $k_B T\ ln\ \tau - P$ relation to lower pressures, leading to excellent agreement with the experiments (Fig. 5.3 inset). This agreement between the experiments and direct MD simulations lends support to the transition-state theory analysis. Note that the local strain rate and the cavity growth rate in our MD simulations and the loadings are different in the experiments. We find that increased precavitation tensile loading leads to higher growth rates. In Fig. 5.3, the rate effect is implicitly incorporated in the precavitation pressure.

For steady states where a cavity is in equilibrium with the surrounding liquid, the surface energy (σ) is σ = ΔP/2r, where ΔP is the pressure difference across the cavity surface and r is the radius of the cavity at steady state. We construct a cavity (radius ~ 25 Å) within the liquid at 1200 K, vary the bulk volume and let the system achieve equilibrium, and then measure the steady-state cavity size and pressure to calculate the corresponding σ. The results of σ for different cavity sizes are shown in Fig. 5.4 (squares), which can be fitted with the Tolman equation

$$\sigma(r) = \frac{\sigma_0}{1+\frac{2\delta}{r}} \qquad (5.2)$$

where the Tolman length δ = 0.3 Å and σ_0= 0.59 J m^{-2} is the surface energy for a planar surface (Fig. 5.4). We apply the Tolman equation to both steady and transient states. For P = -3.16 GPa and T = 1200 K, $\Delta\Omega^{\Theta} = 94$ Å^3 and r = 2.8 Å; the surface energy corresponding to this activation volume is σ = 0.49 J m^{-2} from the Tolman equation (triangle in Fig. 5.4).

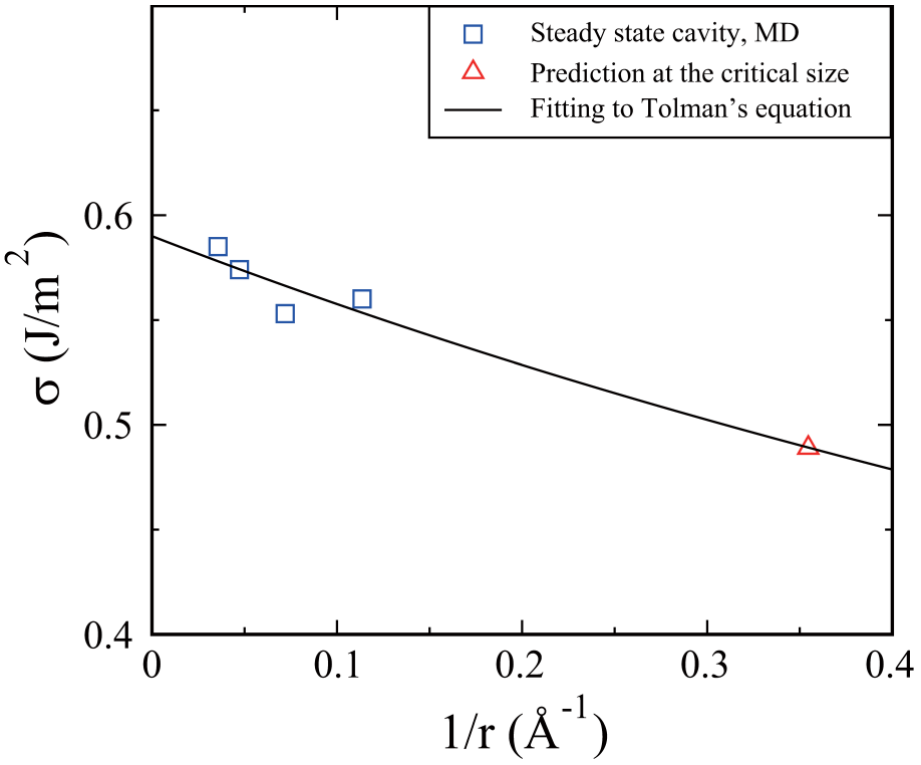

Figure 5.4 Surface energy σ versus inverse cavity size (r^{-1})

In classical nucleation theory, the driving force for cavity nucleation is $\Delta G = 4\pi r^2\sigma + 4/3\pi r^3 P$, where the first (surface) term is the free energy gain due to surface tension of a cavity and the second (volume) term is the reduction while creating the cavity. ΔG peaks at the critical value (ΔG*) with the critical radius r* = 2σ/P, and ΔG* = $16\pi\sigma^3/3P^2$. Our application of CNT assumes an ideal gas with an incompressible liquid and ignores the number of atoms in the bubble. Assuming that the activation volume at P = -3.16 GPa and T = 1200 K from transition-state theory is the corresponding critical nucleus size, we obtain a critical radius of r* = 2.8 Å for use in CNT. From our MD, we obtain σ = 0.49 J m^{-2} from the Tolman equation. This leads to ΔG* = 1.23 eV.

Given ΔG* at P = -3.16 GPa and T = 1200 K, CNT allows us to estimate the nucleation rate at the critical point: $\nu = \upsilon_0 \exp\{-\frac{\Delta G^*}{k_B T}\}$. Considering that the cavitation in vitreous liquids is related to the spontaneous and cooperative reorganization of individual clusters near the shear transformation zones (STZs), we believe that the kinetic feature of the liquid is related to the merging of α and β relaxations at high temperatures[29]. Thus, the pre-factor ν_0 is related to the Maxwell relaxation time[30], configurational entropy of critical cavity, and the size of STZs. Therefore, the pre-factor is $\nu_0 = (1/N^*)(\mu/\eta)(\exp(n\Delta S/k_B))$. Here μ is the shear modulus, η is the viscosity, μ/η is the Maxwell relaxation frequency, N^* is the number of atoms in the STZs (~ 100 atoms, as for glass[31]), ΔS is the configurational entropy per atom, and n is the number of atoms occupying the same volume as the critical cavity. From our previous MD study[26], μ = 2 GPa and η = 0.2 Pa s under similar conditions. We assume that ΔS is ~ 1kB, similar to the entropy of fusion according to Richard's rule, and n = 5 as shown above. It follows that ν0 is ~ 1.48×10^{10} s^{-1} and ν is ~ 1×10^5 s^{-1} per atom, which agrees well with our direct MD simulations (2×10^5 s^{-1}). This agreement shows that the cavitation rate can be predicted from CNT with remarkable accuracy if the Tolman length is included.

5.4 Conclusion

Our systematic study shows that cavitation in a binary metallic liquid is a random Poisson process and that such complex processes can be well described by the transition state theory and classical nucleation theory. We demonstrate the methodology of obtaining the activation volume (or entropy) indirectly from MD simulations and the transition-state theory and deducing cavitation rate directly from MD simulations. The classical nucleation

theory converges with the simulations in describing the cavitation rate if the Tolman-length effect is considered. Our results also bear implications to broadly defined nucleation and growth processes.

5.5 References

[1] M. S. Plesset and A. Prosperetti, Bubble Dynamics and Cavitation, *Annu. Rev. Fluid Mech.*, 9, 145–185. 1977.

[2] H. G. Flynn, Physics of Acoustic Cavitation, *J. Acoust. Soc. Am.*, 31, 1582, 1959.

[3] M. Kornfeld and L. Suvorov, On the Destructive Action of Cavitation. *J. Appl. Phys.*, 15, 495–506, 1944.

[4] D. H. Trevena, *Cavitation and Tension in Liquids*, ***Hilger, Bristol***, England, 1987.

[5] K. S. Suslick, M. M. Mdleleni, and J. T. Ries, Chemistry Induced by Hydrodynamic Cavitation. *J. Am. Chem. Soc.*, 119, 9303–9304, 1997.

[6] J. Classen, C.–K. Su, and H. J. Maris, Observation of Exploding Electron Bubbles in Liquid Helium. *Phys. Rev. Lett.*, 77, 2006–2008, 1996.

[7] B. Niemczewski, Proposal of a Test Procedure for Ultrasonic Cleaners, *Trans. Inst. Met. Finish*, 81, 28–31, 2003.

[8] E. Maisonhaute, C. Prado, P. C. White, and R. G. Compton, Surface Acoustic Cavitation Understood via Nanosecond Electrochemistry. Part III: Shear Stress in Ultrasonic Cleaning, *Ultrason. Sonochem.*, 9, 297–303, 2002.

[9] S. J. Putterman, Sonoluminescence: Sound into Light, *Sci. Am.*, 272, 33–37, 1995.

[10] J. W. Gibbs, *The Scientific Papers of J. Willard Gibbs*, ***Dover, New York***, 1961.

[11] Y. Viisanen, R. Strey, and H. Reiss, Homogeneous Nucleation Rates for Water, *J. Chem. Phys.*, 99, 4680–4692, 1993.

[12] D. Kashchiev, On the Relation Between Nucleation Work, Nucleus Size, and Nucleation Rate, *J. Chem. Phys.* , 76, 5098–5102, 1982.

[13] T. Bazhirov, G. E. Norman, and V. Stegailov, Cavitation in Liquid Metals under Negative Pressures: Molecular Dynamics Modeling and Simulation, *J. Phys.: Condens. Matter*, 20, 114113, 2008.

[14] T. Kinjo and M. Matsumoto, Cavitation Processes and Negative Pressure, *Fluid Phase Equilib.*, 144, 343–350, 1998.

[15] J. M. J. Knap and M. Ortiz, Nanovoid Cavitation by Dislocation Emission in Aluminum, *Phys. Rev. Lett.*, 93, 165503, 2004.

[16] A. V. Neimark and A. Vishnyakov, The Birth of a Bubble: A Molecular Simulation Study, *J. Chem. Phys*., 122, 054707, 2005.

[17] H. Okumura and N. Ito, Nonequilibrium Molecular Dynamics Simulations of a Bubble, *Phys. Rev. E*, 67, 045301, 2003.

[18] S. Punnathanam and D. S. Corti, Work of Cavity Formation Inside a Fluid Using Free Energy Perturbation Theory, *Phys. Rev. E*, 69, 036105, 2004.

[19] V. K. Shen and P. G. Debenedetti, A Kinetic Theory of Homogeneous Bubble Nucleation, *J. Chem. Phys.*, 118, 768–783, 2003.

[20] I. Kusaka and D. W. Oxtoby, Identifying Physical Clusters in Vapor Phase Nucleation, *J. Chem. Phys.*, 110, 5249–5261, 1999.

[21] A. Kuksin, G. Norman, V. Pisarev, V. Stegailov, and A. Yanilkin, Theory and Molecular Dynamics Modeling of Spall Fracture in Liquids, *Phys. Rev. B*, 82, 174101, 2010.

[22] V. Rosato, M. Guillope, and B. Legrand, Thermodynamical and Structural Properties of F.C.C. Transition Metals Using a Simple TightBinding Model, *Philos. Mag. A*, 59, 321–336, 1989.

[23] G. Duan, D. H. Xu, Q. Zhang, G. Y. Zhang, T. Cagin, W. L. Johnson, and W. A. Goddard III, Molecular Dynamics Study of the Binary $Cu_{46}Zr_{54}$ Metallic Glass Motivated by Experiments: Glass Formation and Atomic-Level Structure, *Phys. Rev. B*, 71, 224208, 2005.

[24] J. Stadler, R. Mikulla, and H. R. Trebin, IMD: A Software Package for Molecular Dynamics Studies on Parallel Computers, *Int. J. Mod. Phys. C*, 8, 1131–1140, 1997.

[25] G. Duan, M. L. Lind, M. D. Demetriou, W. L. Johnson, W. A. Goddard III, T. Cagin, and K. Samwer, Strong Configurational Dependence of Elastic Properties for a Binary Model Metallic Glass, *Appl. Phys. Lett.*, 89, 151901, 2006.

[26] G. Duan, Simulations, Modeling, and Designs of Bulk Metallic Glasses, *Ph.D. Thesis*, ***California Institute of Technology***, 2008.

[27] A. Strachan, T. Cagin, and W. A. Goddard III, Critical Behavior in Spallation Failure of Metals, *Phys. Rev. B*, 63, 060103, 2001.

[28] M. C. Jones, J. S. Marron, and S. J. Sheather, A Brief Survey of Bandwidth Selection for Density Estimation, *J. Am. Stat. Assoc.*, 91, 401–407, 1996.

[29] J. Hachenberg, D. Bedorf, K. Samwer, R. Richert, A. Kahl, M. D. Demetriou, and W. J. Johnson, Merging of the α and β Relaxations and Aging via the Johari-Goldstein Modes in Rapidly Quenched Metallic Glasses, *Appl. Phys. Lett.*, 92, 131911, 2008.

[30] A. Masuhr, T.T. R. Waniuk, and W. J. Johnson, Time Scales for Viscous Flow, Atomic Transport, and Crystallization in the Liquid and Supercooled Liquid States of $Zr_{41.2}Ti_{13.8}Ni_{10.0}Be_{22.5}$, *Phys. Rev. Lett.*, 82, 2290–2293, 1999.

[31] W. L. Johnson and K. A. Samwer, Universal Criterion for Plastic Yielding of Metallic Glasses with a $(T/Tg)^{2/3}$ Temperature Dependence, *Phys. Rev. Lett.*, 95, 195501, 2005.

Chapter 6 Synthesis of single-component metallic glasses by thermal spray of nanodroplets on amorphous substrates

6.1 Overview

Bulk metallic glasses (BMGs) provide a number of unique properties (ductility, high strength, high corrosion resistance, and soft magnetism), but most metallic glasses have required very high quenching rates[1−8], leading only to thin films of amorphous material. A great deal of progress has been made toward synthesizing bulk amorphous metallic glasses since the original successes in 1960 using cooling rates of 10^6 K/s[1−5]. Indeed, with multicomponent metals having dramatically different character and radii, it is possible to obtain amorphous sheets of cm size for numerous applications[1−5]. Here we take up the **challenge of forming single-component metallic glasses** (SCMGs), which might have unique surface and bulk properties. Because of the low glass-forming ability of pure metals it has not been possible previously to make SCMG without extremely high quenching rates.

We propose here that SCMGs can be synthesized by thermal spray-coating of nanodroplets onto an amorphous substrate (ND-AS). We show that nanodrops of diameter ≤ 30 nm lead to sufficiently high cooling rates due to the rapid spreading of the nanodroplet during impact on the substrate, which leads to rapid cooling sustained by the large temperature gradients between the thinned nanodroplets and the bulk substrate. However even under these conditions, we show that for glass formation to outrun crystal nucleation, it is required that the substrate be amorphous (avoiding the heterogeneous nucleation sites that could lead to crystallization).

6.2 Simulation models

To demonstrate thermal-spray ND-AS formation of SCMG, we performed molecular-dynamics (MD) simulations for nanodrops of Cu up to 30 nm (1 million atoms) sprayed onto a Cu-Zr amorphous substrate ($Cu_{46}Zr_{54}$) system using force fields (potentials) validated to provide an accurate description of these metals. These MD simulations show that the Cu SCMGs are thermodynamically stable for the simulation time scales (up to 3 ns). In contrast, spraying the same Cu nanodroplets onto Cu crystal substrates leads to crystallization within 100 ps.

Our MD simulations used the embedded-atom-method potential for the Cu-Zr system[9] and the LAMMPS MD package (large-scale atomic/molecular massively parallel simulator)[10]. We constructed liquid Cu droplets with diameters of 10 nm (39081 atoms) which we equilibrated at 1300 K using constant-volume-temperature MD (without periodic boundary conditions). The nanodroplets were impacted on two different substrates at 300 K and 1 atm: (a) $Cu_{46}Zr_{54}$ glass, and (b) Cu (100) single crystal.

For the prototypical amorphous alloy substrate we started with randomly positioned Cu and Zr atoms for the $Cu_{46}Zr_{54}$ composition, melted at 2000 K for 0.5 ns and then cooled continuously to 300 K within 2 ns to form the bulk glass. Then to form the $Cu_{46}Zr_{54}$ glass substrate we constructed from the bulk system a slab containing 320,000 atoms (4.85 nm × 34.21 nm × 35.91 nm along the *x*-, *y*- and *z*-axes, respectively, with the *yz* plane as the surface), which we annealed at 1000 K for 4 ns and then cooled to 300 K using constant-pressure-temperature (NPT) MD to form the amorphous substrate.

As a prototypical crystalline substrate we used Cu (100) containing 432,000 atoms (10.96 nm × 21.93 nm × 21.93 nm). Here we started with the bulk FCC structure and

formed the 10.96-nm-thick (the *x*-direction) slab, which was equilibrated at 300 K and 1 atm using NPT MD.

The Cu nanodroplet was assigned an initial impact velocity along the *x*-axis (the substrate normal), and impacted the substrate. The impact velocity was varied from 0.01 km/s to 0.5 km/s. We used the microcanonical ensemble for impact simulations. The time step in MD simulation was 1 fs and the total simulation time was up to ~ 3 ns.

6.3 Results and Discussion

Fig. 6.1 shows the radial distribution functions (RDF) of Cu nanodroplets after impacting on crystalline and amorphous substrates. The resulting structures of the solidified nanoparticles on the crystal substrate cases show the long-range order characteristic of crystals. On the other hand, the loss of the long-range order in the glass substrate cases indicates that the "solidified" nanoparticles are still amorphous.

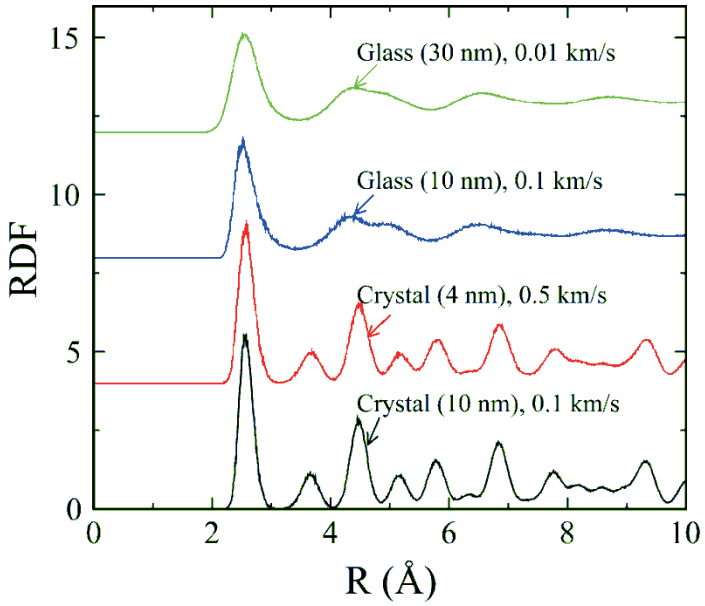

Figure 6.1 Radial distribution functions of various nanodroplets after impacting on various substrates at various impact velocities. The Cu nanodroplets form nanocrystals on the Cu crystal subsrate but become amorphous glasses on the $Cu_{46}Zr_{54}$ glass substrate.

The RDF only reveals the average structure information. To characterize the local structure of the amorphous Cu nanoparticle formed on the $Cu_{46}Zr_{54}$ glass substrate, we performed the Honeycutt-Anderson (HA) analysis[11−14] on various nanoparticles at equilibrium after impact. Fig. 6.2 shows the equilibrium configurations and the HA structure analysis of the Cu nanoparticles after impact. On the crystalline substrate, a Cu nanocrystal grows epitaxially with growth twins and stacking faults (Figs. 6.2a and 6.2b). The characteristic HA indices of this nanocrystal are mainly 1421, corresponding to the FCC structure (Fig. 6.2e).

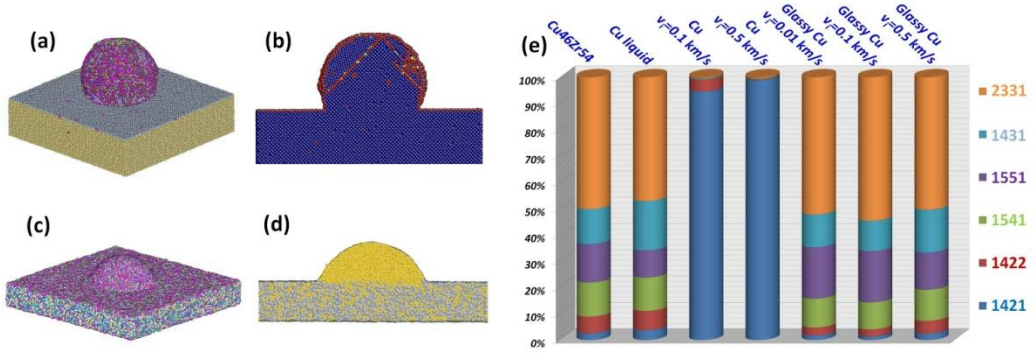

Figure 6.2 Snapshots of Cu nanodroplet (10 nm in diameter) impacting at 0.1 km/s on **(a,b)** a Cu single crystal substrate and **(c,d)** on a $Cu_{46}Zr_{54}$ glass substrate **(e)** analysis of the structure of crystalline, liquid, and glassy Cu and $Cu_{46}Zr_{54}$ glass using the Honeycutt-Andersen (HA) metric. Here 1421 is characteristic of fcc (face-centered cubic) structure, while equal amounts of 1421 and 1422 are characteristic of hcp (hexagonal close-packed) structure. On the other hand 2331 and 1551 indicate icosahedral packing characteristic of liquid or glassy metals; also for indices 1431 and 1541 show the structure of the liquid state [11−14]. **(b)** and **(d)** are cross-sectional views; here **(b)** shows some growth twins and FCC stacking faults. The HA indices for $Cu_{46}Zr_{54}$ glass, Cu glasses and Cu liquids all contain the icosahedral HA (2331 and 1551) of a liquid or glass, but are drastically different from those for crystalline Cu (e.g., 1421).

In sharp contrast, the impact with the $Cu_{46}Zr_{54}$ glass substrate leads to an amorphous Cu nanoparticle (Figs. 2c and 2d). HA indices 1551 and 2331 are the main characteristics of icosahedral packing, and are similar for $Cu_{46}Zr_{54}$ glass, Cu glass, and Cu liquid; this indicates that the amorphous Cu nanoparticle is similar in short-to-medium-range atomic packing to the $Cu_{46}Zr_{54}$ glass and to Cu liquid (Fig. 6.2e).

To verify that the amorphous nanoparticle is indeed "solidified" as a glass (rather than remaining a liquid), we calculated the mean squared displacement (MSD) of the Cu nanodroplet after the system reaches equilibrium, from which we extracted the diffusion coefficient (D) using the Einstein relation (MSD = $6D \times$ time). At 300 K, $D = 3.6 \times 10^{-5}$ cm^2/s for the liquid nanodroplet, which is 50 times higher than $D = 8.0 \times 10^{-7}$ cm^2/s for the amorphous nanoparticle. Thus, the amorphous nanoparticle is a solid-like SCMG.

To identify the point at which a phase transition occurs, it is valuable to determine the change in entropy with time and temperature. To extract the entropy evolution of the nanodroplets during the dynamic impact process, we used the Lin-Blanco-Goddard two-phase thermodynamic (2PT) model[15] to obtain the entropy of the nanodroplets impacting on the substrates. 2PT has been applied to various systems[15–18] to obtain accurate entropies.

We examined nanodroplets of 4 nm in diameter with impact velocity of 0.5 km/s and applied the 2PT model along the impact trajectory (up to 90 ps). The average temperature and entropy were extracted every 2 ps from the 2PT model, as shown in Fig. 6.3. The temperature and entropy increase initially for a few ps due to the dynamic impact, which converts kinetic energy to thermal energy, but then drops rapidly via substrate cooling. Due

to its higher thermal conductivity, the cooling rate in the Cu substrate case is about twice that of the $Cu_{46}Zr_{54}$ glass substrate. The Cu nanocrystal formed on the Cu substrate has entropy lower than the SCGM by ~ 1.5 J/mol/K at 500 K.

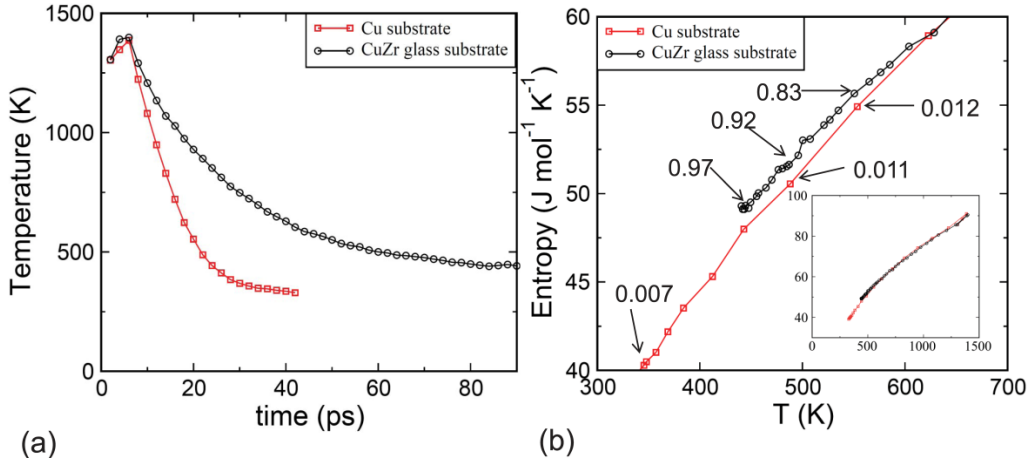

Figure 6.3 Temperature and entropy evolution of the 4 nm nanodroplets impacting at 0.5 km/s on crystalline or amorphous substrates. (a) For both substrates the temperature increases up to 6 ps after the initial impact and then decreases; with an exponential cooling rate (exponential fitting parameter) of 9.7×10^{10} s^{-1} for Cu substrate and 4.5×10^{10} s^{-1} for the glass substrate. (b) The entropy as a function of the temperature (below 700 K). The big difference between the crystal and amorphous substrates shows up below 700 K where the entropy of SCMG formed on amorphous substrate is about 0.2*R* higher than that of the nanocrystal formed on the Cu substrate at 500 K. Here *R* is the gas constant. Inset shows the whole temperature range. The numbers shown are the ratio of HA index 2331 to the sum over all the cases for the first nearest neighbors.

We also examined nanodroplets of various sizes (4 to 30 nm in diameter or 2,580 to 1,083,171 atoms) and larger substrates (up to 7,680,000 atoms), with a range of impact velocities (0.01 to 0.5 km/s), and various orientations for the Cu substrates [(100), (110), and (111)], and always obtained similar results. Our simulations show that nanodroplets ≤ 30 nm in diameter form SCMGs via ND-AS. We also performed the same simulations with another Cu-Zr potential[19], leading to nearly identical results.

For an impact velocity of 0.01 km/s a nanodroplet at 1300 K and diameter of 30 nm, achieves a cooling rate of ~ 2×10^{12} K/s, which we find is sufficient for SCMG formation on a glass surface. For an impact velocity of 0.5 km/s, a nanodroplet at 1300 K and diameter of 4 nm achieves a cooling rate of ~ 1×10^{13} K/s, which we find is also sufficient for SCMG formation. However for a crystalline substrate we find that these same conditions lead to crystallization. Our interpretation is that the glass substrates lack the heterogeneous crystallization nucleation sites. That is, the high energy-barrier for homogeneous crystal nucleation leads to kinetics too slow to compete with glass transition, and thus to SCMG formation. The high-temperature gradient near the substrate surface initiates the growth of the SCMG.

It has also been suggested that free-standing submicron droplets of high-purity metals may become amorphous solid-like phases in vacuum via thermal radiation cooling[20].

We claim that two conditions, rapid quenching due to the size of the nanodrop hitting the cold substrate and the amorphous nature of the substrate, are both essential to obtain a single component amorphous metal. Evidence in favor of this is presented in Fig. 6.3a, where the cooling for the Cu substrate is even more rapid than that for the amorphous substrate, but we find rapid crystallization of the droplet on the crystal substrate but not on the amorphous substrate. In addition we did a simulation of annealing the amorphous droplet (4 nm in diameter) without substrates from 600 K to 300 K over 100 ps and find that the droplet retains the amorphous structure. The simulation results are shown in Fig. 6.4.

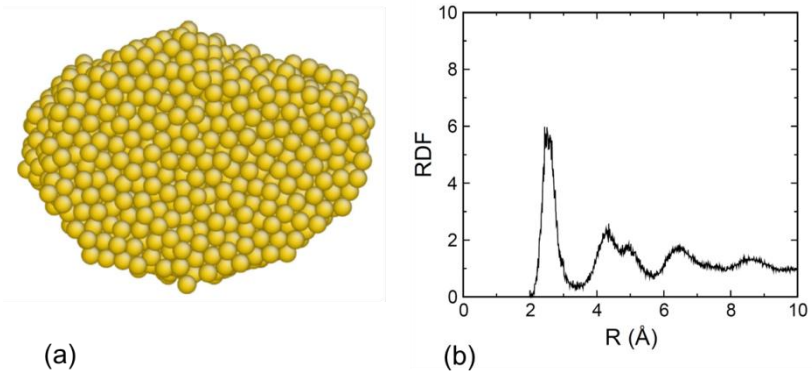

Figure 6.4 The internal structure and RDF of a 4 nm nanodroplet annealed from 600 K to room temperature over 100 ps. Shown in (a) is the cut through the middle of the nanodroplet, which shows the amorphous character as indicated by RDF shown in (b).

Certainly numerous droplets must be deposited to produce a macroscopic amorphous film. Thus one must wonder whether the growth of the pure Cu amorphous film might eventually lead to nucleation of the crystal phase. To demonstrate that this does not occur, we continued to impact Cu nanodroplets (4 nm in diameter) at 1300 K onto the growing film until 180 had been added as shown in Fig. 6.5. We modeled this by constructing a 20 $\times 3 \times 3$ array along the *x*-, *y*-, and *z*-directions, respectively (the *x*-direction is the impact direction), of nanodroplets (each 4 nm in diameter) spaced by 12 nm $\times 5$ nm $\times 5$ nm using an impact velocity of 0.2 km/s (so that the time between successive nanodrops hitting the amorphous surface is larger than 40 ps during which time the previous liquid droplets became an amorphous solid. We find that the bulk film (now 18.5 nm thick) remains amorphous until the system reaches equilibrium. The combination of rapid cooling rate and amorphous substrates still avoids crystal nucleation. The high viscosities (low diffusion coefficient) of the SCMGs make the phase transition from amorphous to crystal phase kinetically unfavorable.

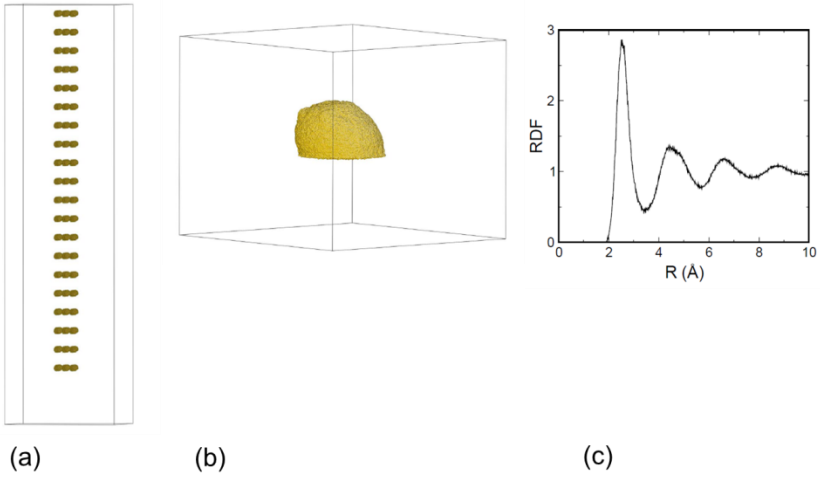

Figure 6.5 Result of impacting 180 nanodroplets (4 nm in diameter) sequentially on the CuZr glass substrate (only the droplet atoms are shown). (a) The initial conditions used an array of 20×3×3 = 180 droplets in the *x*-, *y*- and *z*-directions respectively (*x* is the impact direction), spaced by 12 nm along the *x* direction. The periodic slab has dimensions of 68.2 nm, 71.6 nm in the *y* and *z* directions. (b) The equilibrium structure after impact also shows amorphous character after the system reaches equilibrium, as indicated by the RDF shown in (c).

6.4 Conclusion

We have demonstrated that the synthesis of SCMGs via thermal spray of nanodroplets on amorphous substrates is viable for pure Cu, and we expect it to apply equally to other elemental metals. The thermal spray conditions required to form SCMGs are technically viable, and hence we expect that ND-AS may provide opportunities for broad applications that fully exploit the uniqueness of metallic glasses.

6.5 References

[1] A. L. Greer, Metallic Glasses, *Science*, 267, 1947−1953, 1995.

[2] W. L. Johnson, Bulk Glass-Forming Metallic Alloys: Science and Technology, *MRS Bull.*, 24, 42−56,1999.

[3] A. Inoue, Stabilization of Metallic Supercooled Liquid and Bulk Amorphous Alloys, *Acta Mater.*, 48, 279−306, 2000.

[4] W. Klement, R. H. Willens and P. Duwez, Non-crystalline Structure in Solidified Gold-Silicon Alloys, *Nature*, 187, 869−870, 1960.

[5] Z. P. Lu, C. T, Liu, J. R. Thompson, and W. D. Porter, Onset of Void Coalescence during Dynamic Fracture of Ductile Metals, *Phys. Rev. Lett.*, 93, 245503, 2004.

[6] D. H. Xu, G Duan, and W. L. Johnson, Unusual Glass-Forming Ability of Bulk Amorphous Alloys Based on Ordinary Metal Copper, *Phys. Rev. Lett.*, 93, 245504, 2004.

[7] V. Ponnambalam, S. J. Poon, and G. J. Shiflet, Fe-based bulk metallic glasses with diameter thickness larger than one centimeter, *J. Mater. Res.*, 19, 1320−1323, 2004.

[8] W. H. Wang, C. Dong, and C. H. Shek, Bulk metallic glasses, *Mater. Sci. Eng., R.*, 44, 45−89, 2004.

[9] M. I. Mendelev, M. J. Kramer, R. T. Ott, D. J. Sordelet, D. Yagodin, and P. Popel, Development of suitable interatomic potentials for simulation of liquid and amorphous Cu-Zr alloys, *Phil. Mag.*, 89, 967−987, 2009.

[10] S. Plimpton, Fast Parallel Algorithms for Short-Range Molecular Dynamics, *J. Comp. Phys.*, 117, 1−19, 1995.

[11] J. D. Honeycutt and H. C. Andersen, Molecular dynamics study of melting and freezing of small Lennard-Jones clusters, *J. Phys. Chem.*, 91, 4950−4963, 1987.

[12] Y. Qi, T. Cagin, W. L. Johnson, and W. A. Goddard III, Melting and crystallization in Ni nanoclusters: The mesoscale regime, *J. Chem. Phys.*, 115, 385, 2001.

[13] H. J. Lee, T. Cagin, W. L. Johnson, and W. A. Goddard III, Criteria for formation of metallic glasses: The role of atomic size ratio, *J. Chem. Phys.*, 119, 9858 (2003).

[14] G. Duan, D. Xu, Q. Zhang, G. Zhang, T. Cagin, W. L. Johnson, and W. A. Goddard III, Molecular Dynamics Study of the Binary $Cu_{46}Zr_{54}$ Metallic Glass Motivated by Experiments: Glass Formation and Atomic-Level Structure, *Phys. Rev. B*, 71, 224208 (2005).

[15] S.T. Lin, M. Blanco, and W. A. Goddard III, The two-phase model for calculating thermodynamic properties of liquids from molecular dynamics: Validation for the phase diagram of Lennard-Jones fluids, *J. Chem. Phys.*, 119, 11792 (2003).

[16] G.Y Zhang, Q. An, and W. A. Goddard III, Composition Dependence of Glass Forming Propensity in Al-Ni Alloys, *J. Phys. Chem. C*, 115, 2320−2331, 2011.

[17] T.A. Pascal, S.T. Lin, and W.A. Goddard III, Thermodynamics of liquids: standard molar entropies and heat capacities of common solvents from 2PT molecular dynamics, *Phys. Chem. Chem. Phys.*, 13, 169−181, 2011.

[18] Y.Y. Li, S.T. Lin, and W. A. Goddard III, Efficiency of various lattices from hard ball to soft ball: Theoretical study of thermodynamic properties of dendrimer liquid crystal from atomistic simulation, *J. Am. Chem. Soc.*, 126, 1872−1885, 2004.

[19] Y. Q. Cheng, E. Ma, and H. W. Sheng, Atomic Level Structure in Multicomponent Bulk Metallic Glass, *Phys. Rev. Lett.*, 102, 245501, 2009.

[20] Y. Kim, H. M. Lin, and T. F. Kelly, Amorphous solidification of pure metals in submicron spheres, *Acta Metall.*, 37, 247−255, 1989.

Chapter 7 **Simulating carbon and hydrogen phases under shock compression with electron force fields**

7.1 Overview

Electron force fields (eFF) have been widely used in the equation of state (EOS) of hydrogen, Li under extreme conditions[1,2], the Auger dissociation process[3], and the silicon crack process[4]. The eFF calculations faithfully captured the transition from H_2 molecular to atomic state and to plasma, and the transition of Li from the FCC to CI16 phase to the amorphous phase, as a function of increasing pressure and temperature[1,2]. These results demonstrated an excellent agreement between eFF predictions and leading experimental results.

In this chapter, we report on the use of eFF in the characterization of the Hugoniot relationship of carbon, which includes consecutive phase transitions also captured by experiments. From analyzing the atomic distribution functions at different points on the Hugoniot curve we establish that diamond distortions occur at ~ 167.7 GPa, followed by a transformation into BC8 phase at ~ 868.5 GPa, and subsequent transitions into amorphous phase at ~ 1292.0 GPa and into the liquid phase at ~ 2305.0 GPa.

We also report the Hugoniot states of hydrogen shocked from various initial densities as predictd from eFF, and compare our results with recent laser shock experiments and the path-integral Monte Carlo (PIMC) method. eFF prediction is in good agreement with recent low initial-density shock experiments. We observed the transitions from H_2 molecular to H atom to plasma for various initial densities.

7.2 Carbon phases under extreme conditions of high temperature and pressure

7.2.1 Introduction

The element carbon has received extensive attention for many centuries, not only because it is the backbone of biological molecules but because it is also one of the most abundant elements in the universe. Carbon is a primary constituent of white dwarfs and outer planets such as Uranus and Neptune[5]. Carbon has many practical and technological applications due to the remarkable and contrasting properties of its different allotropes, including the unique high-strength mechanical response of diamond (the only stable carbon phase under high-pressure experiments[6]) versus the softness of graphite, or the low electrical conductivity of diamond versus the very good conductivity of graphite. The behavior and properties of carbon under extreme conditions are of great importance to understanding outer planet interiors, white dwarfs, and extra-solar carbon planets[7, 8], as well as to tailoring new ablator materials capable of withstanding the operating conditions of, for example, inertial confinement fusion chambers[9], or the hypervelocity reentry conditions of spatial vehicles.

Despite its importance, the equation of state (EOS) of diamond under extreme conditions remains largely unknown after decades of research, mainly due to the difficulty in reproducing the required high pressures while controlling the measurement uncertainties during experiments[10]. The diamond anvil cell (DAC) experiment can only access pressures up to 300−400 GPa, typically at room temperature, still far from the extreme conditions that exist in numerous problems of interest[11]. Currently, the dynamical shock experiment is the only existing method that can probe the melting limits of diamond. Recently Knudson et al.[9] presented Hugoniot data for diamond over a pressure range of

550 to 1400 GPa using the magnetically driven flyer-plate technique. Combined with *ab initio* molecular-dynamics (AIMD) simulation, they were able to propose that the Hugoniot intercepts the diamond-BC8-liquid triple point along the melting limit. Other groups[6,12,13] have also reported diamond Hugoniot measurements up to pressures exceeding 1000 GPa.

Concurrently, theoretical calculations are used to reproduce and to extend experimental results. Models based on chemical models remain controversial in the diamond melt boundary[14,15] while quantum mechanical models have provided new insights. In 1996, Grumbach and Martin[16] published data for different carbon phases in a wide range of pressures (400−4000 GPa) and temperatures (2000−36000 K). Later, Wang et al.[17] calculated a more accurate diamond melt curve using Car-Parrinello molecular dynamics (CPMD) combined with thermodynamic integration techniques, and more recently Correa et al.[18] presented a carbon phase diagram calculated using a combined approach with AIMD and the two-phase method. The later predicted the existence of a diamond-BC8-liquid triple point at ~ 850 GPa. Romero and Mattson[19] used the AIMD method to get the carbon Hugoniot for pressures up to ~ 1400 GPa. In general, the results from quantum-mechanical calculations predicted a maximum in the diamond melt line.

7.2.2 Simulation methodology

This work is motivated by the considerable uncertainties in performing high-pressure, high-temperature experiments on carbon (in terms of generation, containment, and characterization) and by the inability of existing theoretical models to capture a high degree of electronic excitations, the structural and electronic heterogeneity, and the complex transient dynamics involved. To address such problems, we developed the electron force

field, eFF, as an inexpensive form of quantum-mechanics approximation which can describe the electron and nuclear dynamics of the extended systems containing highly excited electrons at a computational cost comparable to that of classical molecular dynamics. In this approach, nuclei are represented by point charges, and electrons by Gaussian wave packets with up or down spin. Electron position and radius are dynamical variables in the simulations. The total wave function is the Hartree product of the Gaussian spin orbitals and we introduce a Pauli potential derived from general valence bond (GVB) theory for antisymmetrization of the electrons. There are only three universal parameters for eFF in the Pauli potential, which are optimized for small molecules such as LiH, CH_4, C_2H_6, and B_2H_6[20]. In 2007, we reported the eFF results for the shock dynamics of hydrogen, including the transformation from molecular to atomic to plasma states[1], and in 2009 these results were validated by the corresponding shock experiments from LLNL[21]. Here we report the diamond principal Hugoniot in the pressure range of 100−3000 GPa, and the temperature range between 0−100000 K, using the eFF method.

The eFF method has been demonstrated before. eFF was applied to examine the non-adiabatic electron dynamics of a diamondoid $C_{197}H_{112}$ by the Auger-induced emissions of protons, hydride ions, and CH_x hydrocarbon fragments observed experimentally as a result of core ionization and subsequent Auger decay[3]: the core electron ionization led to cascaded bond-breaking events. eFF was also applied to studying the phase transition of lithium metal under shock compression[2]. It was found that two distinct consecutive phase changes exist which manifest themselves as a kink in the shock Hugoniot, previously observed in experiments but not explained. Based on the analysis of the atomic distribution

functions, it is established that the first phase transition corresponds to an fcc-to-cI16 phase transition that was observed previously in isothermal compression experiments, and the second phase transition corresponds to the formation of an amorphous phase of lithium with a novel topology, and much smaller coordination than in molten lithium, and a random connectivity distribution function. For all of the aforementioned applications the same universal parameters are used in eFF, and they will remain unchanged in this carbon study.

The simulations reported here consist of computing the shock behavior of carbon, using a periodic 2 x 2 x 2 diamond supercell containing 64 carbon atoms and 384 electrons. To compute the Hugoniot curve we use eFF to find a state described by pressure P, volume V, and internal energy U that satisfies the Rankine-Hugoniot condition,

$$U - U_0 + \frac{1}{2}(V - V_0)(P + P_0) = 0 \,, \qquad (7.1)$$

where the subscript zero denotes the initial state before compression. To determine the initial state, we perform constant-volume-energy NVE dynamic equilibration using the eFF-optimized diamond structure at a temperature of 300 K. The initial thermal equilibrium state found was: T_0 = 300.4 K, P_0 = 0 GPa, U_0 = -32.0817768 hartree/atom. Subsequently, we proceed to compress the equilibrated system using an isotropic strain rate of 0.1/ps to a variety of system densities. At each fixed density, we calculate the different states and determine the Hugoniot state parameters that satisfy Eq. 7.1. The eFF-optimized atomic volume for carbon diamond was 7.3289 Å^3 which is about 32% larger than the experiment value of 3.51 g/cm^3. The large atomic volume is due to the repulsive nature of the electrons

with the same spins inherent in Pauli potential, given that we have not adjusted any of the parameters used in our previous studies.

7.2.3 Results and Discussion

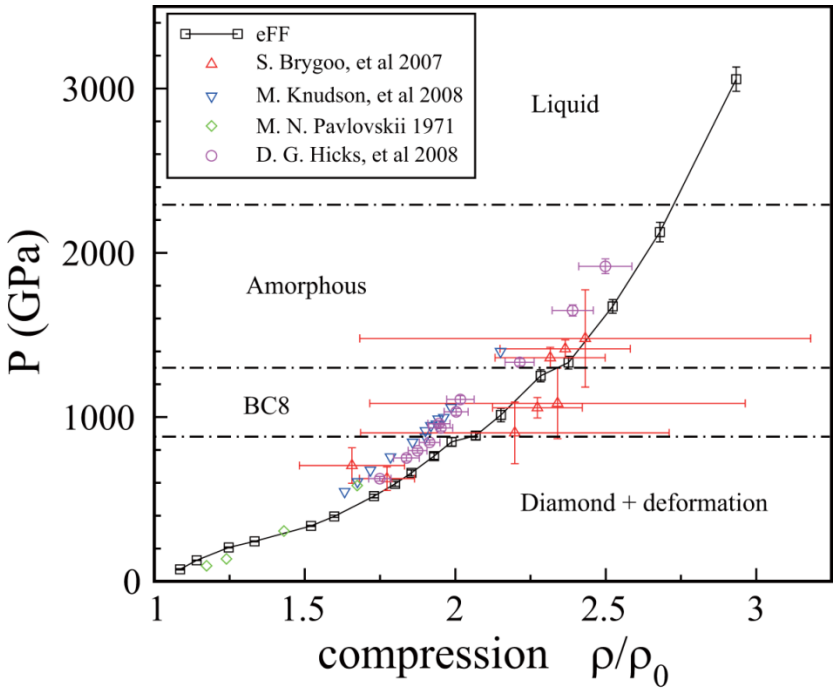

Figure 7.1 Shock Hugoniots for diamond carbon computed from eFF dynamics (square) and from the experiments[6,22,23]. eFF correctly predicts a series of phase transitions along the Hugoniot: diamond deformation at 167.7GPa, diamond to bc8 at 868.5 GPa, bc8 to amorphous at 1292.0 GPa and amorphous to liquid at 2305 GPa.)

Fig. 7.1 depicts the computed Hugoniot compared with different experimental results. We used density compression as the *x*-axis to compare properly with experiment. The eFF (solid square) Hugoniot is predicted to have two discontinuities, located at ~ 868.5 GPa and 1292.0 GPa. These results are consistent with recent experiments which report a discontinuity around 1100 GPa along Hugoniot[23]. Recently, Kundson et al.[9] proposed that the diamond Hugoniot intersects the melt boundary, and follows the diamond-liquid

boundary to the BC8-diamond liquid triple point, and then the BC8-liquid boundary before it finally enters the liquid regime. From our simulation, we found that the diamond solid transforms to a stable high-pressure phase at ~ 868.5 GPa and then transforms to the liquid phase at about ~ 1292.0 GPa. Our calculations indicate that the BC8 phase is as stable as diamond in the high-pressure regime, so we believe the high-pressure phase seen in the Hugoniot is the BC8 phase, which is confirmed by our structure analysis below.

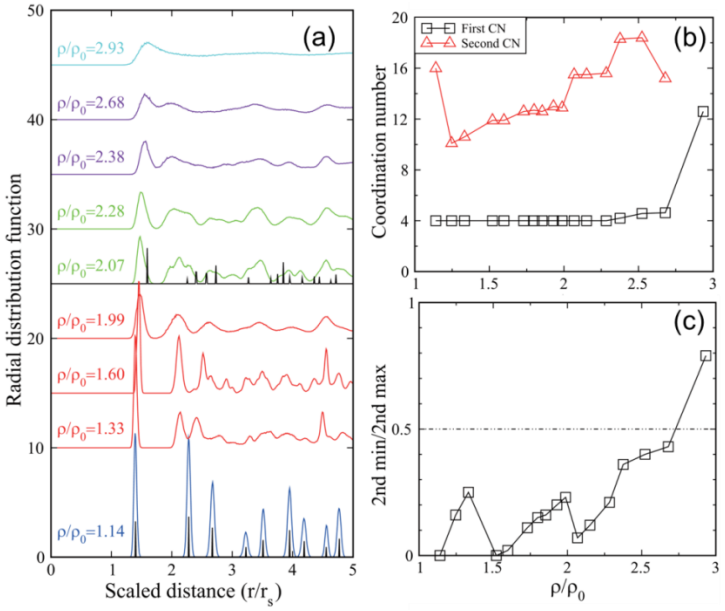

Figure 7.2 (a) Radial distribution functions show the structure change along the Hugoniot: The second peak splitting at 206.8 GPa (ρ/ρ_0=1.33) indicates a deformation starting at around 167.7 GPa (ρ/ρ_0=1.25). Then the broadened second peak at ~ 887.5 GPa (ρ/ρ_0=2.07) represents the transformation from diamond to BC8, followed by the disappearance of long-range order at ~ 1332.1 GPa (ρ/ρ_0=2.38), i.e., melting. (b) Coordination number (CN) calculations show that the first-shell CN is always 4.0 until amorphization/melting occurs. It increases from 4.0 to 4.2 when the amorphous form appears (from the mean square displace discussion below), where pressure increases from 1251.8 GPa to 1332.1 GPa. It then increases rapidly from 4.63 to 12.6 when the liquid forms, where the pressure increases from 2126.5 GPa to 3056.8 GPa. The second-shell CN drops from 16.0 to 10.1 when distortion happens and then increases continuously as pressure increases. A sudden increase occurs during the transformation from diamond to BC8 and BC8 to the amorphous structure. (c) The order parameter used to represent the transformation from the amorphous to liquid phase. We use 0.5 as the criteria for the phase transformation.

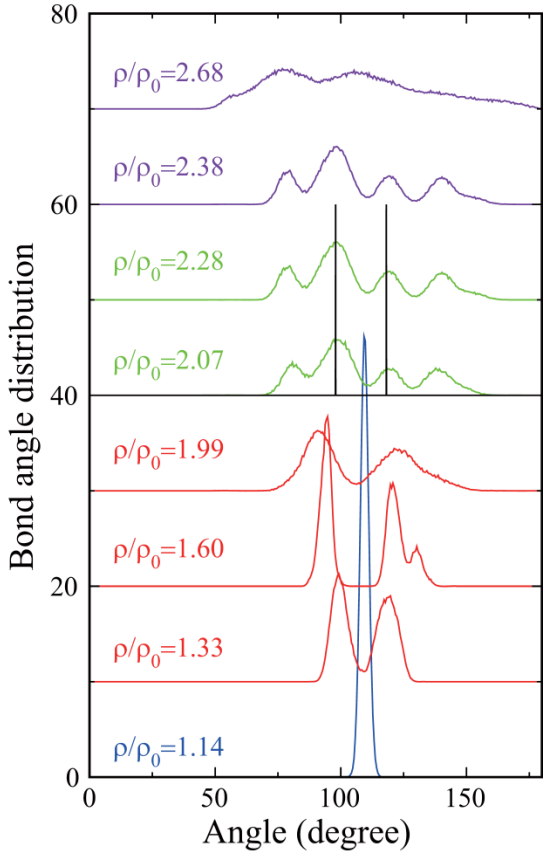

Figure 7.3 Bond angle distribution along Hugoniot. The bond cutoff is the first minimum position in RDF. For perfect diamond, it has only one angle 109.47˚, while for perfect BC8, it has two angles: 99˚ and 118˚.

To analyze the structure of the different phases along the Hugoniot, we computed the pair correlation function (RDF) and coordination number (CN) at different compressibility, as shown in Fig. 7.2. The second peak of RDF splits into two peaks above 167.7 GPa, indicating a distortion in the diamond structure. Although recent static DAC experiments[6] suggest that there is no plastic deformation for diamond up to 140 GPa, our simulations show that the deformation occurs at pressures lower than the diamond-BC8 transition. The CN for the first two shells decreases from 16.0 to 10.1 when the distortion occurs. This deformation is also characterized with the bond angle distribution (Fig. 7.3). The

transformation from the distorted diamond to BC8 is also manifested as the change in the RDF and the discontinuity in the second-shell CN. The RDF at 887.5 GPa is not exactly consistent with the perfect BC8 structure because it could not be transformed to perfect BC8 structure for our 64 nuclei system (the unit cell for BC8 has 16 nuclei). The second-shell CN increase is consistent with this phase transition. As the shock pressure increases, the bc8 phase melts at ~ 1292.0 GPa, as seen from the change in RDF and the second-shell CN discontinuity. It should be noted that the first-shell CN remains constant at 4.0 before melting, at which point it increases to 4.2. This is due to the strong covalent bonding in diamond. At high pressures, diamond may be an amorphous solid phase or liquid phase. To distinguish between these two phases, we computed the order parameter (i.e., the ratio of the amplitudes of RDF at the second minimum (g_{smin}) to the amplitude at the second maximum (g_{smax}), from which we can deduce that the amorphous phase transforms into the liquid phase at ~ 2305 GPa and 72500 K.

In order to understand in more detail the topological changes during phase transitions along the Hugoniot, we used the Honeycutt-Anderson (HA) analysis technique[24]. The HA technique uses an index composed of four integers *mnpq*, where *m*=1 indicates a atom pair *ij* are bonded together, *n* is the number of other atoms bonded to both atom *i* and *j* (the bond cutoff is taken as the first minimum of g(r)), *p* is the number of bonds between these neighboring atoms, and *q* is used to distinguish different bonding patterns with the same *n* and *p*. On the other hand, *m* = 2 indicates that atom i and j are not bonded. The numbers for m = 2 are normalized to the summation all *npq*, to lead them to 1.

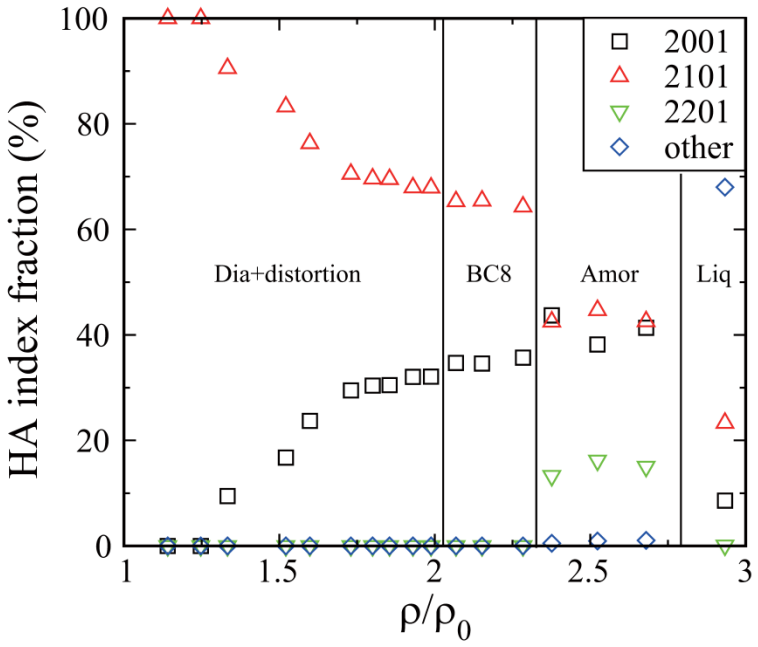

Figure 7.4 The fraction of the Honeycutt-Anderson indices vs. compression along the Hugoniot. Only the indices with m = 2 are shown here. The HA indices change abruptly when the phase transition happened (see the text).

We computed the fractions of the indices with m = 2 since the second peak of the RDF changes significantly during the phase transitions observed along the Hugoniot. The results are shown in Fig. 7.4. For the distortion portion, the percentage of 2101 decreases continuously to a steady value of around 69.5% and that for 2001 increases continuously to around 30.5%. When the distorted diamond transforms to BC8, the amount of 2101 decreases from 69.5% to 67.9% and that of 2001 increases from 30.5% to 32.1%. Perfect diamond only has pair index of 2101; while for the perfect BC8 structure, we obtain a percentage of 46.2% for 2101 and 53.85% for 2001. When amorphous forms appear at ~ 1332.1 GPa, the amount of 2101 decreases from 64.3% to 42.5% and that of 2001 increases from 35.7% to 43.7%. A new index (2201) also appears with a fraction of 13.3% when the amorphous phase starts to form. In the liquid phase at ~ 3056.8 GPa, we find that the

fraction of 2101 decreases to 23.3%, 2001 decreases to 8.6%, and 2201 disappears. For the indices with m = 1, the solid phase has 100% of 1001 until melting begins. Its fraction deceases by 2.6% when the amorphous phase begins to form at ~ 1332.1 GPa and continues to decrease as pressure increases, before disappearing when the liquid phase forms.

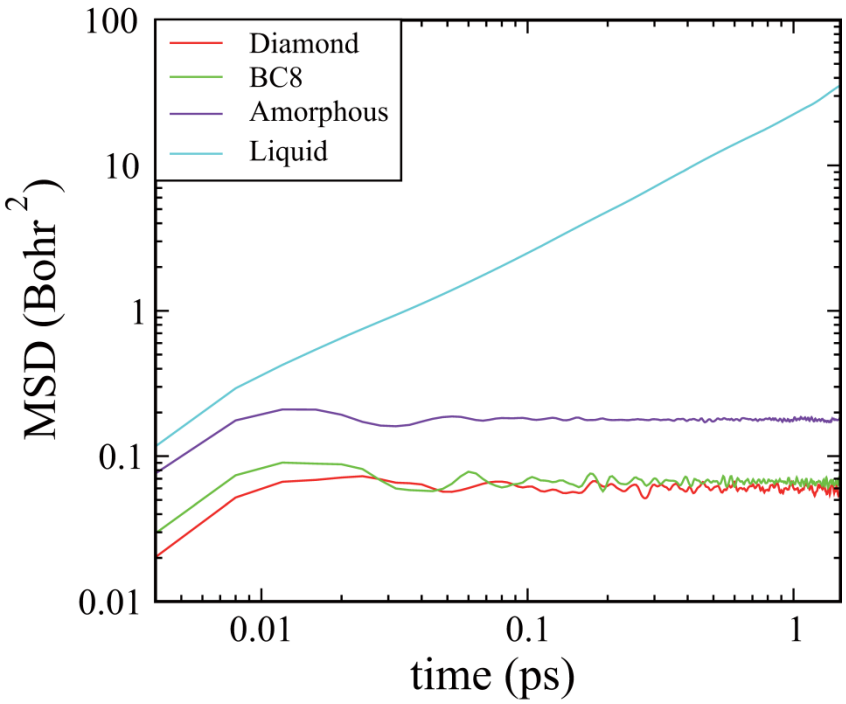

Figure 7.5 Mean squared displacements (MSD) of four different phases: cyan solid line represents the liquid phase (ρ/ρ_0 = 2.93, T = 98300 K), violet solid line is the amorphous phase (ρ/ρ_0 = 2.68, T = 66700 K), green solid line is the BC8 phase (ρ/ρ_0 = 2.068, T = 14406 K), and red solid line is the diamond phase (ρ/ρ_0 = 1:93, T = 10593 K). MSD increases rapidly when the phase changes from the amorphous phase to liquid phase.

To characterize the phase transition from the amorphous phase to liquid phase and the transport properties for the different phases, we compute the mean squared displacement for each case according to Eq. (7.2). Here t corresponds to time, N to the number of

particles, $r_i(t) - r_i(0)$ the distance traveled by particle i over a given time interval, and $\langle \cdots \rangle$ to the ensemble average.

$$MSD = \langle r^2(t) \rangle = \langle \frac{1}{N} \sum_{i=0}^{i=N} (r_i(t) - r_i(0))^2 \rangle \qquad (7.2)$$

The results in Fig. 7.5 show that the solid diamond phase and BC8 phase have similar particle displacement behavior. As expected, the amorphous phase has a larger MSD than the solid phase, while it will also reach a constant value after some time, which constitutes its localized character. The liquid-phase MSD increases faster, when compared to the other phases, and steadily as a function of time. This is consistent with the liquid-flow character. We estimate that the amorphous carbon phase along the Hugoniot has a very low fluidity compared to the high-temperature and high-pressure liquid phase.

7.2.4 Conclusion

We performed an eFF computational study of carbon Hugoniot, in which we addressed the phase boundaries between diamond deformation, diamond/BC8, BC8/amorphous, amorphous/liquid along the Hugoniot curve up to about 3000 GPa and 100,000 K. We find that our eFF description of the carbon Hugoniot agrees well with existing experiments and quantum-mechanical predictions. We presented a detailed structural analysis of each phase, including RDF, CN, and HA indices. From these we were able to determine the carbon phase change along the Hugoniot. Furthermore, we characterized the transport properties for each phase to determine the phase transition from the amorphous phase to the liquid phase. Our results indicate several structure transformations, including diamond deformation, diamond to BC8, BC8 to amorphous, and amorphous to liquid along the carbon Hugoniot, hence providing a new understanding of

carbon in the warm-dense regime and new insights with which to interpret future experimental results.

7.3 Warm-dense hydrogen under extreme conditions from various initial states

7.3.1 Introduction

Hydrogen at high pressures (100 to 300 gigapascals, GPa) and moderate temperatures (10,000 to 100,000 K) appears in diverse locales, from the interior of the cores of giant planets such as Jupiter[25], to the inner layers of fuel pellets for nuclear fusion applications[26]. Yet the nature of hydrogen under such conditions remains poorly understood, due to the challenges in experiments of generating and containing warm dense hydrogen (WDH) and in characterizing transiently present species, and to the challenges in theory of consistently, accurately, and efficiently modeling the complex mixture of phases that may be present (i.e., molecular, atomic, plasma, and metallic).

In the previously study Su and coworkers use the eFF[1–4] method to compute the WDH at various pressures, densities, and temperatures. Excellent agreement was found between the theoretical equation of state (EOS) from eFF to the available data from static and dynamic compression experiments in moderate pressures (< 100 GPa). Since then, new laser-shock experiments[21] have extended the available hydrogen EOS data to higher pressures (100−300 GPa), leading to excellent agreement with eFF in this region (Fig. 7.6a). However, under these extreme conditions, the assumed EOS of the shock impedance standard (SiO2) has been called into question[27]. Using a revised SiO_2 EOS leads to a qualitative change in the H_2 EOS (Fig. 7.6b). This controversy leaves unclear such critical issues as the presence or absence of phase transitions near ~ 100 GPa, the maximum

compression achievable under application of a single shock, and the existence of a metallic phase: all of which complicate the ultimate goal of understanding the nature of WDH.

Here we use eFF to address this controversy, by making comparisons to the new laser-shock EOS in both its uncorrected[21] and corrected[27] forms, over 100 to 300 GPa and 10,000 to 100,000 K. Furthermore, we examine the hydrogen Hugoniot EOS with various initial densities and compare our results with PIMC.

7.3.2 Results and Discussion

Fig. 7.6 shows the eFF-computed hydrogen Hugoniot and the comparison with other theories and recent experiments. Early experiments[28] indicate a larger maximum compression of $\rho/\rho_0 = 6 \pm 1.8$ at 110 GPa. More recent laser-shock experiments[21] (Jan, 2009) indicate a lower maximum compression of $\rho/\rho_0 = 5 \pm 0.5$ at 160 GPa. The discontinuity of this experiment at 110 GPa suggests a liquid-liquid phase transition. Later, the correction to the Jan. 2009 shock experiment was made[27] and the revised Hugoniot suggest an even lower compression of $\rho/\rho_0 = 4.65 \pm 0.5$. However, this correction makes the previous Hugoniot shift to the lower pressure as a whole.

The eFF Hugoniot agrees well with experiment at low pressures, but the comparison with the newest laser shock data is ambiguous. Also there is no discontinuity in the eFF Hugoniot, although we observe the molecular-phase-to-atomic-phase transition at 110 GPa. The maximum compression for the eFF Hugoniot is 4.95, which is close to the uncorrected laser shock experiment. The eFF results suggest that bonding at > 100 GPa is halfway

between an ideal gas of atoms ($\rho/\rho_0 = 4$) and an ideal gas of molecules ($\rho/\rho_0 = 6$). The comparison of eFF with other theories methods can be found in Ref. [1].

We analyze the species present in WDH using two criteria: (1) whether hydrogen atoms are bonded together, as indicated by a peak at r = 1.4 bohr (0.74 Å) in the nuclear-nuclear radial distribution function; and (2) whether electrons are bound to nuclei, as indicated by a negative total energy (kinetic plus potential) of the electrons. Applying these criteria, we find three phases: molecular, atomic and plasma (Fig. 7.6).

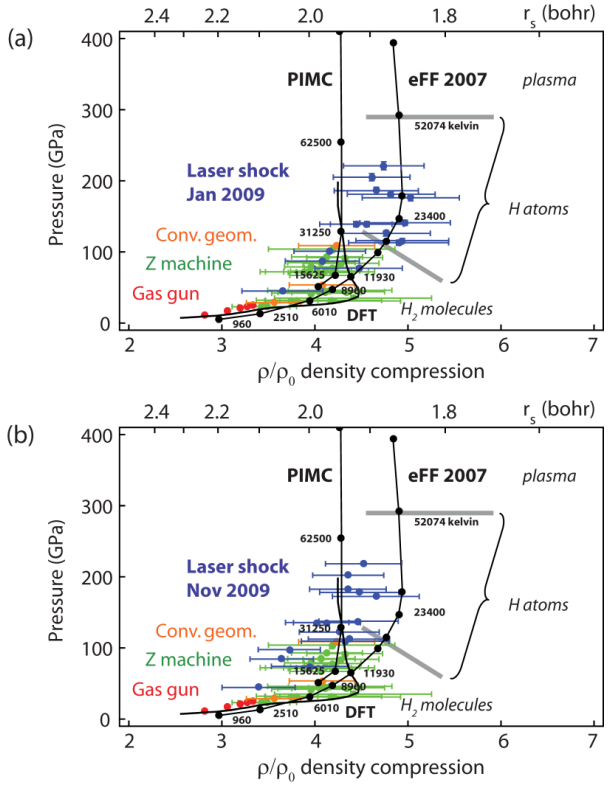

Figure 7.6 Single shock Hugoniot curve (pressure vs. density) for liquid H2 computed with eFF (solid line), compared to curves from two theories (solid line, path integral Monte Carlo [29]; dashed line, density functional theory [30]) and experiments using different shock sources (red dots, gas gun [31]; green dots, Z machine [32]; orange dots, convergence geometry [33]; blue dots, laser ablation [21,27]). The most recent experimental data (laser shock, blue dots) is shown in both (a) uncorrected (January 2009) and (b) corrected (November 2009) versions (following a revision of the quartz EOS).

We extended the hydrogen Hugoniot calculations by increasing the initial hydrogen densities from 0.171 g/cm^3 to 0.25 g/cm^3, 0.30 g/cm^3, and 0.40g/cm^3. Figs. 7.7 and 7.8 are the eFF-computed Hugoniots with the four various initial densities. We also observe the phase transition from molecular phase to atomic phase and plasma phase for the three high initial densities using a similar structure analysis method. The transition pressure is increased as the initial density increases. The transition temperature from the molecular to atomic phases are nearly same (~ 20000 K), but from the atomic phase to the plasma phase the temperature varies for different initial conditions. Our results indicate that the pre-compression will decrease the compression from 4.95 to 4.2.

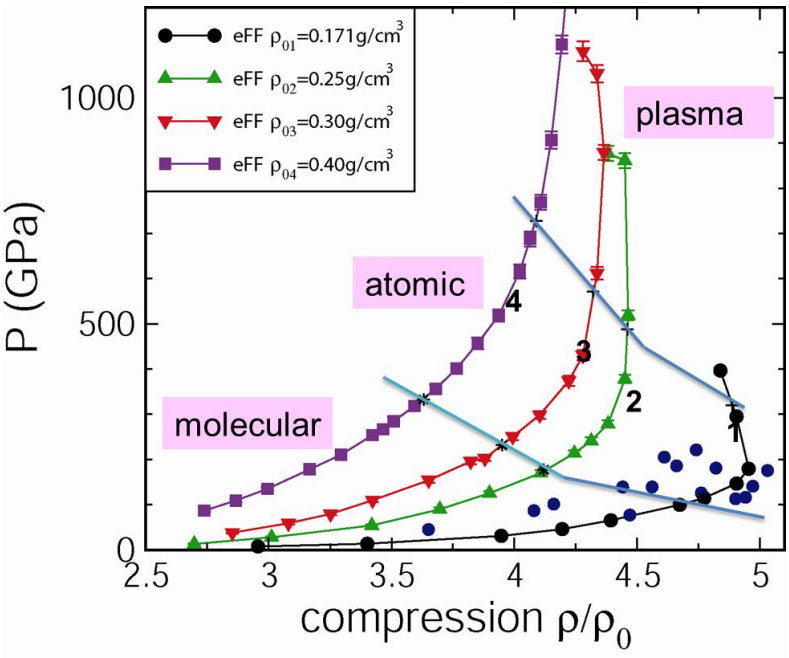

Figure 7.7 The eFF hydrogen Hugoniot (P-compression) with various initial densities. The various phase regions are separated by the thick lines.

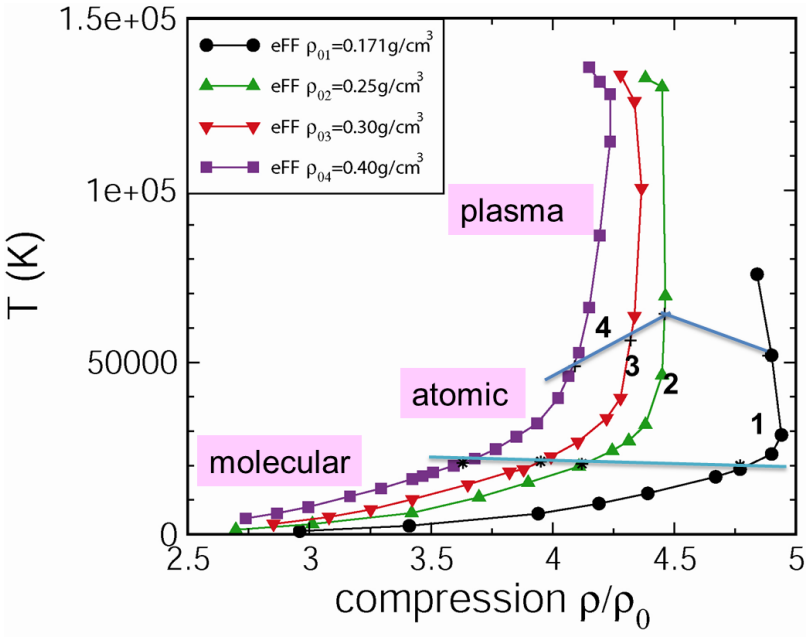

Figure 7.8 The eFF hydrogen Hugoniots (T-compression) with various initial densities. The various phase regions are separated by the thick lines.

We compare our hydrogen Hugoniots with PIMC results[34] in Fig. 7.9. The eFF yields the same compressibility as the recent experiment, but PIMC is 20% lower in compressibility for the Hugoniot centered at the lowest initial density. For the three high initial densities, PIMC gives nearly the same compressibility, but our eFF results give different values, which might be consistent with the experiments.

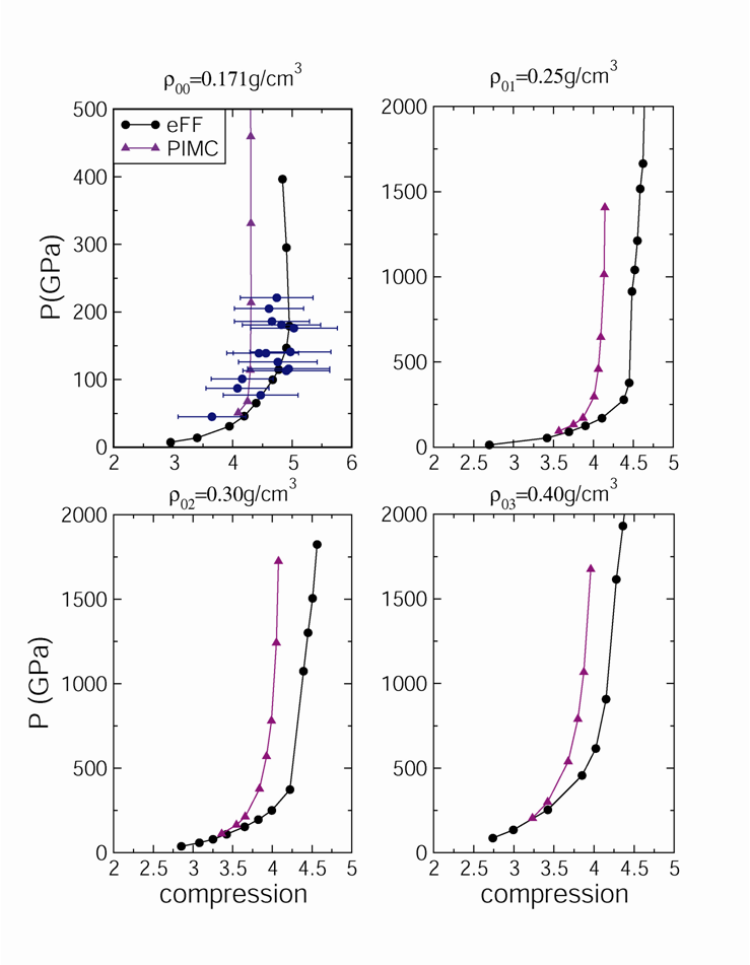

Figure 7.9 The comparison of eFF-predicted hydrogen Hugoniots with PIMC for various initial densities. The filled black circles are eFF results and the filled triangles are PIMC results.

7.3.3 Conclusion on hydrogen simulations

In summary, we compare the eFF-predicted hydrogen Hugoniot with recent laser-shock experiments. Our results agree very well with the uncorrected laser-shock experiments and show no discontinuities on the Hugoniot. But we did observe the phase transition from molecular phase to atomic phase to plasma phase along the Hugoniot. The extended Hugoniots were also examined with various initial densities and compared with the PIMC results. Our results need to be verified by future experiments.

7.4 References

[1] J. T. Su and W. A. Goddard III, Excited electron dynamics modeling of warm dense matter, *Phys. Rev. Lett.*, 99, 185003, 2007.

[2] H. Kim, J. T. Su, and W. A. Goddard III, High-temperature high-pressure phases of lithium from electron force field (eFF) quantum electron dynamics simulations, *Proc. Natl. Acad. Sci.*, 108, 15101-15105, 2011.

[3] J. T. Su and W. A. Goddard III, Mechanisms of Auger-induced chemistry derived from wave packet dynamics, *Proc. Natl. Acad. Sci.*, 106, 1001−1005, 2009.

[4] P. L. Theofanis, A. Jaramillo-Botero, W. A. Goddard, III, and H. Xiao, Nonadiabatic Study of Dynamic Electronic Effects during Brittle Fracture of Silicon, *Phys. Rev. Lett.*, 108, 045501, 2012.

[5] W. Hubbard, Interiors of giant planets, *Science*, 214, 145−149, 1981.

[6] S. Brygoo, E. Henry, P. Loubeyre, J. Eggert, M. Koenig, and B. L. Alessandra, Laser-shock compression of diamond and evidence of a negative-slope melting curve, *Nat. Mater.*, 6, 274−277, 2007.

[7] M. Ross, The ice layer in Uranus and Neptune—diamonds in the sky?, *Nature*, 292, 435−436, 1981.

[8] L. R. Benedetti, J. H. Nguyen, W. A. Caldwell, H. J. Liu, M. Kruger, and R. Jeanloz, Dissociation of CH_4 at High Pressures and Temperatures: Diamond Formation in Giant Planet Interiors?, *Science*, 286, 100−102, 1999.

[9] M. Knudson, M. P. Desjarlais, and D. H. Dolan, Shock-Wave Exploration of the High-Pressure Phases of Carbon, *Science*, 322, 1822−1825, 2008.

[10] F. Bundy, W. Bassett, M. Weathers, R. Hemley, H. Mao, and A. Goncharov, The pressure-temperature phase and transformation diagram for carbon, *Carbon*, 34, 141-153, 1996.

[11] F. Occelli, P. Loubeyre, and R. Letoullec, Properties of diamond under hydrostatic pressures up to 140 GPa, *Nat. Mater.*, 2, 151−154, 2003.

[12] D. Bradley, J. Eggert, D. Hicks, P. Celliers, S. Moon, R. Cauble, and G. Collins, Shock Compressing Diamond to a Conducting Fluid, *Phys. Rev. Let.*, 93, 195506, 2004.

[13] H. Nagao, K. Nakamura, K. Kondo, and et al., Hugoniot measurement of diamond under laser shock compression up to 2 TPa, *Phys. Plasmas*, 13, 052705, 2006.

[14] M. van Thiel, and F. H. Ree, High-pressure liquid-liquid phase change in carbon. *Phys. Rev. B*, 48, 3591−3599, 1993.

[15] L. Fried and W. Howard, Explicit Gibbs free energy equation of state applied to the carbon phase diagram, *Phys. Rev. B*, 61, 8734−8743, 2000.

[16] M. Grumback and R. Martin, Phase diagram of carbon at high pressures and temperatures, *Phys. Rev. B*, 54, 15730−15741, 1996.

[17] X. Wang, S. Scandolo, and R. Car, Carbon Phase Diagram from Ab Initio Molecular Dynamics, *Phys. Rev. Lett.*, 95, 185701, 2005.

[18] A. Correa, S. Bonev, and G. Galli, Carbon under Extreme Conditions: Phase Boundaries and Electronic Properties from First-Principles Theory, *Proc. Nati. Acad. Sci.*, 103, 1204−1208, 2006.

[19] N. Romero and W. Mattson, Density-functional calculation of the shock Hugoniot for diamond, *Phys. Rev. B*, 76, 214113, 2007.

[20] J. Su and W. Goddard, The dynamics of highly excited electronic systems: applications of the electron force field, *J. Chem. Phys.*, 131, 244501, 2009.

[21] D. Hicks, T. Boehly, P. Celliers, J. Eggert, S. Moon, D. Meyerhofer, and G. Collins, Laser-driven single shock compression of fluid deuterium from 45 to 220 GPa, *Phys. Rev. B*, 79, 014112, 2009.

[22] M. Pavlovskii, Shock compression of diamond, *Sov. Phys. Solid State*, 13, 741−742, 1971.

[23] D. H. et al., High-precision measurements of the diamond Hugoniot in and above the melt region, *Phys. Rev. B*, 78, 174102, 2008.

[24] J. D. Honeycutt and H. C. Andersen, Molecular dynamics study of melting and freezing of small Lennard-Jones clusters, *J. Phys. Chem.*, 91, 4950−4963, 1987.

[25] H. M. Van Horn, Dense Astrophysical Plasmas, *Science*, 252, 384−389, 1991.

[26] M. K. Matzen et al., Pulsed-power-driven high energy density physics and inertial confinement fusion research, *Phys. of Plasmas*, 12, 055503, 2005.

[27] M. D. Knudson and M. P. Desjarlais, Shock Compression of Quartz to 1.6 TPa: Redefining a Pressure Standard, *Phys. Rev. Lett.*, 103, 225501, 2009.

[28] G. W. Collins et al., Measurements of the Equation of State of Deuterium at the Fluid Insulator-Metal Transition, *Science*, 281, 1178−1181, 1998.

[29] B. Militzer and D. M. Ceperley, Path Integral Monte Carlo Calculation of the Deuterium Hugoniot, *Phys. Rev. Lett.*, 85, 1890−1893, 2000.

[30] B. Holst, R. Redmer, and M. P. Desjarlais, Thermophysical properties of warm dense hydrogen using quantum molecular dynamics simulations, *Phys. Rev. B*, 77, 184201, 2008.

[31] W. J. Nellis et al., Equation-of-state data for molecular hydrogen and deuterium at shock pressures in the range 2–76 GPa, *J. Chem. Phys.*, 79, 1480−1486, 1983.

[32] M. D. Knudson, D. L. Hanson, J. E. Bailey, C. A. Hall, and J. R. Asay, Use of a Wave Reverberation Technique to Infer the Density Compression of Shocked Liquid Deuterium to 75 GPa, *Phys. Rev. Lett.*, 90, 035505, 2003.

[33] G. V. Boriskov et al., Shock compression of liquid deuterium up to 109 GPa, *Phys. Rev. B*, 71, 092104, 2005.

[34] B. Militzer, Path integral calculation of shock Hugoniot curves of precompressed liquid deuterium, *J. Phys. A: Math. Gen.*, 36, 6159–6164, 2003.